

Multiscale Pore Network Modeling of Hierarchical Media with Applications to Improved Oil and Gas Recovery

by

Mirza Shoaib Beg

A thesis

Presented to the University of Waterloo

in fulfillment of the

thesis requirement for the degree of

Master of Applied Science

in

Chemical Engineering

Waterloo, Ontario, Canada, 2021

© Mirza Shoaib Beg 2021

Author's Declaration

I hereby declare that I am the sole author of this thesis. This is a true copy of the thesis, including any required final revisions, as accepted by my examiners.

I understand that my thesis may be made electronically available to the public.

Abstract

For complex geological materials such as carbonates and tight sandstones having pores at several scales, the conventional relationships are not adequate to quantify transport properties. Therefore, it becomes important to study these complex rocks at the pore scale and apply relevant physics for transport properties. However, with the current state of imaging technology it is not possible to obtain realistic images of the rock having pores at several orders of magnitude in a single image. Therefore, it becomes necessary to develop modeling tools that can study images with unresolved porosity. A pore network can be extracted such that the transport properties of the visible voids are calculated, while the interplay between micro- and macro-porosity can be studied by modeling the unresolved pores as effective continua. In this work, first we have attempted to generate three phase multiscale artificial images using PoreSpy and then devised a method of network extraction on these three phase images in a single step and thus created a multiscale pore network model using OpenPNM. Also, 3D and three-phase segmentation of real carbonate images were prepared where the developed algorithm was successfully tested. A cubic grid is applied to the micropores region which becomes the mesh for the continua simulation with each element endowed with effective properties. The macropores are then stitched together with the continua scale, thus creating a hybrid hierarchical pore network that possess information at several scales. The multiscale pore network algorithm prepared in this work is fast and robust and has been tested on several 2D and 3D artificial and real rock images. Porosity, permeability, and formation factor have been calculated on the resulting pore networks and validated with the real sandstone and carbonate images.

Acknowledgements

First, I would thank Allah Almighty for all the kindness bestowed upon me. I would like to thank my supervisors Professor Jeffrey Gostick and Professor Nasser Mohieddin Abukhdeir, the people who made this thesis possible and to Judy Caron for her proactive support.

Dedication

This thesis is dedicated to my parents, my father-in-law, my mother-in-law, and my wife whose care and support I will always be grateful for.

Table of Contents

List of Figures	viii
List of Table	xiii
List of Symbols	xiv
1 Introduction.....	1
1.1 Research motivation.....	1
1.2 Objectives.....	5
2 Background	6
2.1 Porous Media	6
2.1.1 Porosity	7
2.1.2 Microporosity	8
2.1.3 Permeability	9
2.1.4 Pore size distribution.....	10
2.1.5 Tortuosity	12
2.1.6 Formation Factor and Resistivity	14
2.2 Pore network modeling – General review.....	18
2.3 Image Processing and Analysis.....	22
2.3.1 X-ray Imaging	23
2.3.2 Image Representation.....	25
2.3.3 Correcting Imaging defects.....	26
2.3.4 Image Enhancement.....	26
2.3.5 Segmentation and Thresholding.....	26

2.3.6	Binary Images	28
2.3.7	Distance Transforms and Watershed Segmentation	31
3	Literature Review	34
3.1	Pore network extraction	34
3.2	Multiscale pore network modeling	38
4	Multiscale Pore Network Modeling	45
4.1	Hybrid-hierarchical Pore Network Modeling	45
4.1.1	Multiscale network extraction process.....	48
4.1.2	Permeability estimation in hybrid hierarchical networks	53
4.1.3	Formation factor estimation in hybrid hierarchical networks	58
4.2	Materials and Images Used	60
4.3	Results and Discussion.....	61
5	Conclusions and future work.....	74
5.1	Conclusions.....	74
5.2	Further studies.....	74
	References.....	77
	Appendix A.....	83
	Appendix B.....	86
	Appendix C.....	91
	Appendix D.....	110

List of Figures

Figure 1: Global oil demand by scenario between 2010 and 2040, and declines in supply from 2019 IEA (2020), World Energy Outlook 2020, IEA, Paris <https://www.iea.org/reports/world-energy-outlook-2020> Stated Policies Scenario (STEPS), Sustainable Development Scenario (SDS) [3]. .. 1

Figure 2: A typical pore size distribution curve for Berea sandstone (blue) and Estailades carbonate (orange)[26] 11

Figure 3: A typical capillary pressure vs saturation curve for Berea sandstone (blue) and Estailades carbonate (orange) [26]..... 12

Figure 4: FF vs ϕ log-log plot of a formation to determine the formation specific parameters [30]. . 15

Figure 5: A plot of Formation Factor vs Permeability for U.S. Gulf coast formation [30]. 17

Figure 6: A pore-throat-pore schematic diagram for hydraulic calculations 20

Figure 7: A simplified Illustration of a cone-beam imaging system..... 24

Figure 8: Schematic illustration of X-ray CT acquisition and reconstruction process. 25

Figure 9: A grayscale image on left showing void in light gray, grains in dark gray and matrix in the background with microporosity which cannot be clearly distinguished. On the right is the segmented image with void in white, grains in black and matrix in darker gray. 28

Figure 10: Closing operation - Dilation of the original image followed by Erosion of the dilated image using the same structuring element..... 30

Figure 11: Opening operation - Erosion of the original image followed by dilation of the eroded image using the same structuring element..... 31

Figure 12: Euclidean distance transform applied to the binary image (a) on the left resulting in the (b) graylevel image shown on the right. 32

Figure 13: Two touching objects, their distance transform and watershed segmentation showing the ridge line 33

Figure 14: Basic steps of SNOW algorithm, a) a binary image, b) applying Euclidean Distance transform on the binary image, c) finding peaks using gaussian filter and trimming spurious peaks, d) finally applying marker-based watershed segmentation. 37

Figure 15:Representation of the dual PNM models, the Coincident micropore model (a) proposed by Berki [38], a cubic-lattice based network of macropores is embedded in a homogeneous microporous matrix of uniform properties, (b) The Parallel micropores model proposed by Baur [39] is image based and microporosity is added in parallel to the user defined percentage of macrothroats, (c) The Explicit micropores model used by Jiang [40] and Masa [41], the unresolved microporosity is modeled on high resolution micro-tomograph images where each individual micropore is taken into account. While in the Averaged micropores model used (d) by Bultreys [42] microporosity is modeled as truncated cone micro-link between macropores taken both in series and parallel communication to the macropores. In the proposed Hybrid micropores model (e) microporosity is taken as the original shape and location by image analysis with its network of macropores and macrothroats, the microporosity is taken as a continuum placing a cubic grid while the communication between macropores and micropores is through a macropore surrounding rim of pores, while the solid phase (black) shown at its true location. In models (a), (b) and (d) shaded region represents the matrix..... 39

Figure 16: Examples of three artificial images of different sizes. 46

Figure 17: The network extraction of images shown in figure 16. 47

Figure 18: The concept of rim is shown above. In fig (a) the two pores with their surrounding rims as identified in step 2 of the procedure are shown. In fig (b) cubic lattice is inserted in surrounding matrix having all 1s as explained in step 7 and do the network extraction in the macropores regions having all 0s using OpenPNM network extraction algorithm. 49

Figure 19: A three phase simple image with matrix in green, two connected macropores and one non-touching vug in yellow and a grain embedded in matrix is shown in black (top left)..... 49

Figure 20: From left to right, a) first column show step 1 as pore network for voids is found, b) step 2 in second column shows cubic lattice is created in micropores, c) third column shows step 3 where, using basic image processing techniques micropore voxels rim of each void are identified with their associated void, as indicated by darker shades. (zoomed in view with connections are shown in second row) d) The fourth column shows the last step when these voxels are connected with void and micropores..... 50

Figure 21: Example 2D and 3-phase image on a) left with green as matrix region, yellow as macropores and black are solid grains, and b) its network extraction is shown on the right. The value of absolute permeability determined was 0.775. 51

Figure 22: (a) Network extraction of a 3D and 3-phase artificial image. Macropores, interconnects (red color) and matrix (white), (b) below the same network with overlaid image showing solid grains. 52

Figure 23: A schematic illustration of the geometrical elements in the proposed hybrid model..... 55

Figure 24: The figure (a) above shows that the isolated matrix region surrounded by solid (bottom left corner) in a rectangle shape is not connected to the combined network, whereas in (b) vug (bottom right corner) is connected to the surrounding matrix via interconnects shown in blue color..... 57

Figure 25: (a) Massangis Juane Limestone raw image and (b) a subsection of the greyscale raw image taken for 3 phase segmentation (c) Three phase segmentation. 62

Figure 26: a) Macropore network in 3D and, (b) histogram of network properties for Massangis Jaune Limestone..... 63

Figure 27: 2D slices through the three-phase segmentation of various z-direction slices of Massangis Jaune Limestone sample. The macroporosity fraction is approx. equal to microporosity. The microporosity type is both pore lining and pore filling resulting in microporosity having dominating control on transport properties. 64

Figure 28: 3D network of Massangis Jaune Limestone shown in Paraview. Matrix is in white, macrothroats in red and interconnects are shown in blue color..... 65

Figure 29: (a) Estailades raw image and (b) a greyscale subsection of the raw image taken for 3 phase segmentation (c) Three phase segmentation.....	66
Figure 30: Estailades carbonate a) Macropore network and b) histogram of network properties.	67
Figure 31: 2D representation of three-phase segmentation of various z-direction slices of Estailades carbonate sample. The microporosity fraction is greater than macroporosity. The microporosity and macroporosity arrangement results in parallel dominated flow with resulting higher permeability.	68
Figure 32: Two different view angles for 3D network of Estailades carbonate shown in Paraview. Matrix is in white, macrothroats in red and interconnects are shown in blue color.	69
Figure 33 : Artificial image of the rock on the left compared with an actual SEM image on the right. On the right rock types I an II [18] are shown.....	87
Figure 34: Two artificially generated 2-D and 3-phase images and real rock type III are shown in the right column.....	88
Figure 35: A few more examples of artificially generated images.	90
Figure 36: Selected sandstone SEM images for 2D analysis, (a) top left to right Berea sandstone, (b) North Sea sandstone plug 44, (c) North Sea sandstone plug 77, (d) bottom left to right North Sea sandstone plug 130, (e) North Sea sandstone plug 367.	91
Figure 37: Berea_D_20 sandstone (a) raw image, (b) three-phase segmentation of a selected section, (c) network extraction and (d) histogram of network properties.	92
Figure 38: North Sea sandstone plug 44 a) Three phase segmentation, b) Macropore network and c) histogram of network properties	93
Figure 39: (a) North Sea sandstone plug 77 three-phase segmentation of a selected section.....	94
Figure 40: (a) North Sea sandstone plug 130 three-phase segmentation of a selected section, (b) network extraction and (c) histogram of network properties.....	95
Figure 41: North Sea sandstone plug 367, a) Three-phase segmentation b) Macropore network and c) histogram of network properties.....	96

Figure 42: Selected Carbonate SEM images for 2D analysis, (a) top left to right Estailades ES32_0523 (images downloaded from www.digitalrockportal.org, (b) Estailades ES32_1832, bottom left to right (c) Savonnieres carbonate, (d) Austin chalk. 101

Figure 43: a) Estailades ES32_0532 three-phase segmentation of a selected section, b) network extraction and c) histogram of network properties. 102

Figure 44: Estailades ES32_1832 (a) three phase segmentation of a selected section, (b) network extraction and (c) histogram of network properties. 103

Figure 45: Savonnieres carbonate (a) three phase segmentation of a selected section (b) network extraction and (c) histogram of network properties. 104

Figure 46: (a) Austin chalk three phase segmentation of a selected section, (b) network extraction and (c) histogram of network properties. 105

Figure 47: Example of a Tomography image of a sandstone material with microporosity. Top left shows a greyscale image where the microporosity is visible between the voids (dark) and grains (light). Bottom left shows the result after applying a non-local means filter. 111

List of Tables

Table 1: Grain sizes for sands, table borrowed from [48].....	54
Table 2: Network statistics for 3D and 3-phase carbonate rock samples.	70
Table 3: Comparison of hybrid algorithm with the experimental values, * experimental range for this value is taken from [51].	71
Table 4: Summary of network statistics for 3D artificial and 2D sandstone samples.	97
Table 5: Summary of network statistics for 2D carbonate samples.....	106

List of Symbols

The following is a list of symbols used in this thesis. SI units are indicated in parenthesis where applicable.

P	Pressure Pascals, ($\frac{N}{m^2}$)
R	Pore Radius (m)
L	Pore Length (m)
μ	Fluid viscosity ($\frac{m^2}{sec}$)
g_h	hydraulic conductance $m^2/(Pa \times sec)$
q_{ij}	Flow rate from pore i to pore j
\emptyset	Porosity
K_{ck}	Carman-Kozeny estimate of permeability
k_{ck}	Carman-Kozeny fitting factor
K	Absolute permeability (m^2)
Q	Darcy flow rate
FF	Formation Factor
RI	Resistivity Index
a	Cementation factor
m	Cementation exponent
R_t	Resistivity of oil-bearing formation (ohm-meter)
R_o	Resistivity of water bearing formation (ohm-meter)
R_w	Resistivity of formation water (ohm-meter)
n	Saturation exponent
S_w	Water saturation
τ	Tortuosity of porous medium

N_A	Diffusive flux $\left(\frac{\text{moles}}{\text{m}^2 \text{ sec}}\right)$
D_{AB}	Open space diffusivity $\left(\frac{\text{m}^2}{\text{sec}}\right)$
D_{eff}	Effective diffusivity of the porous medium $\left(\frac{\text{m}^2}{\text{sec}}\right)$
C_{in}	Inlet concentration $\left(\frac{\text{moles}}{\text{m}^3}\right)$
C_{out}	Outlet Concentration $\left(\frac{\text{moles}}{\text{m}^3}\right)$
FF	Formation Factor

1 Introduction

1.1 Research motivation

It is projected that even with the current progress in the development of alternative energy resources, oil and gas will retain the largest share in the energy mix over the next three decades led by demand from transportation, petrochemicals, and electric power generation. By 2040, oil and gas are expected to make up more than half of the global energy mix. The non-OPEC liquid petroleum supply is expected to expand significantly, with the majority of growth in supply over the next decade coming from US tight oil [1]. The global oil production in 2019 grew by 2.2 Mb/D, more than double its historic average [2]. In addition to that, increasing attention is being given by the industry to enhance the sustainability of oil and gas production, thus requiring maximizing the production of the existing fields.

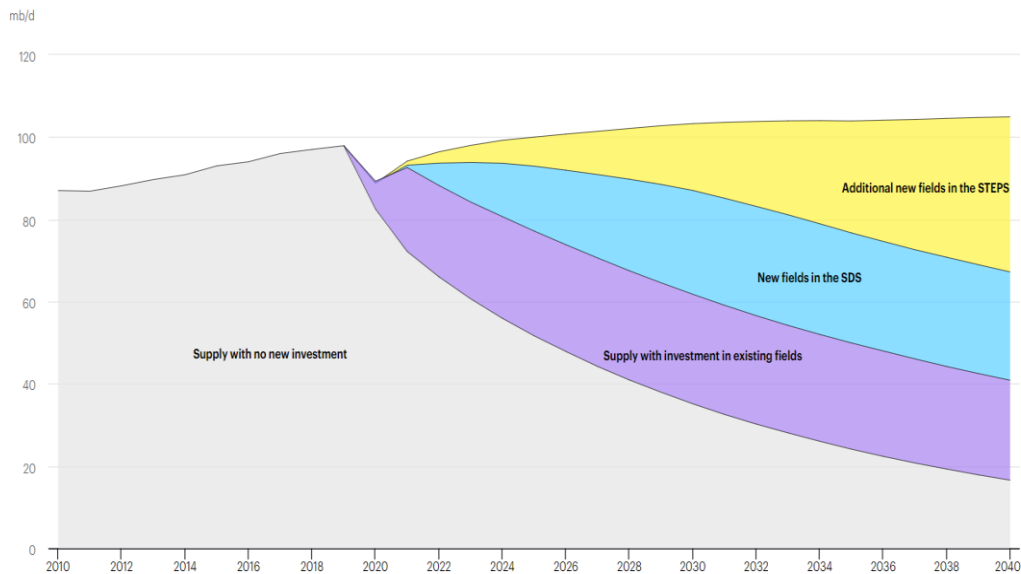


Figure 1: Global oil demand by scenario between 2010 and 2040, and declines in supply from 2019 IEA (2020), World Energy Outlook 2020, IEA, Paris <https://www.iea.org/reports/world-energy-outlook-2020> Stated Policies Scenario (STEPS), Sustainable Development Scenario (SDS) [3].

It is evident that growth in the developing economies of the world requires access to cheap energy supplies as increased access to modern energy, population growth, and improving living standards are achieved. Since energy is so important for human progress, society faces a twofold challenge: providing reliable and affordable energy to a growing population, while also lowering environmental impact, such as climate change threats. Technology holds the greatest potential to help society address this dual challenge [4].

Transport in porous media has an important role in oil and gas recovery and aquifer management in naturally occurring rocks and soils [5]. Transport processes strongly depend on the void and solid structural arrangements since transport essentially occurs around the solid obstacles. However, analysis of porous materials is not straightforward. Two materials having the same porosity may exhibit drastically different transport rates because of differences in pore size, shape, and connectivity, etc. [6]. For example, because of complex sedimentary and diagenetic processes carbonate rocks exhibit widely varying petrophysical properties that can vary over short distances within the reservoir. The goal of reservoir characterization is then to describe the spatial distribution of petrophysical parameters such as porosity, permeability, and saturation. These parameters are ultimately linked through pore size. Key decisions for reservoir production, such as completion schemes, reservoir management strategies and enhanced oil recovery methods, require a rigorous understanding of the fundamental controls on fluid flow at the pore scale. A model that accounts for the geometry and topology of the multiscale nature of carbonate reservoirs is therefore a critical step in understanding the role of pore architecture in the fluid flow process, particularly the interplay between macropores and micropores. Therefore, if the pore structure is correctly represented and initial conditions are clearly understood, then any emergent macroscopic fluid behavior can be accurately captured.

Carbonate reservoirs contain approximately 60% of the world's oil reserves and vast quantities of natural gas. Carbonate reservoirs have a diverse variety of pore types, structures,

geometries and connectivities, resulting in large variations in the petrophysical properties and flow mechanics. Vugs are commonly connected to the fractures or to the matrix [7]. Carbonates with dominant microporosity, such as sandstone with clay, tight gas sandstones and shale with nanoscale, are typical rocks which can be modeled as hierarchical geological media. One of the defining features of carbonate reservoirs is heterogeneity caused by the presence of microporosity. Not accounting for microporosity causes erroneous prediction of flow and electrical properties, e.g., relative permeability, capillary pressure, and formation factor. Such omissions leads to the assumption of high mobile water saturation which cause substantial underestimation of hydrocarbon reserves for instance [8].

Measuring the electrical resistivity of the water phase in the reservoir is a crucial tool for analyzing subsurface conditions. The relationship between resistivity and water content is described by the classic Archie's law (to be discussed in more detail in Chapter 2). Carbonate rocks commonly display non-Archie behavior attributed to porosity at difference length scales and the main reason for low resistivity at low water saturation in carbonates is the existence of connected intra-granular micro-porosity in the grain region of nearly all carbonate rocks [9]. This severely limits the ability of reservoir engineers to analyze the formation using the existing tools, which is a main motivation for better understanding the impact of microporosity in multiphase flow. In an oil reservoir after primary drainage most of the sub-resolution pores retain high brine saturation and in open hole log evaluation connected microporosity results in lower resistivity and thus incorrectly indicate high water saturation, this could be mistaken as a transition zone with overestimation of water saturation, S_w resulting in lower oil estimation by applying Archie's law or a transition zone may be incorrectly estimated as a 100% water zone, whereas a significant hydrocarbon volume may be present in the transition zone. This can occur due to short circuit of resistivity measurement caused by of water filled micropores resulting in underestimation of oil saturation by Archie's equation [10]. Thus, failing to correctly account for the microporosity where capillary bound water can cause higher S_w estimates using

conventional open hole logs. Therefore, while resistivity measurements can be used to predict permeability in normal rocks, this prediction fails in microporous rocks. The realistic 3D pore network modeling which accurately captures the pores and throats sizes and arrangement based on 3D images generated by X-ray tomography could help in evaluation of the impact of microporosity on the electrical parameters by correctly identifying the location, amount and type of microporosity in the reservoir facies thus greatly improve the estimation of transport properties and hydrocarbon reserves [11].

Recent advances in sub-micron scale imaging are providing new opportunities to model micropore systems and improving the attempts of understanding their impacts on reservoir-scale behaviours. Moreover, experimental evidence suggests that some specific types of micropores are oil-bearing, but can also contribute with secondary oil recovery through a time-dependent spontaneous imbibition process [12]. Therefore, recovery of residual oil from micropores could deliver additional economic benefits if such formations are carefully developed. The petrophysics of microporosity is fairly well-behaved and an abundance of this pore system may actually enhance predictive capabilities [13]. The microporous component in many reservoirs may be grossly underestimated and modeling techniques based solely on depositional texture or macroporous component are not capable of fully capturing the interplay of multiple coaxing pore systems and their petrophysical responses [14]. The pore scale characterization of complex carbonate rock has significant importance in the context of optimizing hydrocarbon recovery due to structural heterogeneity which results in complex spatial fluid distributions [9]. This in turn dictates where and how much oil is located and aids in reserves assessment.

Multiphase flow prediction in complex rocks is required to predict relative permeability curves which are input to reservoir scale simulations. However, this is still an area of active research to determine how the pore-scale configuration of various phases affects field scale recovery. We hypothesize that advanced pore-scale models of hierarchical porous media

incorporating multiple displacements, wettability conditions and different saturation paths can greatly contribute to improved understanding of multiphase flow behavior in complex rocks. The main objective of the present study/research was to develop a pore scale understanding of hierarchical reservoir media with the aim of enhancing oil recovery.

1.2 Objectives

The overall objective of this work was to present a new hybrid pore network extraction method. Since multiscale images of real porous media cannot currently be obtained from tomography equipment, as a first step multiscale images were artificially created that spanned several length scales. On the artificial images thus generated, the micropore regions was modeled as continua with effective properties, either obtained from network extraction of nanoscale tomographic image, or from correlations for related materials. The macropore networks were then stitched together with the continua scale, thus creating a hybrid hierarchical pore network. This approach, though conceptually simple, is the state of the art in multiscale PNM modeling [8], as will be discussed in Chapter 4.

Thus, a pore network model of the hierarchical reservoir rock was obtained by extracting pore networks from images that possess information at several scales in a single step. Once the method was successfully validated, the developed modeling framework was used to evaluate formation properties such as porosity, permeability, and formation factor on real images.

2 Background

This chapter explains the nature of the porous media and the challenges faced in modeling fluid flow in real porous media. Pore network modeling is a simplified representation of real porous media and is a suitable technique to model complex hierarchical porous media. Porous media is discussed in section 2.1, while Pore Network Modeling is discussed in general terms in section 2.2. Image Processing for digital porous media is discussed in section 2.3.

2.1 Porous Media

Porous media is ubiquitous in nature and industry, in the forms of sedimentary rocks, bones, teeth, and artificial media such as used in chemical reactors and Li-ion batteries where pores provide space to store fluids and facilitate chemical reactions, however the most economically important applications of porous media are in oil and gas reservoirs and in water aquifers. In this thesis porous media is defined as a material having pores or void spaces of variable sizes embedded in solid material that must be permeable to fluids of various types such as oil, water, and gases. Thus a true porous material should have a specific permeability, the value of which can be uniquely determined by its pore geometry and should be independent of the properties of the penetrating fluid [15].

Two important examples of porous media and its applications are in the field of petroleum engineering where sedimentary rocks such as carbonates, sandstones, shales, and gas hydrate accumulations found in shallow marine sediments, all of which have capability to store and produce huge quantities of oil and gas used to meet the worlds energy needs. Reservoirs traps found in these sedimentary rock formations can also serve as potential CO₂ storage. Another example is in the field of hydrology, also concerned with sedimentary rocks having large

aquifers where most of the world's fresh water is stored and there is an important need to protect these aquifers from contaminant transport.

The porous media is characterized in terms of its pore structure since the pore structure i.e., shape, size, orientation, and spatial arrangement of pores greatly influence the transport and storage capacity of porous media. The important properties which are discussed in this work for porous media characterization are porosity, permeability, pore size distribution, tortuosity, and formation factor. Hierarchical porous media is defined here as the porous media where multiple pore sizes with smaller and smaller pores are found as we zoom in with higher resolution. The pore sizes in hierarchical media could range from a high of 100 μm to low values of 100 nm and could be distributed like fractals i.e., self-similar shape at all scales.

2.1.1 Porosity

Porosity is an important property since it gives the storage capacity of the rock. Porosity is the fraction of pore volume found in a sample with a given bulk volume:

$$\phi_{total} = \frac{V_{pore}}{V_{bulk}} \quad (1)$$

The term 'effective porosity' is used to denote porosity that is available for fluid flow [14]. While inter-grain porosity in sandstones is a function of packing (decreases with closer packing), the pore size is controlled by size and packing of spheres. Sandstone porosity is affected by packing, sorting and cementation. Although the porosity of a pack of uniform spheres is independent of the grain size, in real materials such as carbonate sediments, the shape of the grains, presence of intragrain porosity and sorting all have a significant impact on porosity. While pore and throat sizes in sandstones are closely related to sedimentary particle size and sorting, in carbonates pore and throat sizes seldom show such a relationship. The sum of the porosity contributed from both the macropores and micropores is the total porosity of the sample:

$$\phi_{total} = \frac{V_{macro}}{V_{bulk}} + \frac{V_{micro}}{V_{bulk}} = \phi_{macro} + \phi_{micro} \quad (2)$$

where V_{macro} is the volume fraction of the macro-porosity region in the sample and V_{micro} is the volume fraction of the matrix region in the sample.

The impact of microporosity on total sample properties has been studied and it was found that various types of microporosity exist. Microporosity regions are important in determining fluid flow properties for carbonates rock showing at least one order of magnitude difference in the computed permeability [16].

Advanced imaging techniques have revealed that the microporosity can take on a wide variety of forms. Cantrell [17] has identified four important types of microporosity, namely: microporous grains, microporous matrix, microporous fibrous to bladed cements and microporous equant cements. Experimental evidence reviewed by Clerke et al. [12] reveals that not only are specific micropores oil-bearing, but they can even contribute to secondary oil recovery in the field through a time-dependent spontaneous imbibition process. Pore types control fluid flow and are thus very important rock characterization consideration to the petrophysical properties of the porous media [18]. Fullmer et al. [13] using Total Pore System Characterization, demonstrated that limestones having more that 80% microporosity exhibit favorable oil recovery and lower residual oil saturation due to homogeneous nature of micro-pore system. Remaining oil saturation values were found from primary imbibition measurements via water-oil centrifuge capillary pressure (P_c) experiments.

2.1.2 Microporosity

Microporosity has been defined by different sizes according to different types of microporosity found in the carbonate and tight sandstone and one cutoff size cannot be assigned

to microporosity. Several authors have categorized microporosity as pore sizes less than some given particular size while using classification of micropores, and macropores [19], [13], [20], [18]. In this work we have adopted the definition of Bultreys et al. [21], ‘micropores are defined as pores which are below the resolution of the micro-CT scan in question’, thus microporosity in our work will be called the matrix region having pore size which is below the micro-CT imaging resolution.

Hebert et al. [22] indicated that micropores often controls the connectivity of the sample, in samples tested they have found no percolating cluster where only macropores were considered however combining micropores with macropores resulted in a well-connected network. The presence of micropores increases the residual water saturation by defending from the non-wetting phase, while also offers escape routes to the trapped nonwetting phase inside macropores. In Estailades which is a micro-porous dominated carbonate and exhibits parallel dominated flow paths provided by intragranular pore filling nature of microporosity, Lin et al. [23] found that the presence of micro-porosity leads to higher initial water saturation and also provides additional connectivity resulting in lower residual oil saturation. However, the high permeability is Estailades is a result of well-connected macroporosity network indicating preference of fluids to flow through such a network where percolating network of macropores or vugs is available [21],[24],[25].

2.1.3 Permeability

Permeability is an important rock property that relates to the rate at which hydrocarbons can be recovered by application of pressure such as water injection into the reservoir. Permeability is a function of porosity, tortuosity, and pore and throat size. Unlike porosity, permeability varies with grain size, as well as packing and sorting. The absolute/effective permeability, K , of a medium is defined by Darcy’s law:

$$\frac{Q}{A} = \frac{K(P_{in} - P_{out})}{\mu L} \quad (3)$$

Different rock types have a range of permeability spanning around ten orders of magnitude, controlled principally by the variation in throat size and connectivity of the pore space. Most reservoir rocks have permeabilities in the range of 1 - 1000 mD, porosities around 0.1 to 0.3 and corresponding pore radius around 1 to 10 μm [26]. The relationship between permeability and pore size can be qualitatively understood by considering Hagen-Poiseuille equation for flow of fully developed Newtonian fluid through cylindrical pipe given by equation (4) below. Note the strong dependence of flow on the size of the tube R^4 , therefore in porous media flow through small pores is severely restricted even though there are a great many micropores.

$$Q = \frac{\pi R^4 \Delta P}{8 \mu L} \quad (4)$$

This nature of pressure driven flow in which preferential flow occurs through the connected macropore network affects the production flow rates in oil reservoirs having multiscale porous media. This type of behavior is known in the petroleum industry as dual porosity system and has been noted in tight naturally fractured reservoirs in which cross-flow of oil occurs from the tight matrix blocks into the fractured system and then produced through wellbores [27]. In cases where macropores are shielded by the micropores, permeability and hence flow rate can be drastically impacted.

2.1.4 Pore size distribution

Pore size distribution refers to the range of all the pore sizes in the sample. Mercury intrusion porosimetry is the most common method of measuring pore size distribution. The pore size obtained by this method is referred to as pore-throat size and is defined as the pore size that connects the larger pores. In the primary drainage process modeled in the porosimetry experiment the pore space is initially filled with the wetting phase. Then the non-wetting phase

is forced to penetrate from the inlet and the applied pressure is increased in small increments. Initially the non-wetting phase penetrates only the largest pores adjacent to the surface of the porous medium. As the non-wetting phase pressure is increased progressively more of the pore space is accessible until the smallest pores are penetrated. From the measured capillary pressure vs wetting phase saturation curve the derivative of saturation with respect to the logarithm of capillary pressure is used to find the throat size distribution. While the throat radius at that particular capillary pressure is calculated from the Washburn equation assuming contact angle of zero if one of the fluids is non-wetting such as mercury.

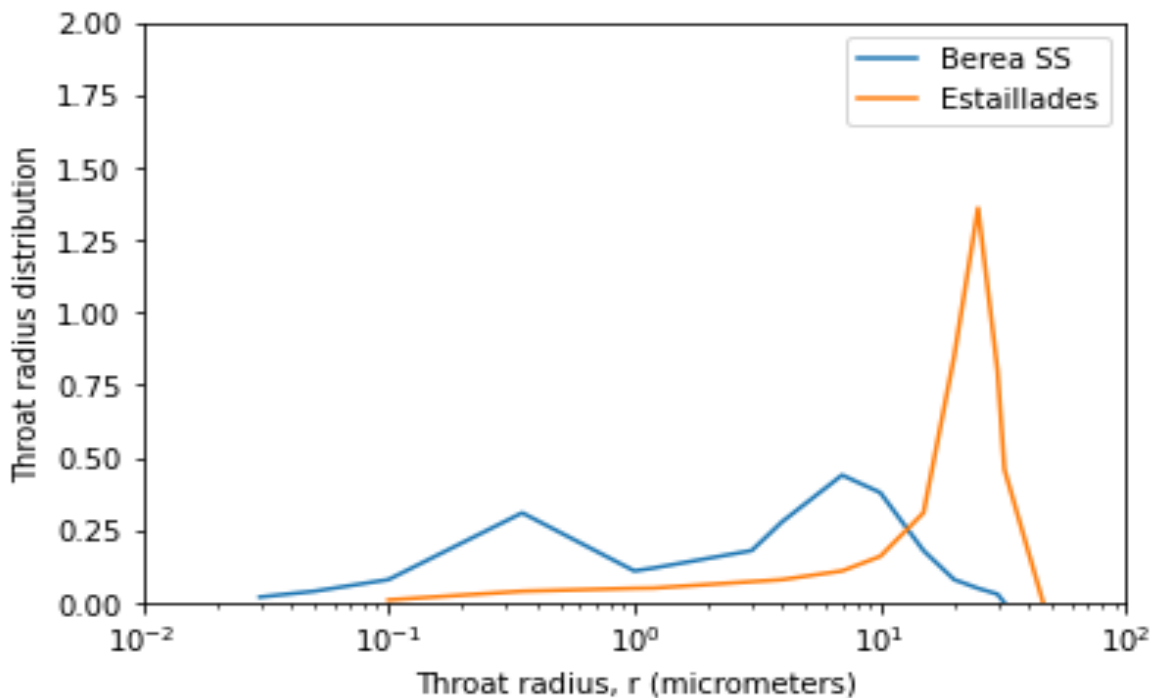


Figure 2: A typical pore size distribution curve for Berea sandstone (blue) and Estailades carbonate (orange)[26]

An illustrative primary drainage capillary pressure curve for Berea sandstone and Estailades carbonates and pore size distribution curves are shown in Figure 3 and Figure 2 respectively.

The Estailades shows a dual porosity behavior with bimodal pore size distribution since the rock is known to contain two types of pores: well-connected intragranular macropores and intragranular micropores within the grains. While the Berea sandstone indicating unimodal pore size distribution has a homogeneous arrangement of large pores.

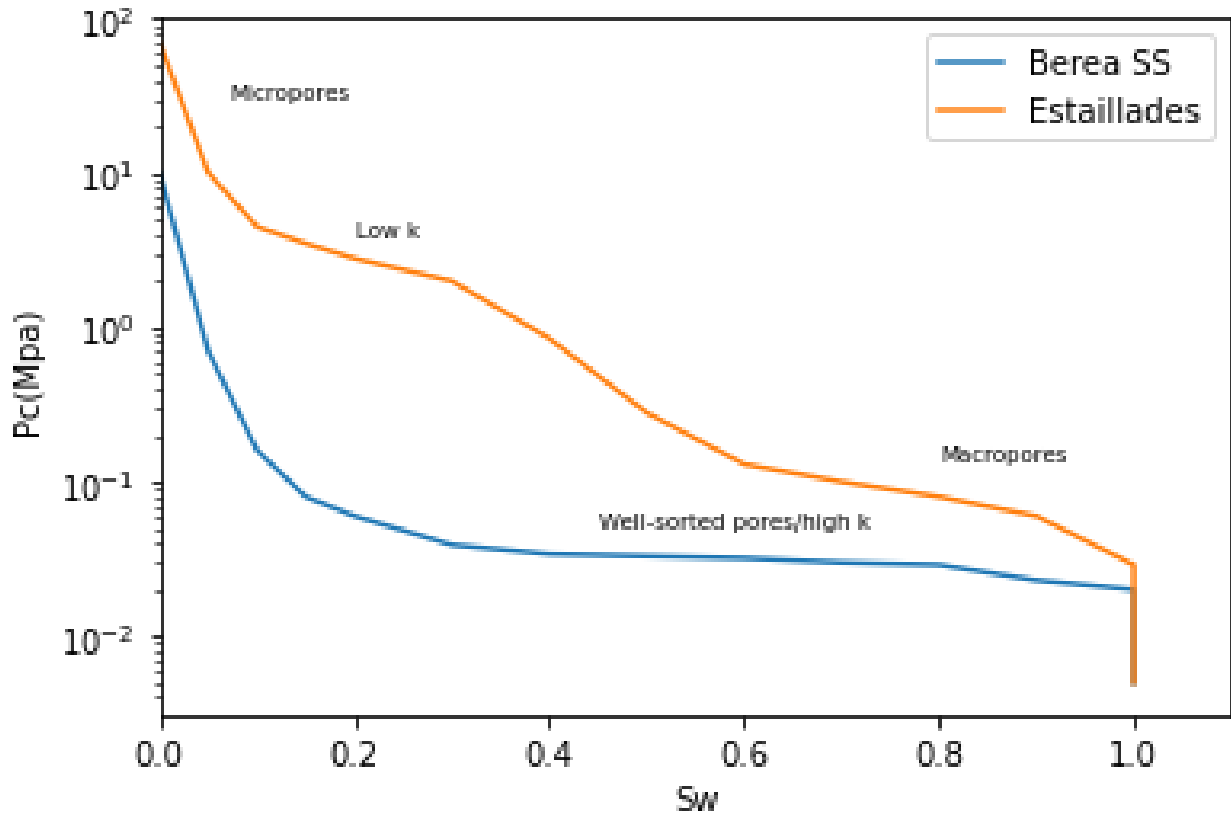


Figure 3: A typical capillary pressure vs saturation curve for Berea sandstone (blue) and Estailades carbonate (orange) [26]

2.1.5 Tortuosity

Tortuosity has been defined as the ratio of effective flow path L_e , to the macroscopic length L (sample length):

$$\tau = \left(\frac{L_e}{L}\right)^2 \quad (5)$$

We explain below the definition of tortuosity using Fick's law. The Fick's law of diffusion for a species A in a mixture of species A and B is written as follows:

$$N_A = -D_{AB} \frac{d_{c_A}}{d_X} \quad (6)$$

While diffusion through a porous media treated as a continuum and be written as

$$N_A = -D_{eff} \frac{d_{c_A}}{d_X} \quad (7)$$

where $D_{eff} < D_{AB}$, the effective diffusivity accounts for reduction in flux due to two factors, the presence of solid obstacles, i.e., reduction of space being taken into account by porosity and the additional path that the molecules must travel to avoid the solid obstacles, taken into account as tortuosity. Hence equation (7) can be written as:

$$N_A = -D_{AB} \frac{\phi}{\tau} \frac{d_{c_A}}{d_X} \quad (8)$$

Equating equation (7) and equation (8),

$$\frac{D_{eff}}{D_{AB}} = \frac{\phi}{\tau} \quad (9)$$

Since obtaining tortuosity value for a porous medium is experimentally difficult, many correlations have been proposed based on other more easily measured parameters. In porous media the most applied is the Bruggemann correlation for spheres. Since the shape of the particles in real rocks are much more complex than simple spheres, the tortuosity value estimated from the Bruggemann correlation will be an underestimation and therefore in real sandstones we should expect higher tortuosity and lower effective diffusivity.

Various forms of tortuosity has been defined [28] in the literature:

- Geometrical: in terms of path length
- Electrical: in terms of electrical conductivity of medium
- Diffusional: in terms of temporal changes in concentration as explained in this work
- Hydraulic: normally defined in geometrical terms

In tight formations, diffusional tortuosity is important because diffusion can occur through the microporosity with relative ease compared to fluid flow. Note that there is no size dependence in the definition of tortuosity. It has been demonstrated in the literature, Hedley et al. [28], that for a porous medium electrical and molecular diffusivities are equivalent. Therefore, electrical tortuosity can represent the diffusional tortuosity as explained above.

2.1.6 Formation Factor and Resistivity

The formation factor, FF measures the influence of pore structure on the resistance of the sample by measuring the electrical transport properties of a porous media and is related to porosity and pore structure.

$$FF = \frac{R_o}{R_w} \quad (10)$$

where R_o is the resistivity of water bearing formation and R_w is the resistivity of formation water. Note that due to the analogy between diffusion and electrical conduction of ions, we can also write:

$$FF = \frac{D_{AB}}{D_{eff}} = \frac{\tau}{\phi} \quad (11)$$

FF is usually correlated using a more practical relationship that is the Bruggeman equation, known as Archie's law:

$$FF = \frac{a}{\phi^m} \quad (12)$$

where m is the cementation exponent, the value of m reflects the tortuosity of current flow and in general its value varies with the degree of cementation as rock becomes more consolidated [29]. The structural parameter, a is a cementation factor and has been attributed to the interstitial structure of the rock. Theoretical and experimental investigation showed that a and m vary mainly with pore geometry, hence depends on the rock type. Thus, the significance of formation factor is that its value is uniquely determined by the pore geometry [15]. The equation above when written in log format is used to make a log-log plot of FF vs ϕ which yields a straight line from where values of a and m are determined as shown in Figure 4. In petroleum industry FF vs ϕ and FF vs k relationship for a particular formation is determined from laboratory measurements on number of core samples. The values of a and m are thus obtained for a specific formation from measurements of FF and ϕ values determined either from laboratory measurement on core samples or from well logs.

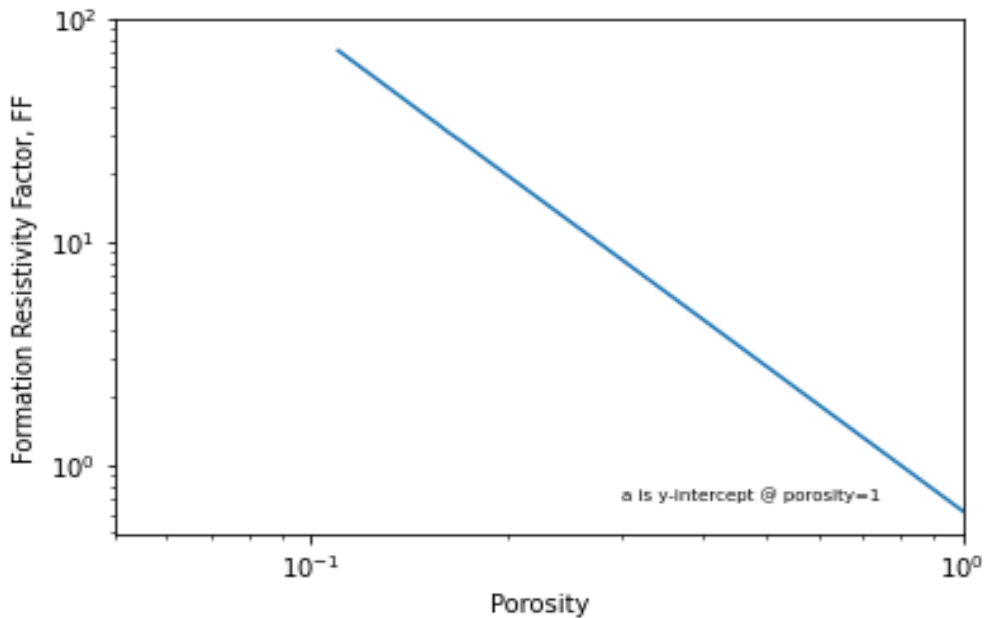


Figure 4: FF vs ϕ log-log plot of a formation to determine the formation specific parameters [30].

The values of a and m are then used in the Archie's equation to determine water saturation which is an input parameter in the calculation of oil and gas reserves. Thus, the values of a , m and n used in the Archie's equation below are critical in the determination of S_w and ultimately oil and gas reserves.

$$S_w = \left(\frac{R_w}{R_t} \frac{a}{\phi^m} \right)^{\frac{1}{n}} \quad (13)$$

where, R_t is the resistivity of the oil-bearing formation and n is termed as the saturation exponent with values close to m . The value of n is known to depend on the wettability of the rock. Resistivity index RI is defined as the ratio of the resistivity of the partially water-saturated rock, R_t , to the resistivity of the fully water-saturated rock, R_o :

$$RI = \frac{R_t}{R_o} = S_w^{-n} \quad (14)$$

Resistivity index is known to be affected by the pore structure and saturations. In one study it was found that $RI-S_w$ curve of a rock "bend upwards" in dual porosity systems, with the inflection point being related to the fractional partitioning of macro-porosity and micro-porosity [9]. In another study pore network modeling showed that the microporosity fraction influences Archie n and thus S_w . In a real field case study, it was found that micropores have excellent connectivity in 3D [19].

By combining actual fluid velocity within the pores with the macroscopic velocity in Darcy's law it can be shown that permeability is inversely proportional to the tortuosity. Since both the electrical conductivity and the permeability of a porous medium are determined by the effective length of the path of flow of ions. The greater this length the lower the conductivity and the permeability, hence as the effective length of the path of flow of ions increases tortuosity

increases, permeability decreases and FF increases. Formation factor is the electrical analog to absolute permeability, while RI is the electrical analog to relative permeability. Based on experimental studies on core plugs Archie concluded that there exists a relation between FF and k as highlighted in figure below. Bassiouni et al. suggested an empirical relationship of the following form [30], the relation also verified in various experimental studies.

$$FF = Ak^{-B} \quad (15)$$

where A and B are formation specific constants. Formation factor estimation method used in this thesis is further explained in section 4.1.3.

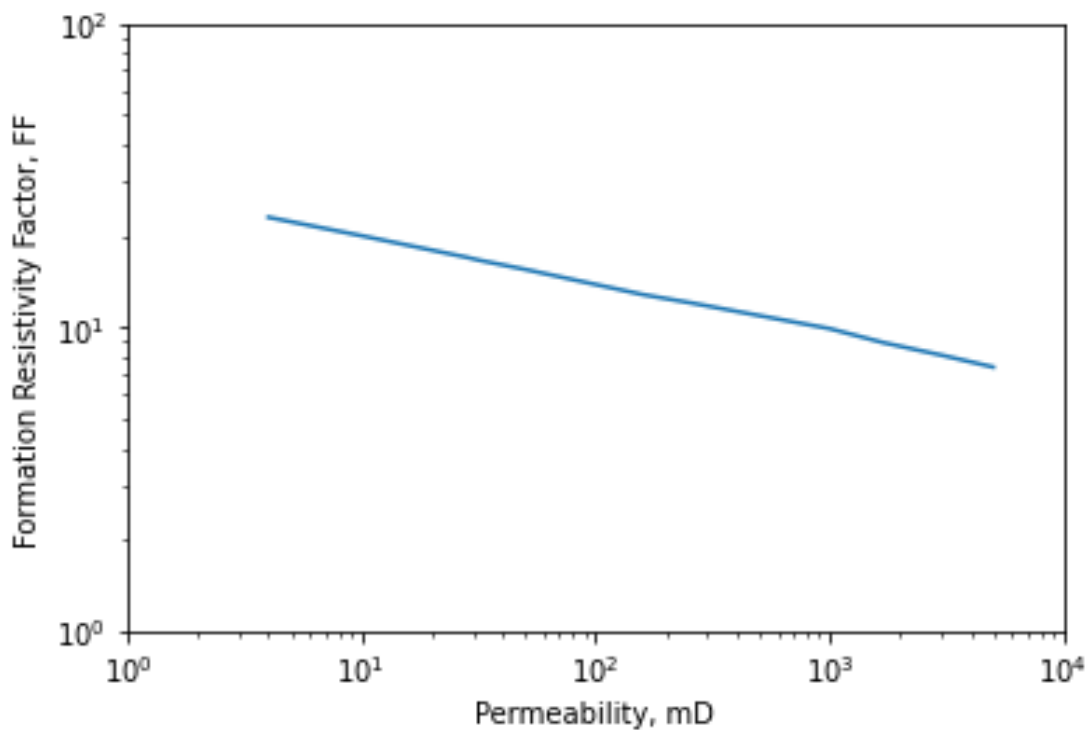


Figure 5: A plot of Formation Factor vs Permeability for U.S. Gulf coast formation [30].

2.2 Pore network modeling – General review

One of the problems encountered in pore scale modeling of geological materials is the multiple spatial scales inherent to the pore structure of complex rocks such as carbonates and tight sandstone with mud. This means that it is not possible to capture the wide range of pore sizes in one single imaging experiment, due to limited resolution and sample volume of these experiments. The discrepancy between these scales, which might be several orders of magnitude, poses computational problem. For instance, in a carbonate or sandstone sample of 1 cm across, large vugs or pores may be present which are 100s μm across, combined with micro-porosity or clay with structure down to 0.01 μm . Hence, to resolve the smallest pore space in this small rock sample require an analysis over six orders of magnitude (from 10^{-8} to 10^{-2} m). Therefore, it is useful to have a simplification that retains the connectivity of the pore spaces as well as geometric information [26].

Pore network models (PNMs) are a suitable technique for multi-scale simulations of this kind, because these models describe individual pores as a single unknown element and are thus computationally efficient [21]. Pore-network modeling was first introduced by Fatt [31] in 1956, who exploited the analogy between flow in porous media and a random resistor network and introduced interconnectivity and spatial heterogeneity; which was in contrast to the prevailing representation of pore space as bundle of parallel tubes. In his two-dimensional model the electrical current represented flow, while the voltage difference was equivalent to the pressure drop. This was possible due to the analogy between Poiseuille's law and Ohm's law. Note that his 'model' was an analogue computer which literally consisted of wires and resistors.

Pore network modeling is based on the recognition that, in many applications, an approximate model of a suitably large domain is more effective than a highly rigorous model of a limited number of pores. The modern concept of PNMs is to map the pore space onto a discrete network

of pores and connecting throats, then use transport algorithms based upon nodal balances (i.e., resistor networks) of transported fluids to run simulations. In addition to speed and simplicity, PNMs have some advantages over the more commonly used continuum models. PNMs can solve realistic saturation profiles and have a direct connection between structure and topology of the porous material and transport processes.

In this network model, each throat represents a resistor e.g., the throat constriction causes resistance to flow because of its geometry, as well as the fluid properties such as viscosity. The resistance in PNMs is described by an appropriate pore-scale physics model, such as Hagen-Poiseuille model for single phase flow in a cylindrical tube:

$$q_{ij} = \frac{\pi R_{i-j}^4 (P_i - P_j)}{8\mu L_{i-j}} \quad (16)$$

where P_i and P_j are the pressures in pores i and j , L_{i-j} and R_{i-j} are the length and radius of the throat (pipe) connecting pores i and j , and μ is the fluid viscosity. Assuming each pore-throat-pore conduit Figure 6 as a cylinder we can find the hydraulic conductance using the above equation (16). Then conservation of mass is applied around each pore as given in Equation (20).

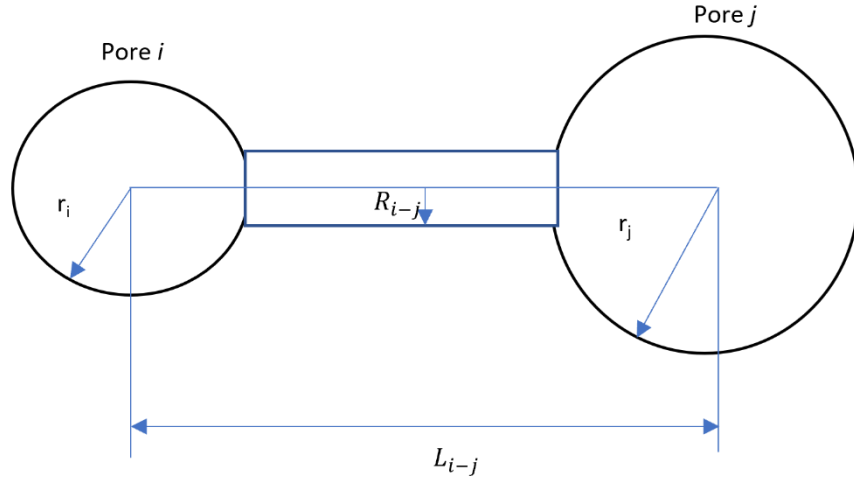


Figure 6: A pore-throat-pore schematic diagram for hydraulic calculations

The above equation for n neighboring pores can be stated as:

$$q_{ij} = \sum_{j=1}^n g_{h,ij}(P_i - P_j) \quad (17)$$

where q_{ij} is the flow rate from pore i to pore j , $g_{h,ij}$ is the conduit's hydraulic conductance between pores i and j . The hydraulic conductance for each section of half pore i , the conducting throat $g_{t,i-j}$, and half pore j are calculated as three resistances in series as follows.

$$g_{h,ij} = \left(\frac{1}{g_{p,i}} + \frac{1}{g_{t,i-j}} + \frac{1}{g_{p,j}} \right)^{-1} \quad (18)$$

When the pressure loss in each half pore is neglected for simplicity then the total flow rate Q through a single pore can be generalized as:

$$Q_{ij} = \sum_{j=1}^n g_{h,ij}(P_i - P_j) \quad (19)$$

At steady state and in absence of any source or sink terms, the net material flow through pore i is zero, hence Eq.(19) can be recast as:

$$0 = \sum_{i-j}^n g_{h,ij}(X_i - X_j) \quad (20)$$

where pore i has n neighbors and X is the unknown to be solved for. When the above equation is applied to each pore in the network it generates a system of linear equations in X that can be readily solved by any matrix inversion algorithm subject to given boundary conditions.

When the unknown X represent the pressure, applying equation (20) to all pores in the network generates a linear system that can be solved for the pressure in each pore system. This result in a system of equations such that

$$P = A^{-1}b \quad (21)$$

where P is the unknown pressures to be solved, A is the coefficient matrix of hydraulic conductance and b is the boundary condition. Basically, equation (21) states that if the inverse of the coefficient matrix exists and can be found, the solution of the system of equations for unknown P , can be obtained by pre-multiplying the known boundary conditions vector b , by the inverse of the coefficient matrix, A^{-1} .

Having determined the pressures P of all pores, the flow rate leaving the sample can be computed by summing the rate for all boundary pores. Once rate, Q , through the entire network calculated by the summation of flow rates across all throats connected through the inlet (or

outlet) pores is known, to determine permeability coefficient use Darcy's law with imposed pressure at the boundaries, P_{in} and P_{out} , on the network of length l :

$$K = \frac{\mu Q l}{A(P_{in} - P_{out})} \quad (22)$$

Similar to the above approach for calculating permeability, the formation factor which is the electrical analog to the permeability is calculated using Fick's law of ionic diffusion due to concentration difference. The diffusive conductance for each half pore, throat and half pore element are calculated by resistors in series analogy similar to equation (18) using diffusive conductance in place of hydraulic conductance of the form, as explained in detail in section 4.1.3

$$g_d = \frac{D_{AB} A}{L} \quad (23)$$

Assuming steady state with no generation or consumption of ions, net mass flow through a single pore is zero. The system of linear coupled equation is then solved to find value of concentration in each pore with applied concentration difference for the entire network. Having determined concentration in each pore the diffusive flow rate is then calculated. Once the mass flow rate through the entire network is known, the effective diffusivity of the whole domain is determined by applying Fick's law with imposed concentration at the boundaries. The formation factor is finally determined as the ratio of bulk diffusivity in open space to the effective diffusivity of the medium.

2.3 Image Processing and Analysis

Image processing and analysis includes correcting imaging defects, image enhancement operation, segmentation and thresholding and processing binary images. The `scipy.ndimage` packages by SciPy.org, has been used in this thesis, the package includes a

number of general image processing and analysis functions that are designed to operate with arrays of arbitrary dimensionality. Image processing fundamentals are briefly discussed below [32].

2.3.1 X-ray Imaging

The common approach to image the pore space of rocks is to use a laboratory micro-CT instrument that houses its own source of X-rays. The dependence of the X-ray absorption on the composition and geometry of an object allows to make radiographies, by placing the object in between an X-ray source and detector. These are basically shadow images and thus projections of a 3D object on a 2D plane getting 2D slices. However, by rotating the object around an axis and acquiring radiographies from multiple angles, the 2D slices are then stacked to construct three-dimensional images of the rock sample as illustrated in Figure 8. The image resolution is determined primarily by the proximity of the rock sample to the source. The magnification of the projected image is the ratio $(a + b)/a$, see Figure 7. Thus to obtain a high resolution image, it is necessary to scan a smaller sample which is placed closer to the X-ray source [26] since the geometric magnification rapidly degrades with increasing sample size.

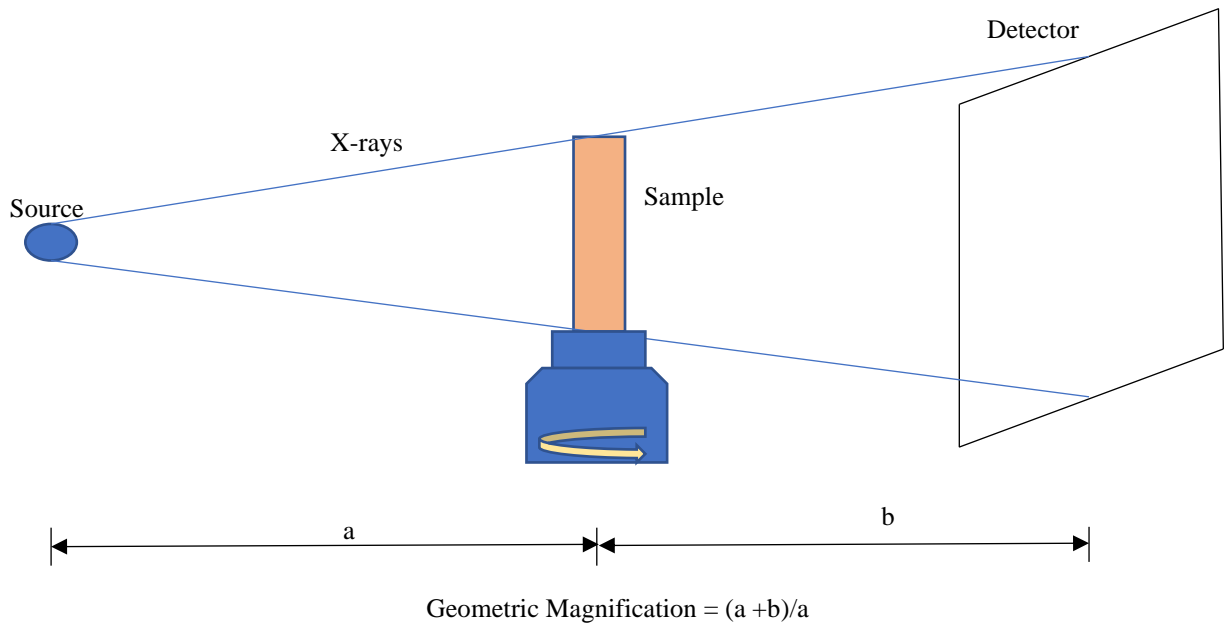


Figure 7: A simplified Illustration of a cone-beam imaging system.

For micro-CT devices, typical X-ray energies are in the range 10 – 160 keV – with corresponding wavelengths 0.1 – 0.01 nm. Current micro-CT scanners produce images of around 1000^3 – 2000^3 voxels. To obtain a representative image, the cores are normally a prepared a few mm across, constraining resolution to a few microns per voxel.

In a bench top instrument with its own X-ray source, an electron beam strikes a target to produce X-rays that pass through the specimen, which is mounted on a rotating and translating sample holder placed in front of the X-ray detector. By accelerating an electron beam to a small focal spot on a metal anode, often made of tungsten here the sudden deceleration of the electrons produces a conical X-ray beam. This results in a geometrical magnification of the object on the detector. The resolution is limited by the minimal focal spot size of the X-ray tube and by the

geometrical magnification which can be achieved. The intensity of the transmitted X-rays, which can be set for characteristic energies to achieve element-specific imaging can then build up a series of projected views from which tomographic reconstruction can be performed as highlighted in the figure below. After conversion to visible light by a phosphor or channel plate and appropriate intensification, the projected images can be collected using conventional solid state detector arrays.

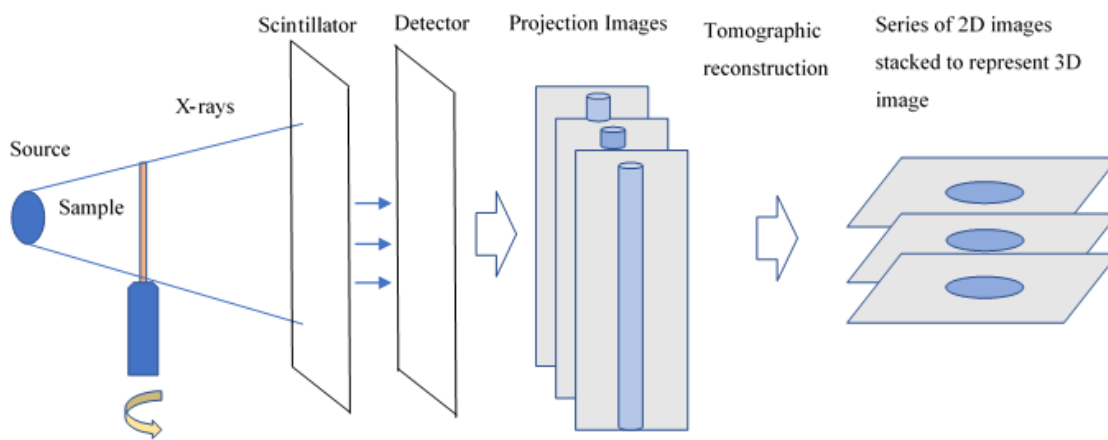


Figure 8: Schematic illustration of X-ray CT acquisition and reconstruction process.

2.3.2 Image Representation

Digital representation of porous media at pore scale are basically mathematical arrays with values in each element. For example, in 2D binary images which comprise of ‘Pixels’, a value of 1 represents void and 0 represents solid. Stacks of 2D images where the third dimension represents the height make a 3D image in which the basic element is called a ‘Voxel’.

2.3.3 Correcting Imaging defects

This describes image processing operations and procedures that can be applied to correct some of the defects in as-acquired images that may occur due to several causes such as: imperfect detectors, limitations of the optics, inadequate or non-uniform illuminations, etc. The image processing does not add anything to the image but only removes or reduces one portion of the image content so that others may be better seen or measured. The common way uses neighborhood averaging which replaces each pixel with average of itself and its neighbors. This is often described as a ‘kernel’ operation since implementation can be generalized as the sum of pixel values in the region multiplied by an array of numeric weights.

2.3.4 Image Enhancement

This involves enhancing the visibility of one portion of an image by suppressing the visibility of another portion and is done simply to make image easier to visually examine and interpret. Image mathematical operations such as addition, subtraction, division, and multiplication use two images to produce a new image. These operations are performed pixel by pixel such that the sum of two images contain pixels whose brightness values are sum, ratios, or differences of the corresponding values in the original images. Image addition is used for averaging of images to reduce noise. Adding images together can in some cases be helpful to create composites, which help to communicate complex spatial relationships. Image subtraction is used to level images by removing background. Subtraction is also a way to discover differences between two images. Multiplication operation is used to superimpose one image on another, for example to add texture to a surface [32] which refers to image variability or brightness values.

2.3.5 Segmentation and Thresholding

Selecting objects or features within an image is an important requirement which entails checking each individual pixel in the raw image to see whether it belongs to the object of interest

or not. The simplest way is to define a range of brightness values in the original image, select the pixels within this range as belonging to the foreground i.e., region of interest, which is the pore space, and rejecting all the other pixels to the background or the solid phase. The selection process is usually called thresholding. The resulting image is then displayed as a binary or two-level image, using black and white to distinguish the regions. Image segmentation is a crucial step in image processing since it impacts subsequent analysis such as pore network generation. Image segmentation can be defined as the process of assigning a label for example, a unique number, to each pixel in an image such that pixels with the same label have similar characteristics. An illustrative example of three-phase segmentation is shown in Figure 9.

The brightness histogram of the image is used for thresholding the image. The histogram counts pixels with each brightness, the typical image digitalization process produces values from 0 (black) to 255 (white), producing 1-byte (8bit) values. Thus, for typical 8-bit monochrome image, the brightness scale represents 2^8 or 256 grayscale values. The image histogram, a plot of the number of pixels with each possible brightness level i.e., 256 possible values, is a valuable tool for examining the values in the image. The premise behind thresholding with the histogram is that a peak indicates that many pixels have nearly the same brightness and therefore represents the same type of object. Typically, voxels with darker shades represent the pore-space while brighter grayscale values correspond to solid phase. In two-phase segmentation the grayscale histogram consists of two distinct peaks that define the solid and void phases. In three-phase segmentation as used in this work there is a region that lies between the two peaks that is unresolved by micro-CT device and is categorized as microporosity.

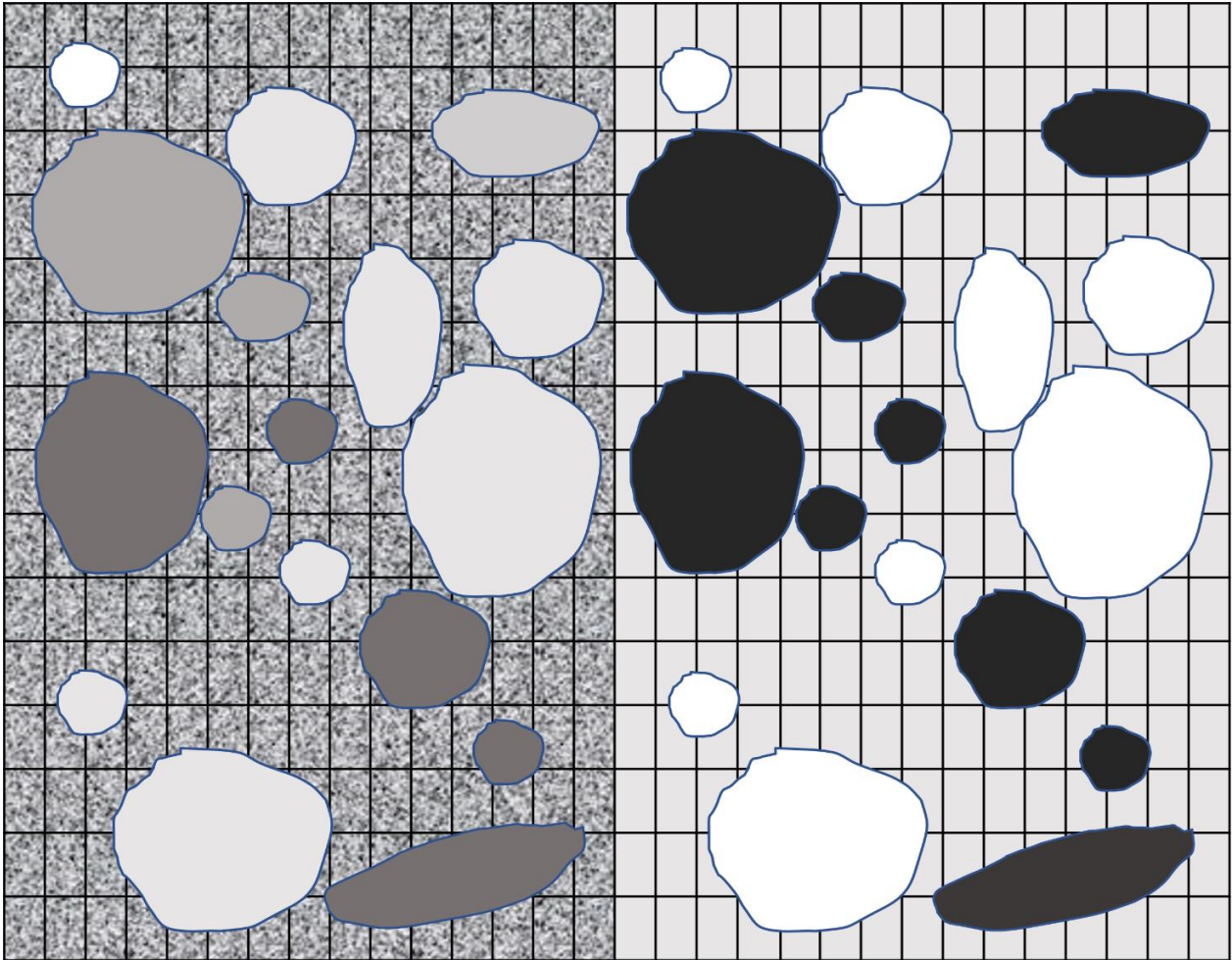


Figure 9: A grayscale image on left showing void in light gray, grains in dark gray and matrix in the background with microporosity which cannot be clearly distinguished. On the right is the segmented image with void in white, grains in black and matrix in darker gray.

2.3.6 Binary Images

Morphological operations modify individual pixels in the binary images based on their local neighborhood. These operations function by dealing with array of pixels. The important morphological operations are Dilation, Erosion, Opening and Closing.

Dilation is the operation of expanding objects in an image by a specified amount and is accomplished by scanning through an image and replacing each 0 with a 1 if any pixel in its neighborhood are 1s. This adds a layer of pixels around the periphery of all features and regions, increasing their dimensions and sometimes cause features to merge. It can also be used to fill in small holes within features. Erosion removes pixels from features in an image by replacing 1s if it has neighbors of 0 and is used to remove pixels that do not lie within the large regions of brightness. The combination of an erosion followed by a dilation is called an opening operation and used to open gaps between just-touching images i.e., to separate touching features and for removing isolated pixel noise from binary images. Performing a dilation followed by an erosion (both with the same structuring element) is called closing. The result is to fill places where isolated pixels are 0s such as missing pixels within a feature.

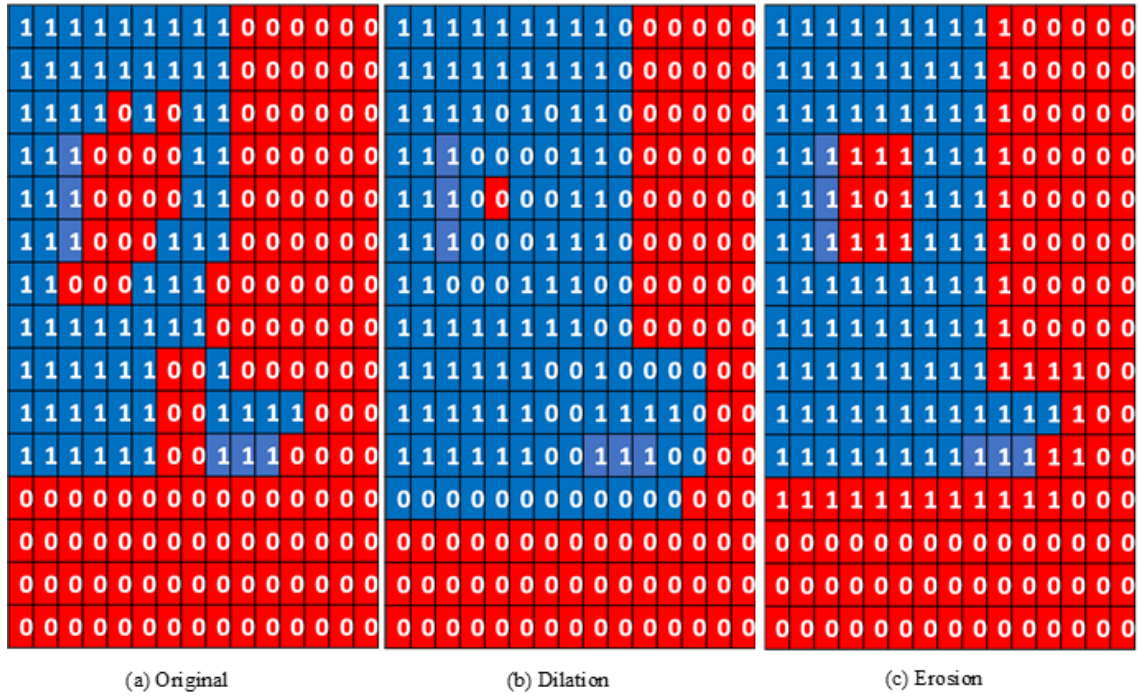


Figure 10: Closing operation - Dilation of the original image followed by Erosion of the dilated image using the same structuring element.

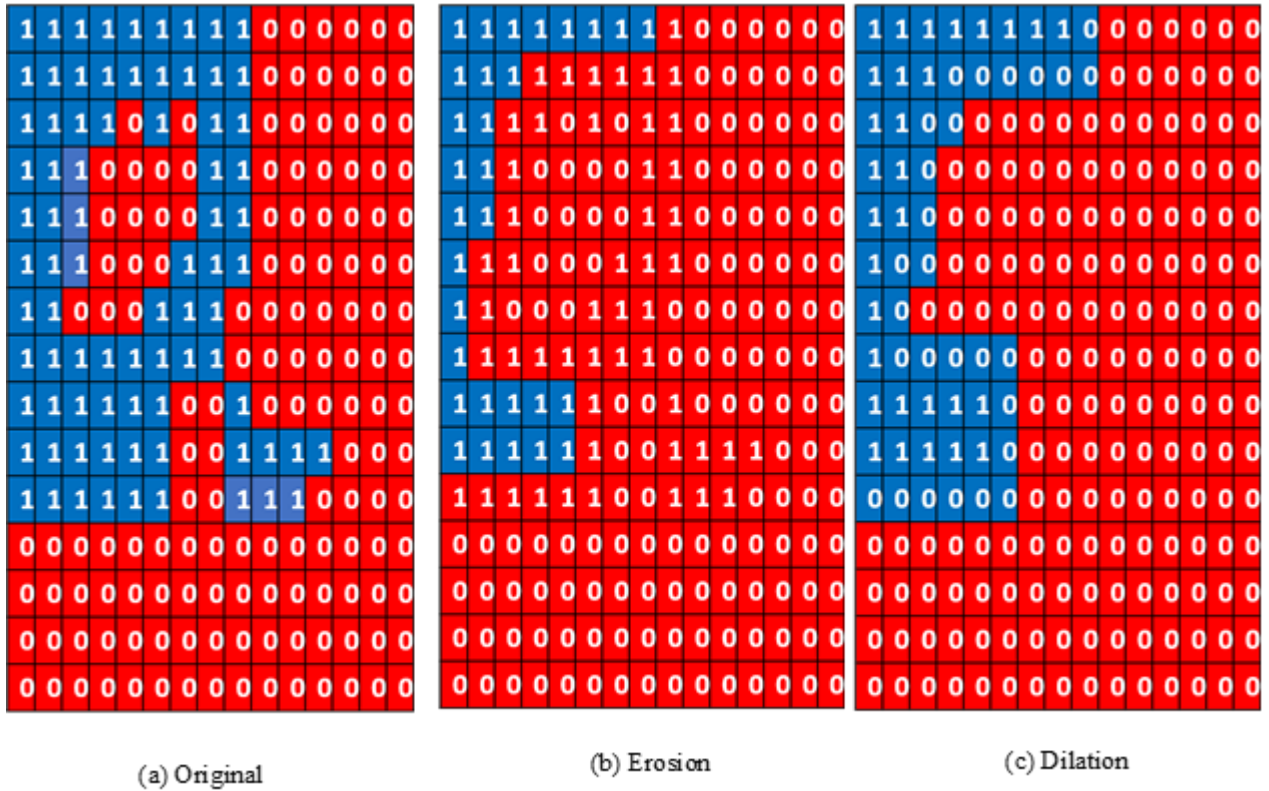
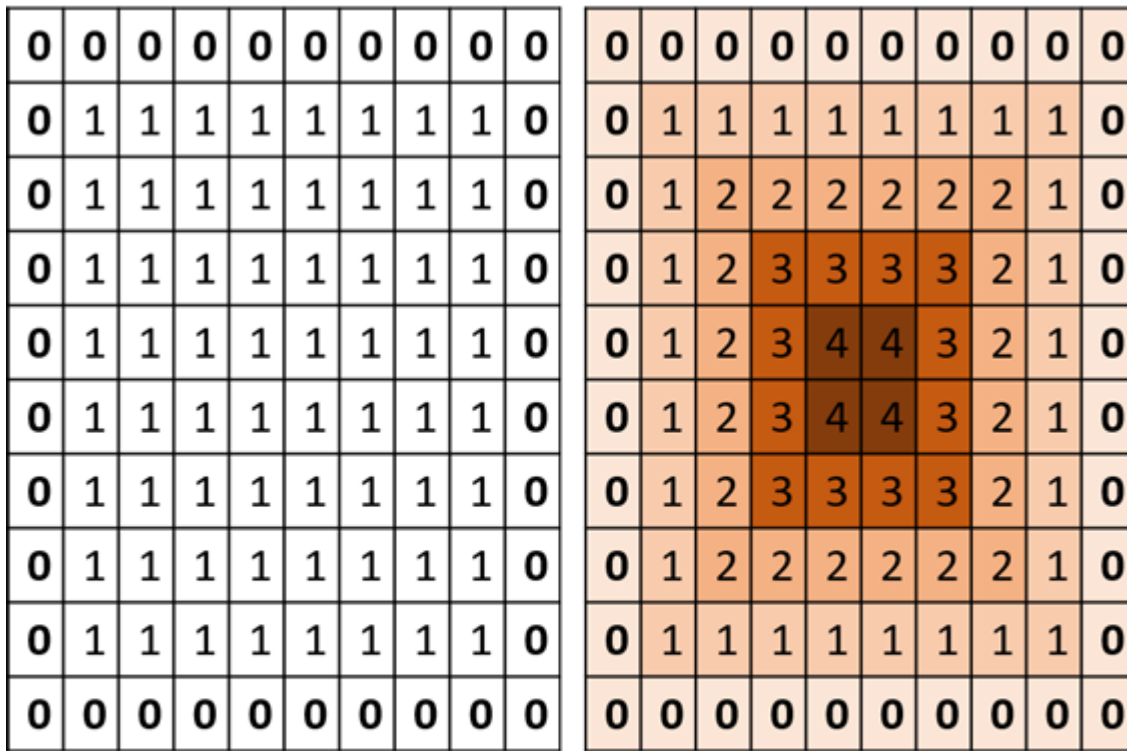


Figure 11: Opening operation - Erosion of the original image followed by dilation of the eroded image using the same structuring element.

2.3.7 Distance Transforms and Watershed Segmentation

Distance transform applied to binary images results in a grayscale image with gray level intensities of points inside foreground regions (pixel 1) changed to show the distance to the closest solid boundary (background, pixel 0). Thus, showing the distance of each void voxel to the nearest solid voxel. The gray level intensity corresponds to Euclidean distance. Hence the name Euclidean distance Map as shown in Figure 12 below:



(a)

(b)

Figure 12: Euclidean distance transform applied to the binary image (a) on the left resulting in the (b) graylevel image shown on the right.

Watershed segmentation is used for separating touching convex features in an image. The brightness values of each pixel in EDM are visualized as a physical elevation, each feature then appears as a mountain peak, as a result the larger features have higher peaks. Thus, watershed method first builds a distance map of the pore space, the pore space is then partitioned into regions associated with each pore by treating the distance map as a topological contour. Since

flooding should start from the lowest point. This minimum is obtained by applying a negation operation inside each catchment basin which results in the maximum becoming the minimum.

In accordance with the watershed analogy, fictitious water is applied to the image, and collects in each basin, which become pore regions, with ridge between them becoming the throat. The watershed process used in this work for segmentation is explained in detail in section 3.1.

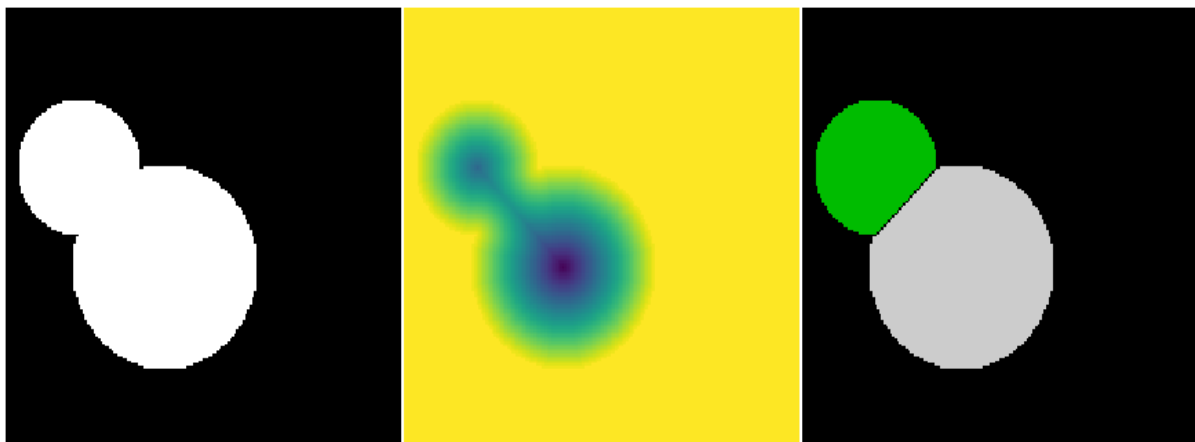


Figure 13: Two touching objects, their distance transform and watershed segmentation showing the ridge line

3 Literature Review

This chapter presents a literature review on pore network extraction methods and the current status of pore network modeling. Section 3.1 covers a review of current efforts on pore network extraction methods and the method developed in this thesis. Section 3.2 covers current multiscale pore network models for complex porous rocks, examples of which are carbonate rocks with lot of microporosity and clay-bearing sandstones, efforts on making representative models and typical output of those models are also discussed.

3.1 Pore network extraction

By definition a network representation is a partitioning of the void space to preserve approximately, the connectivity and other useful geometric information [26]. We will briefly discuss the more commonly used extraction methods where the pore network model is directly constructed by segmenting voids and throats of porous media using image processing techniques. The three common methods are medial axis, maximum ball, and watershed segmentation. Among the three methods, watershed segmentation is one of the most popular methods since it is efficient and extracted network definition provided by the watershed algorithm does serve as a reasonably consistent, robust, and useful characterization of the pore space.

In the medial axis method, a pore space skeleton that runs approximately in the middle of the void region is identified. The pore space skeleton is achieved by shrinking the pore space voxel by voxel iteratively until a cross section through a pore becomes a single voxel, thus pore bodies are identified as the branching points of the medial axis. While medial axis has the advantage that it provides direct relationship to the topology of the original image, the method suffers from

the disadvantage that pore space is not clearly identified i.e. geometrical pore bodies obtained do not necessarily coincide with the actual pore bodies [8].

The maximal ball algorithm was proposed by Silin and Patzek and later refined by Blunt and co-workers. In this method, spheres centered on each voxel are grown until they touch the nearby solid. These spheres are called maximal balls. A sphere that is larger than any other sphere that it overlaps uniquely defines a pore and is named an ancestor. The algorithm then builds a family of cascading smaller spheres and eventually finds one ball that is a child (intersection) of two families. This defines the throat or restriction that separates two wider regions of pore space. The maximal ball method suffers from two drawbacks: due to discrete nature of pore-space images the method can find multiple connections with spheres of apparently equal size between the same pores; and the unclear distinction between a pore and a throat [26].

The watershed algorithm technique is one of the most popular one due to its relative ease of implementation and robust identification of pore and throats. This idea was first presented by Thompson et al. [33] and Sheppard et al. [34] but has been extended by recent work. This method first builds a distance map of the pore space, this is the distance from the center of a void voxel to the nearest solid. The pore space is then partitioned into regions associated with each pore by treating the distance map as a topological contour. In accordance with the watershed analogy, fictitious water is applied to the image, and collects in each basin, which become pore regions, with ridge between them becoming the throat.

Rabbani et al. [35] presented an algorithm adapting watershed to rock materials and producing 3D and 2D networks. The main steps in their algorithm are applying a distance transform to binary volume data, performing median filtering for smoothing the distance transform, and lastly applying watershed segmentation by pixel flooding to label all detected pores and throats for network extraction. Gostick [36] made an improvement to the method of

Rabbani et al. by removing several types of spurious peaks in the distance transform that leads to over-segmentation in the watershed step. This is particularly common in high porosity images; hence it was called the sub-network of the over-segmented watershed (SNOW). The steps to achieve this improvement are: The algorithms start by applying Euclidean Distance Transform of the segmented pore space, then filtering the distance transform with a Gaussian blur to reduce the number of bad peaks, removing peaks that actually fell on plateaus and saddles in the distance transform, removing peaks that were too near to another peak, and finally applying marker-based Watershed segmentation algorithm which finds local valleys in the inverted distance transform so that peaks become valleys. The workflow for the SNOW pore network extraction methodology is shown in Figure 14 below:

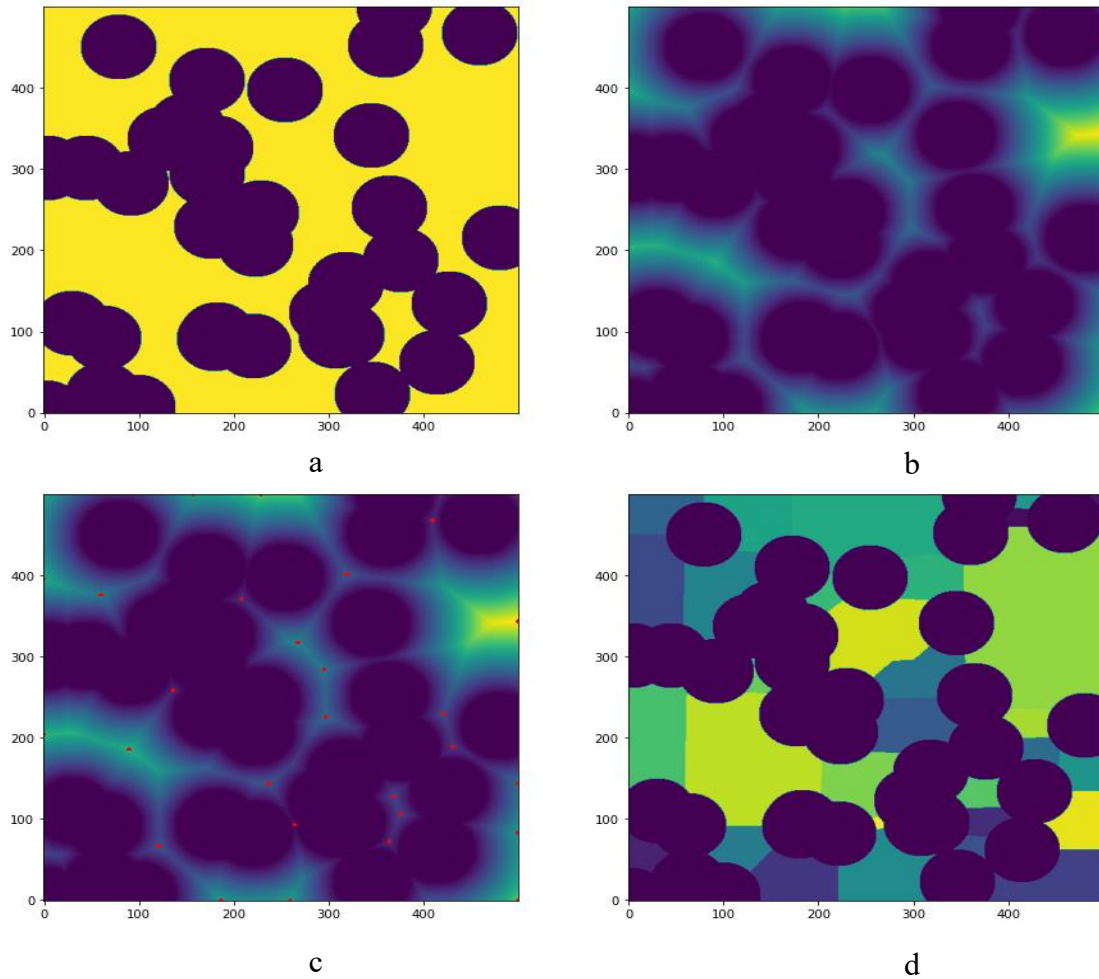


Figure 14: Basic steps of SNOW algorithm, a) a binary image, b) applying Euclidean Distance transform on the binary image, c) finding peaks using gaussian filter and trimming spurious peaks, d) finally applying marker-based watershed segmentation.

The main improvement required in the current pore network extraction methods is the accurate representation of multiscale rock. This means by capturing the true amount and location of microporosity including the presence of small-scale heterogeneity such as microfractures can greatly improve the reliability of pore network models. Thus, in our multiscale pore network

extraction approach, we aim to capture the correct amount and location of microporosity in a single step and then by assigning average effective properties and relevant pore scale physics to simulate the transport behavior of real rocks. We propose that by assigning realistic geometrical properties and having matched porosity, permeability and, formation factor with real sample, we hope will lead to good estimate of transport properties for multiphase flow conditions.

3.2 Multiscale pore network modeling

When the pore structure is accurately characterized by reasonably specifying size, shape, connectivity, and spatial arrangement of pores and throats, pore network models have the potential to become a predictive technique. In recent years, significant advances have been made in predictive pore-network modeling, where geologically realistic networks are constructed from 3D voxel-based images that may be generated by X-ray microtomography, confocal microscopy, or by 3D reconstruction informed by 2D images. Multiscale pore networks have the potential to model complex hierarchical porous media and systems with significant microporosity like carbonates. Multiscale networks recently developed represents a significant advancement over earlier research that concentrated on more homogeneous porous media like sandstones and sandpacks. Carbonates have a bimodal pore size distribution, and a far more complex wettability state [37] than sandstones. Carbonate rocks commonly display non-Archie behavior which has been attributed to porosity at different length scales, as evidenced by the anomalously low resistivity at lower water saturations. The main reason for this behavior in carbonates is the existence of connected intra-granular microporosity in the grain regions of nearly all carbonate rocks as explained previously in section 2.1.2.

Since the traditional relationships used in petroleum industry such as Archie's equation relating resistivity to saturation, Brooks-Corey for relative permeability and Carman-Kozeny for absolute permeability are not appropriate for carbonates and tight sandstones with mud, it

becomes imperative to investigate at the pore scale to gain a fundamental understanding of flow through porous media for finding closure relationships. Attempts previously made can be broadly classified into four different dual PNM approaches, since they consider both macro and micropores in these models, these dual PNM models can be classified as Coincident micropores, Parallel micropores, Explicit micropores and Averaged micropores according to the modeling of micropores in their approach as will be explained in detail in the following paragraphs. These four different approaches are shown in Figure 15 below:

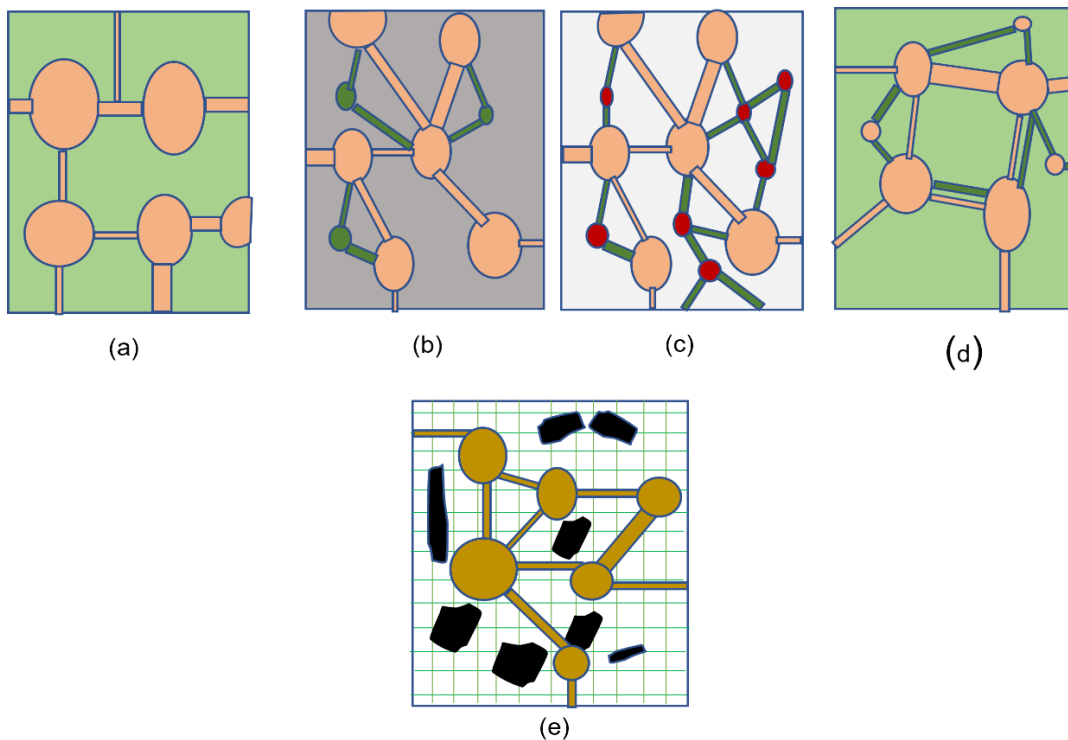


Figure 15:Representation of the dual PNM models, the Coincident micropore model (a) proposed by Berki [38], a cubic-lattice based network of macropores is embedded in a homogeneous microporous matrix of uniform properties, (b) The Parallel micropores model proposed by Baur [39] is image based and microporosity is added in parallel to the user defined percentage of macrothroats, (c) The Explicit micropores model used by Jiang [40] and Masa [41], the unresolved microporosity is modeled on high resolution micro-tomograph images where each individual micropore is taken into account. While in the

Averaged micropores model used (d) by Bultreys [42] microporosity is modeled as truncated cone micro-link between macropores taken both in series and parallel communication to the macropores. In the proposed Hybrid micropores model (e) macroporosity is taken as the original shape and location by image analysis with its network of macropores and macrothroats, the microporosity is taken as a continuum placing a cubic grid while the communication between macropores and micropores is through a macropore surrounding rim of pores, while the solid phase (black) shown at its true location. In models (a), (b) and (d) shaded region represents the matrix.

The dual pore network models to greater or lesser extent approximate microporosity and its connectivity with macropores. In the proposed Hybrid Micropores model developed in this work which may be considered as a continuation and improvement in the above four approaches, we take into consideration the real location of both micropores and macropores, real size of macropores informed by micro-CT images and the actual area of contact between the macropore and micropores by introducing the ‘interconnects’. The previous four approaches are discussed below in more detail.

Berki et al. [38] built a dual pore-network model, herein referred to as the Coincident Micropore model, where the microporosity and macroporosity systems are considered to co-exist in the same pore-throat-pore connections. This combined transport properties of the microporosity (capillary pressure, and relative permeabilities of the matrix which was considered homogeneous) with the pore network modeling approach used to simulate the secondary porosity (vugs or fractures). The model was based on generating an artificial cubic network of macropores while assigning average matrix (micropores) properties. Pore and throat dimensions of the macropore network in the model were adjusted to match the experimental values. Their method is unrealistic since the macropores must be fully connected for any path to exist through the domain. In a real sandstone the large-scale macropores do not necessarily form a connected network through the domain. The ability to bridge two disconnected macropores via microporous regions is crucial to properly describing the interaction between scales. Another attempt for modeling both the series and parallel flow was made Hakimaov et al. [43] they

prepared a 2D rectangular network model to represent the macro-network and then modified it to include microporosity by inserting the micro-network into macrothroats. They concluded that the existence of connected pathways through micro-pores that are fully saturated with a conductive phase creates ‘shortcuts’ for electrical currents which causes short circuit and, ultimately, lowers rock resistivity measured from log analysis. Neglecting microporosity thus causes erroneous prediction of flow and electrical properties, e.g., relative permeability, capillary pressure, and formation factor. Assumption of high mobile water saturation leads to underestimation of hydrocarbon reserves. However, they concluded that further work needs to be done to estimate Archie parameters such as saturation exponent and cementation factor [43].

A significant improvement on the Coincident Micropore PNM is the approach of Bauer et al. [39] called the Parallel Micropore approach. They extracted image-based network from three-phase segmented image of micropores, macropores and solids, the microporosity from micro-CT images of carbonate samples and added microporosity in parallel to a user-defined percentage of macro-throats, Figure 15. Although their method is largely image-based taking in account the real architecture of the macropore network, microporosity was considered to act only in parallel located along the macrothroats, thus present the same problem as the Coincident Micropore method. They suggested improvements of their method by including the real locations of micropores as deduced from micro-CT images so that both series and parallel arrangement of microporosity are taken into consideration generating a model of larger size and assigning better pore and throat conductance.

In the Explicit micropores approach Jiang et al.[40] proposed a workflow to join PNM extracted from images at different resolutions. A PNM of arbitrary volume representing the microporosity is statistically generated based on small network extracted from high-resolution imaging or modeled data. A network of macropores is subsequently fused with the microporosity by making a cross-scale connection between the networks. Although this is probably the most

rigorous and theoretically satisfying approach, the disadvantage being that the number of network elements can quickly become computationally prohibitive because each individual micro-pore is considered separately. Moreover, they have uniformly distributed fine-scale nodes in the model space without considering any spatial correlation. However, in complicated materials like carbonate rocks, correlations between micro-porosity and macro-porosity plays an important role in determining the transport properties and should be considered. Following the similar concepts, Prodanovic et al. [41] prepared an image based multiscale model in which they developed a two-scale algorithm and explicitly inserted rescaled micro-network into image analysis informed micropores regions. Since their model applies a re-scaled sandstone network to carbonate microporous region this technique could become computationally expensive in case of samples having large micropore percentages. Also, their assumption of using same physics for both length scales may give erroneous results.

Another attempt which can be placed in the category of the Explicit micropores approach attempted by Mehmani et al. [44] is process-based method using Delaunay tessellation of grain centers, then introduced a method to integrate microporosity explicitly with interparticle macroporosity [44]. Although, their method was useful for the investigation of the influence of microporosity on the transport properties when acting in series (intergranular or pore filling) or in parallel (grain filling, intragranular or dissolution microporosity) to the macropores, does not produce representative geometrical shapes of pores. Also, their method of adding rescaled microporosity may become computationally intensive.

Arash et al.[45] presented a Triple Pore Network model, of macropores, micropores inside solids and synthetically generated fractures composed into a single coupled pore network. They used two stage watershed segmentation to extract data from images of porous material and build a triple network by first building a dual PNM of macropores and fractures and then adding a PNM of micropores inside partially solid grains to the dual network to make a Triple network

composed of macro-pores, micro-pores, and fractures. They concluded that for gas flow in tight formations, a triple pore network model (T-PNM) better represents gas permeabilities than the dual models. In their model, microporosity is considered to consist of a bundle of microtubes of different radii, transport calculations by this approach could be complex for large size samples.

In the Averaged micropore approach Bultreys et al. [8] prepared an image based multiscale network model and used micro-CT images of tight and heterogenous carbonate rocks to extract a dual pore network that in addition to macropores also included microporosity which was treated as a continuous porous medium. In their method, starting from three phase segmented image, the macropore network was extracted using the maximal ball algorithm, while the microporosity was modeled through a truncated cone micro-link between macropores treating the microporosity as a continuous porous medium. This averaging of microporous region properties introduced the need of cut-off length to the micro-links. The truncated cone shape model was used to connect two neighbouring macro-pores, thus tortuosity of the connection and geometric details about the bulk of the micro-porous cluster such as exact location of microporosity and actual connectivity are neglected, which can lead to erroneous local conductivities [46]. Their method, therefore, needs improvement in terms of more realistic averaging of micropore properties, including tortuosities and connectivity with macropores.

In our approach, called ‘hybrid micropores’, which can be considered as an improvement to the Averaged micropores approach, is illustrated in Figure 15(e). We first aim to capture the correct amount and location of microporosity in a single step and then by assigning average effective properties and the relevant pore scale physics simulate the behavior of real rocks, the details of the model development will be explained in detail in the next chapter. Also, the proposed method when implemented on real images will enable to vary the phase properties and help analyze the impact on resulting transport properties. We propose that by assigning realistic geometrical properties to the macropore network and realistic average statistical properties to

the micropore regions and then matching porosity, permeability, formation factor and capillary pressure will lead to a good model of real rocks which can be used to estimate transport properties for multiphase flow conditions.

4 Multiscale Pore Network Modeling

This chapter explains the methodology used in developing a multiscale pore network extraction method and applies it to some images for demonstration and validation. Since multiscale images of real porous media cannot currently be obtained from tomography equipment, so multiscale images have been artificially created that span several length scales for demonstration purpose. Section 4.1 details how on the artificial images generated, the pore network is extracted on these artificial images in a single step, the micropore regions are modeled as continua with effective properties, obtained from correlations for related materials, but could in principle be obtained from network extraction of nanoscale tomographic images. The macropore networks is then stitched together with the continua scale, thus creating a hybrid hierarchical pore network, the developed modeling framework is used to evaluate formation properties such as porosity, permeability, and formation factor. Materials and images used for validation is discussed in section 4.2. Results and discussion on the example applications of the developed model on 3D and 3-phase real images are shown in section 4.3.

4.1 Hybrid-hierarchical Pore Network Modeling

The objective of this section is developing the method of obtaining a pore network model of the hierarchical reservoir rock by extracting pore networks from images that only possess information at a single length scale explained. To achieve this goal, it was expedient to generate representative artificial images of carbonate rocks and tight sandstones with mud and perform quantitative analysis. In this work the simple 2-D and 3-D images have been created for demonstration purpose, examples of artificial images and network extraction are shown in this chapter and in Appendix B. Examples of artificial images can also be found in Mousavi et al. [18]. It should be noted that these artificial images were generated during the start of the project to develop the workflow and in lieu of real images, these images are not rigorously generated.

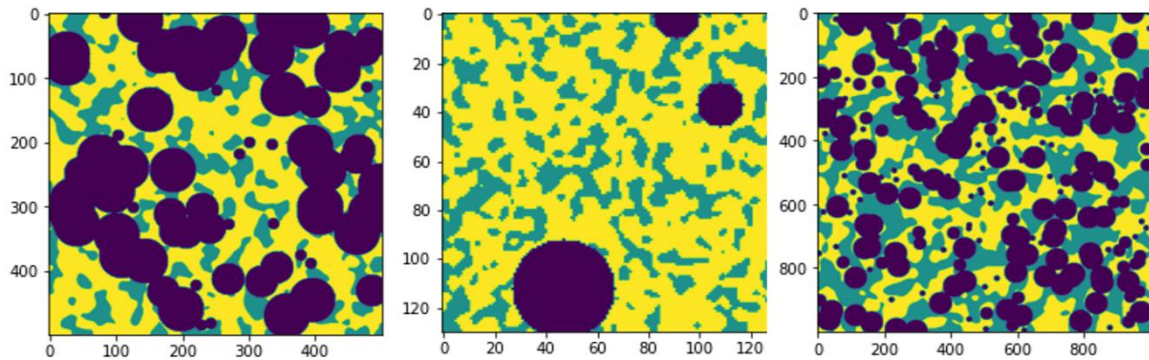


Figure 16: Examples of three artificial images of different sizes.

The main innovation of the present work is to model the matrix region as an effective continuum using basic finite difference calculations on a grid, while this grid is connected to the macro-pore network. In this way the transport through the domain can be simulated as a combined effect of both the network and the continuum. Crucially, by connecting microporosity with macroporosity the two regions can communicate and exchange mass thus allowing the concentration/pressure field to be computed, so as flow travels through the macro-pore network as the pressure field is applied to the micropores via the new interconnections termed as ‘interconnects’. The result of this extraction is shown briefly in Figure 17 for the same three 2D artificial images presented in Figure 16. This model makes it possible to further evaluate the resulting impact of type and size and spatial arrangement of microporosity on total permeability, formation factor, resistivity index, mercury injection capillary pressure curve, porosity and ultimately water and oil saturations of the rock sample.

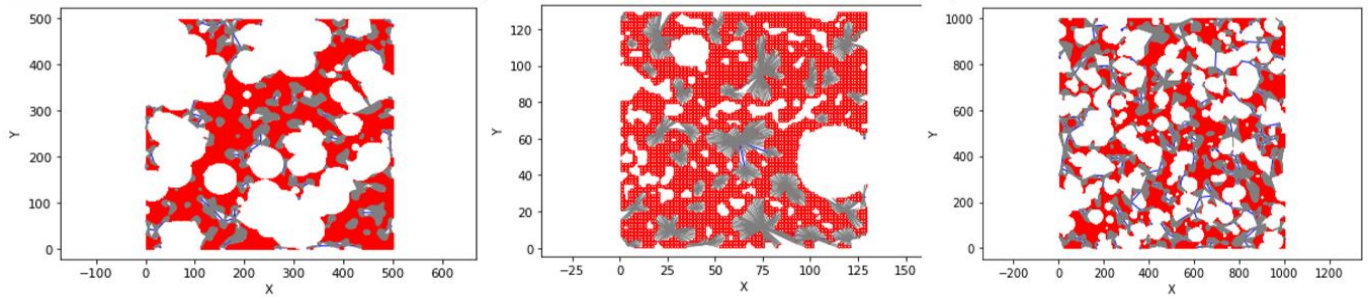


Figure 17: The network extraction of images shown in figure 16.

By correctly mapping the distribution of microporosity across oil and gas reservoirs and its connectivity with macropores and vugs, a better characterization of the reservoirs is obtained. This in turn helps in improving the static and dynamic models of the reservoirs for field development planning in terms of production potential, and realistic hydrocarbon reserves estimates. The correct mapping of microporosity and its relationship with macroporosity also helps in refined water saturation calculation and consequently enable the identification of bypassed oil pockets in the reservoirs. In our multiscale network extraction model, we are extracting a macropore network by using SNOW network extraction, then assigning a cubic grid network with average properties on the micropores matrix region identified from 3-phase segmented image rendered into solid, macropores and matrix regions. Then multiscale network is generated by merging and stitching these two networks by using ‘interconnects’ i.e., the links between macro and micropores, while these interconnects have high conductance values.

The details of current network extraction method are explained in section 4.1.1. We are extracting micropores, but we abstract the microporosity as a cubic grid i.e., continuum scale microporosity with constant properties throughout. This assumption is well justified. Stanely et al. [19] reported that there was a trend of increasing unimodal distributions as the fraction of

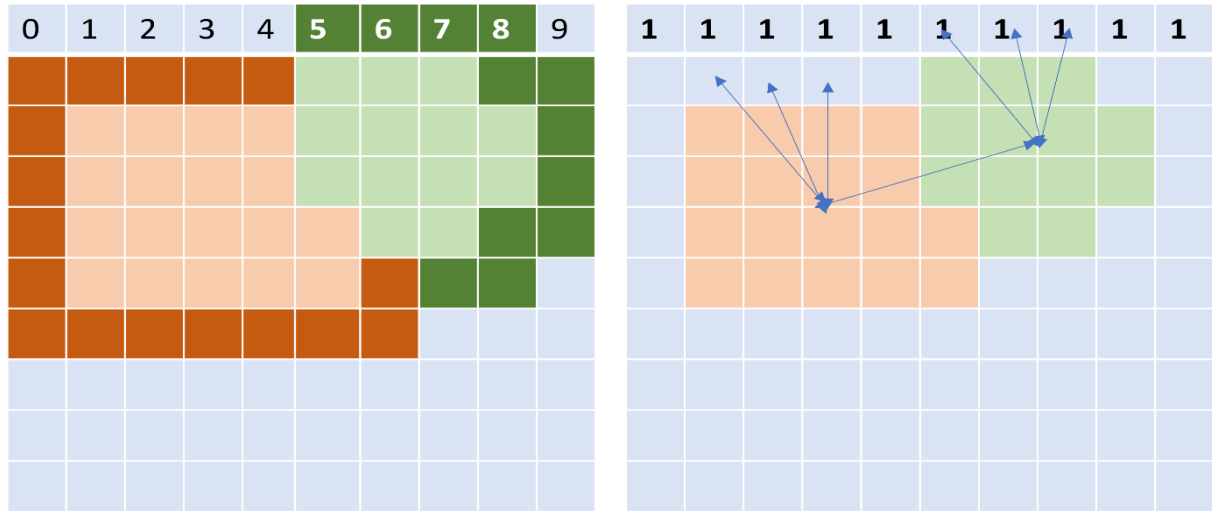
microporous matrix increases in carbonates. Fullmer et al. [13] reported highly homogeneous pore systems in micro-pore dominated rocks.

4.1.1 Multiscale network extraction process

Consider the schematic diagram shown in Figure 18 illustrating the hybrid network extraction method developed herein. The regions denoted by orange and green voxels represent the void pores, while the grey voxels represent microporosity. The hybrid network extraction works in three steps. Firstly, the pore network for the voids is found using the standard SNOW technique to determine which voxels in the image are associated with each pore (this is indicated by the orange and green colors). Second, a cubic lattice network is created using the micropore voxels as a template. Lastly, using basic image processing techniques such as dilation and maximum filters, micropore voxels around the rim of each void are identified and associated with their associated void, as indicated by darker shades. These voxels are then connected to the void network by making manual entries in the network adjacency matrix.

The details of the implementation are given in a more realistic example applied to the 3-phase image shown in Figure 19, containing 3 voids and a small solid grain. Each of the above steps are illustrated sequentially in Figure 20, with the top row showing the image processing and the bottom row showing the corresponding network connections. To start the voids are identified using the watershed-based network extraction algorithm the steps of SNOW algorithm as explained previously in section 3.1. In step 1 pore network for voids is found, step 2 shows that cubic lattice is created in the microporous regions, and step 3 where basic image processing techniques are used to connect each micropore voxel in the rim of each void with their associated macropore void. As indicated by the darker shades. The last step shows when these rim voxels are manually connected with void and to micropores thus resulting in a merged network.

Conceptual Diagram



(a)

(b)

Figure 18: The concept of rim is shown above. In fig (a) the two pores with their surrounding rims as identified in step 2 of the procedure are shown. In fig (b) cubic lattice is inserted in surrounding matrix having all 1s as explained in step 7 and do the network extraction in the macropores regions having all 0s using OpenPNM network extraction algorithm.

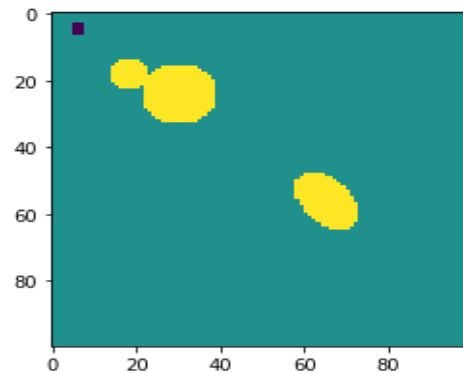


Figure 19: A three phase simple image with matrix in green, two connected macropores and one non-touching vug in yellow and a grain embedded in matrix is shown in black (top left).

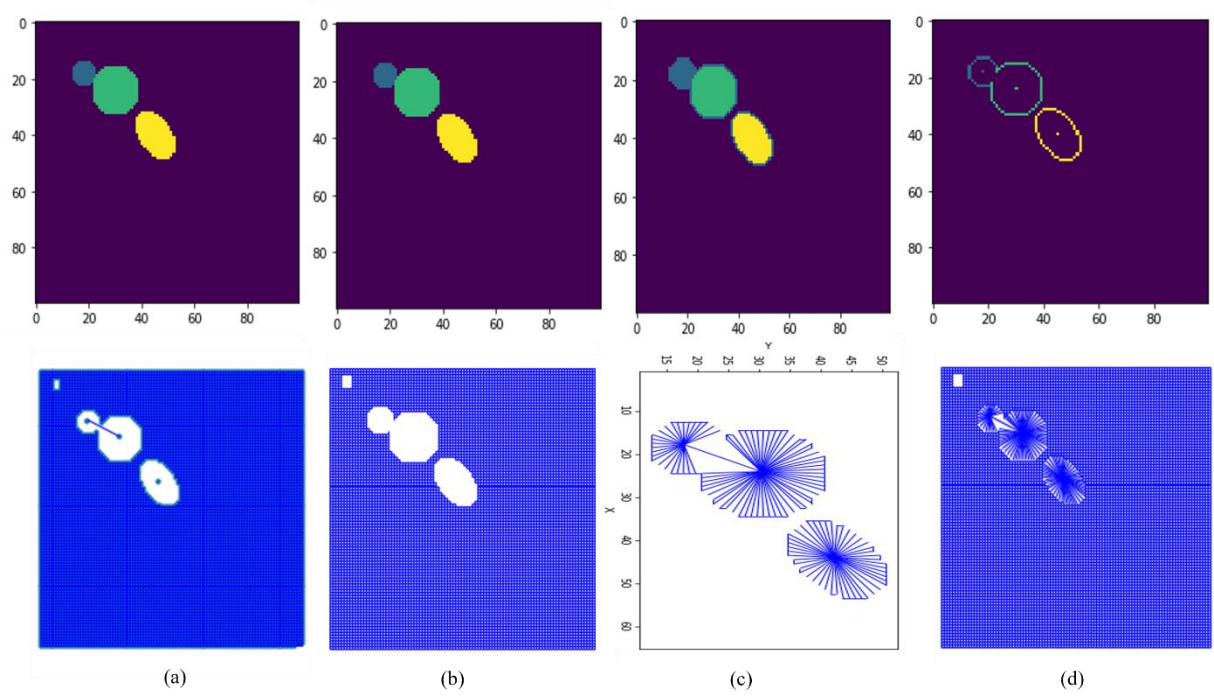


Figure 20: From left to right, a) first column show step 1 as pore network for voids is found, b) step 2 in second column shows cubic lattice is created in micropores, c) third column shows step 3 where, using basic image processing techniques micropore voxels rim of each void are identified with their associated void, as indicated by darker shades. (zoomed in view with connections are shown in second row) d) The fourth column shows the last step when these voxels are connected with void and micropores.

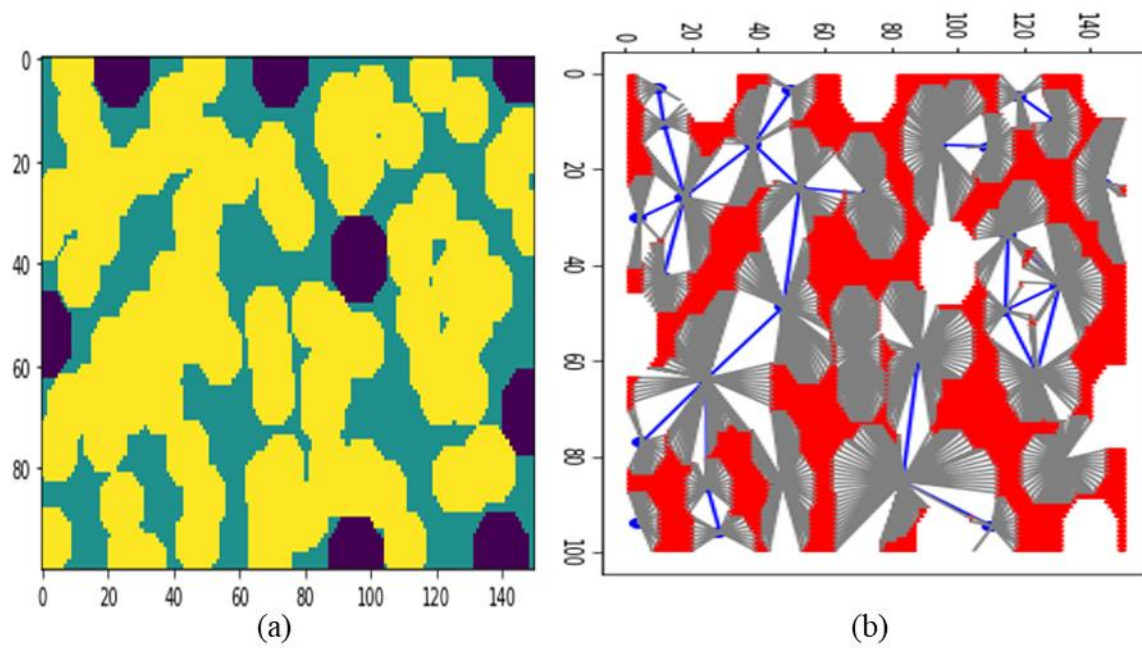
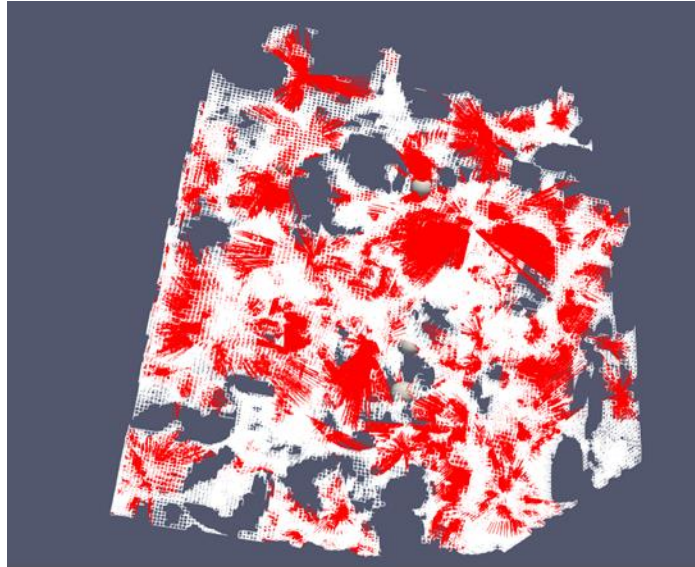
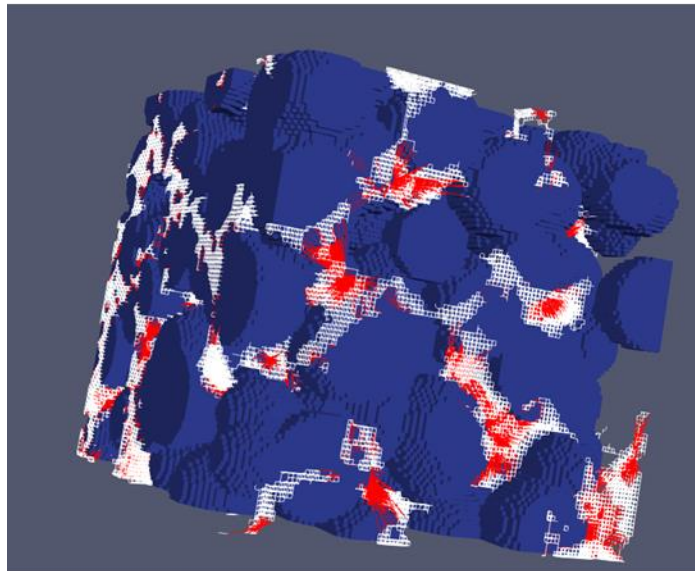


Figure 21: Example 2D and 3-phase image on a) left with green as matrix region, yellow as macropores and black are solid grains, and b) its network extraction is shown on the right. The value of absolute permeability determined was 0.775.



(a)



(b)

Figure 22: (a) Network extraction of a 3D and 3-phase artificial image. Macropores, interconnects (red color) and matrix (white), (b) below the same network with overlaid image showing solid grains.

4.1.2 Permeability estimation in hybrid hierarchical networks

In this and the next section estimation of transport properties is explained on the developed modeling framework and is used to evaluate formation properties such as porosity, permeability, and formation factor. The porosity calculation method has been previously explained in section 2.1.1.

Since the transport properties of regions of microporosity cannot be obtained from the image, instead we use the continuum approach for these regions. In the continuum approach we ignore the actual details of the pore structure and abstract the media as continuum with effective properties. As we do not know the size or number of tubes through which fluid is flowing, we lump all unknown values into a single constant K_{ck} as given in Carman-Kozeny (CK) equation (24) which relates permeability to porosity and grain size with some measure of tortuosity, in this case k_{CK} :

$$K_{ck} = \frac{d_{grain}^2 \phi^3}{16k_{ck}(1 - \phi)^2} \quad (24)$$

where, ϕ is the porosity in the microporous region, d_{grain} , is the characteristic particle size of microporous matrix, and k_{ck} is a fitting factor that encompasses all other aspects of the microporous material i.e., structural affects such as particle shape. In carbonates, unresolved pores that contribute to flow are typically of sizes between 0.1 to 5 microns [16]. For example, in our case we have taken the parameter to be 4 microns. However, for the actual porous media we need to enter the correct estimate of microporous region porosity and grain size. Grain sizes commonly used for sandstones are shown in Table 1 below:

Table 1: Grain sizes for sands [47].

Material	Grade	Sizes
Gravel	Coarse	20-60 mm
	Medium	6-20 mm
	Fine	2-6 mm
Sand	Very Coarse	1-2 mm
	Coarse	0.5-1 mm
	Medium	0.25-0.5 mm
	Fine	0.1-0.25 mm
	Very Fine	0.05-0.1 mm
Silt	Coarse	0.02-0.06 mm
	Medium	0.06-0.02 mm
	Fine	0.02-0.006 mm
Clay		<0.002 mm

Having determined permeability coefficient K_{ck} for the matrix regions from equation (24), we can estimate the hydraulic conductance for each matrix node in the microporous region using Darcy's law:

$$Q = \frac{K_{CK} A_{vx}}{L_{vx} \mu} \Delta P \quad (25)$$

from which we can identify the hydraulic conductance as:

$$g_{h,matrix} = \frac{K_{ck} A_{vx}}{L_{vx} \mu} \quad (26)$$

where A_{vx} is the cross-sectional area of the voxel element, L_{vx} is the length of the voxel along the direction of flow, and μ the fluid viscosity.

The macropores in the hybrid network are connected both with other macropores via macrothroats network and with the surrounding micropores via the interconnecting throats, this results in an enhanced connectivity for the sample. However, the hydraulic conductance for these interconnects needs to be estimated. As a first approximation we are assigning minimum resistance, thus maximum conductance to these interconnects so that mass transfer between macropores and surrounding micropores easily occurs without any resistance.

A novel feature of the proposed algorithm is that we can accurately identify the exact number of micropores/microthroats surrounding each macropore. The total number of interconnects are basically the total number of micropores/microthroats which surrounds or are in direct communication with the macropores and links microthroats with the macrothroats and thus enhance the connectivity of the total network as illustrated in Figure 23 below.

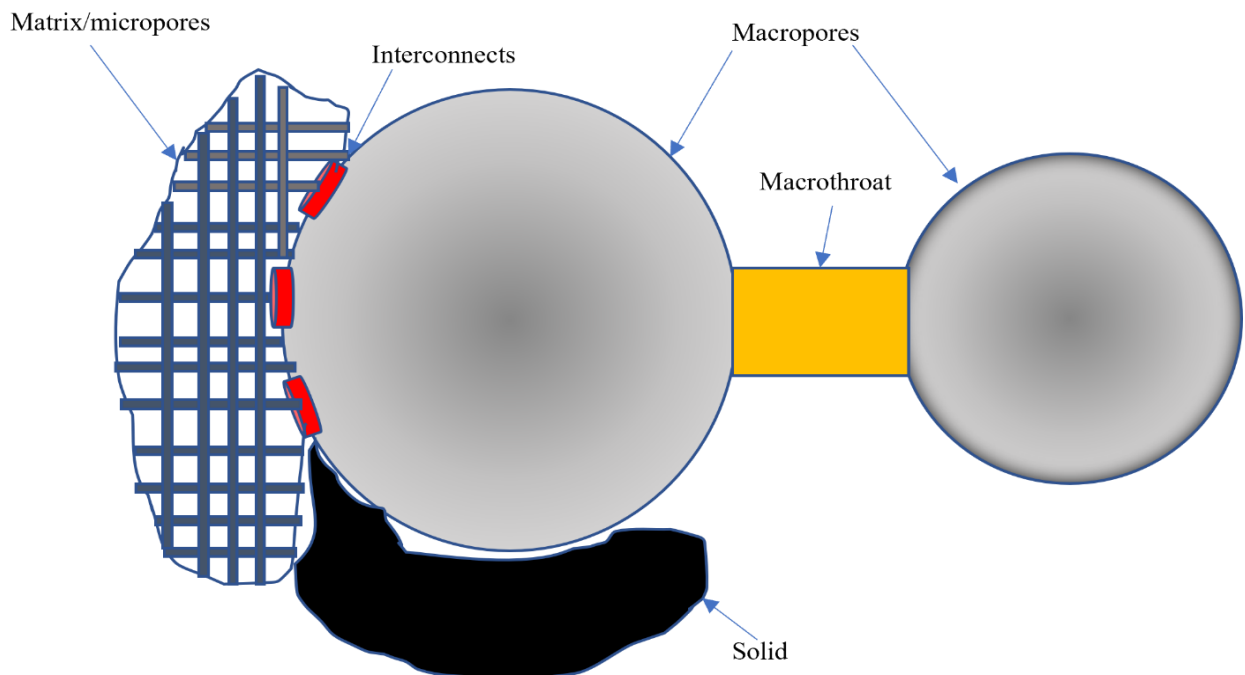


Figure 23: A schematic illustration of the geometrical elements in the proposed hybrid model.

Since we have identified the total number of pores/throats surrounding the macropores, these ‘interconnects’ having been assigned minimum resistance to flow and conductance as explained in previously. As geometry plays the key role in conductance calculations, we propose a shape which gives high conductance to the ‘interconnects’, however this will be investigated in future studies. This assumption is justified on the basis that the hydraulic or diffusive conductance should be transferred from macropore to the immediate neighbouring micropores without any resistance.

As explained in this section above, in our hybrid multi-physics model calculating overall hydraulic conductance has been implemented by using Darcy’s equation in microporous regions and the Stokes equation in the remaining macropore region.

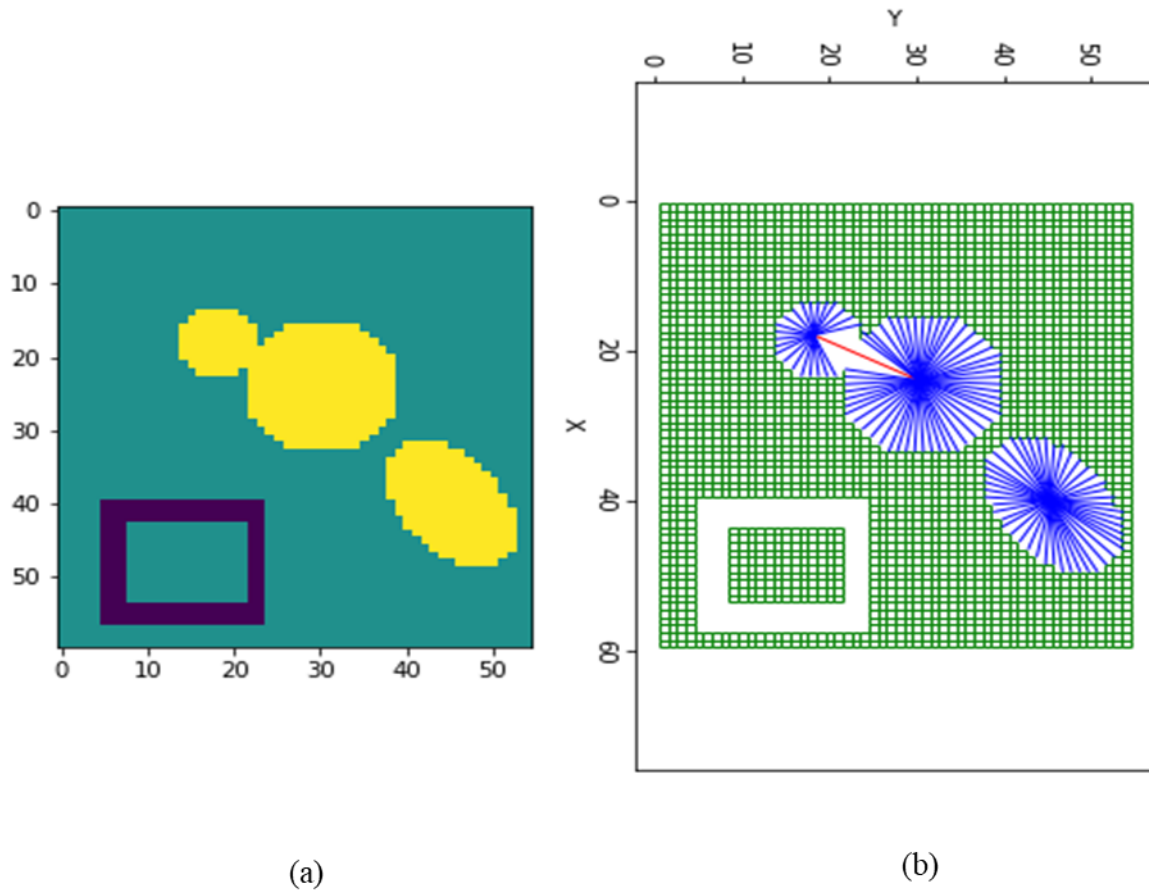


Figure 24: The figure (a) above shows that the isolated matrix region surrounded by solid (bottom left corner) in a rectangle shape is not connected to the combined network, whereas in (b) vug (bottom right corner) is connected to the surrounding matrix via interconnects shown in blue color.

Having applied conductance for each throat, by using appropriate models for micropores, macropores and new throats conductance, we finally apply the necessary boundary conditions and using the StokesFlow algorithm in OpenPNM to handle the process of building the coefficient matrix and solving for pressures in each pore. Knowing the pressure in each pore and the conductance in each throat it is possible to find the volumetric flow rate entering or exiting

each boundary pore. The sum of these gives Q , which allow for the determination of the network permeability coefficient by inverting Darcy's law:

$$K = \frac{\mu QL}{A(P_{in} - P_{out})} \quad (27)$$

where K is the absolute permeability of the hybrid network, P_{in} and P_{out} are arbitrary chosen inlet and outlet pressures, A is the cross-sectional area of the domain normal to the flow direction and L is the length of the domain in the flow direction.

4.1.3 Formation factor estimation in hybrid hierarchical networks

A good model to simulate petrophysical transport properties should not only produce the classically observed Archie's behavior, but also non-Archie curves [39]. The petroleum industry utilizes the measurement of electrical resistivity of partially saturated rocks to estimate the productivity and size of oil and gas reservoirs [9]. The formation factor (FF) measured at complete brine saturation of the rock sample defined the electrical transport properties of the porous medium. The value of m , the cementation exponent in FF equation (12) reflects the tortuosity of the current flow and is specific to the type of microporosity, in case applied to that region of the sample. Due to the analogy between Ohm's law for electrical charge transport and the Fick's law for the solute particles in diffusional transport, and considering electrical and diffusional tortuosities are the same [28], the formation factor is also given by the ratio of molecular diffusion coefficient in open space D_{AB} to the effective diffusion coefficient in the medium D_{eff} as will be explained.

The Resistivity index given by equation (14) in section 2.1.6 can be utilized to calculate the water saturation of a hydrocarbon bearing zone when an obvious water-bearing zone of the same porosity is available nearby and having water of the same salinity [48]. Empirical Archie's laws describe the resistivity behavior of clean sandstones as given in equation (13).

In the current model to calculate Formation Factor, as a first approximation, we are estimating tortuosity of the matrix region using Bruggemann correlation for spheres, equation (28). The effective diffusivity of the matrix region is calculated from equation (31) and assigning high diffusive conductance for the interconnects.

$$\tau = \phi^{-0.5} \quad (28)$$

$$\frac{D_{eff}}{D_{AB}} = \frac{\phi}{\tau} \quad (29)$$

$$D_{effVx} = \frac{D_{AB}\phi_{matrix}}{\tau} \quad (30)$$

$$g_{d_{matrix}} = \frac{D_{effVx} A_{Vx}}{L_{Vx}} \quad (31)$$

The diffusive flow rate N_A (moles/sec) with applied concentration difference at the inlet and outlet. Upon solving the system of coupled linear equations to find value of concentration in each pore by casting the equation in matrix form, once N_A is known, we calculate effective diffusivity of the whole domain by applying the Fick's law equation (33).

$$N_A = -D_{AB} \frac{\phi}{\tau} \frac{dC_A}{dx} \quad (32)$$

$$D_{eff} = \frac{N_A L}{A(C_{in} - C_{out})} \quad (33)$$

The formation factor is then obtained as the ratio of bulk diffusivity in open space, D_{AB} , to effective diffusivity of the medium, D_{eff} as follows:

$$FF = \frac{D_{AB}}{D_{eff}} \quad (34)$$

4.2 Materials and Images Used

Validation of the developed hybrid algorithm is done by comparing porosity, absolute permeability and formation factor values calculated from our hybrid algorithm with the experimental values obtained on realistic image of sandstones and carbonate rock samples from different formations. The algorithm for hybrid pore network extraction has been tested first on a total of nine 2D images, five sandstones and four carbonates Appendix C. For sandstones we selected Berea Sandstone and four samples of North Sea Sandstone all of which were three-phase segmented, for carbonates we have used Estailades carbonate, Austin Chalk and Savonnieres carbonate. Further detailed validation and analysis was done on the two 3D carbonate samples all downloaded from www.digitalrocksportal.org, namely Massangis Juane Limestone and Estailades carbonate [49]. Since for heterogeneous carbonate samples, having complex pore structures many pores could be disconnected in 2D models, we have used 3D models for validation, which should result in a better match with experimental values.

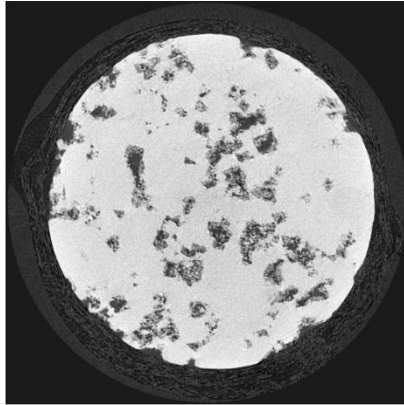
These 3D samples were first segmented into the three phases namely, void, matrix and solid using an in-house algorithm (described in Appendix D), then network extraction and calculation of transport properties was done using our hybrid algorithm. Since correct segmentation plays a crucial role in further analysis of the sample, a close matching of matrix fraction of pore space obtained from the segmented images with the values in reference Bultreys et al. [49] is an indication that our segmentation is reliable. For Estailades our segmentation showed matrix region as 46.77% contribution of porosity versus DPNM of 43.4%, while in case of Massangis our segmentation showed a value of 45.4 versus 38.9 from the reference case. It should be noted that the final network obtained by the hybrid algorithm contains information about the size, spatial location, and connectivity of macropores, as well as the size, spatial location of matrix region i.e., distribution of microporosity regions in the sample, containing unresolved

microporosity and the amount of connectivity of unresolved micropores in the matrix region with their neighboring macropores.

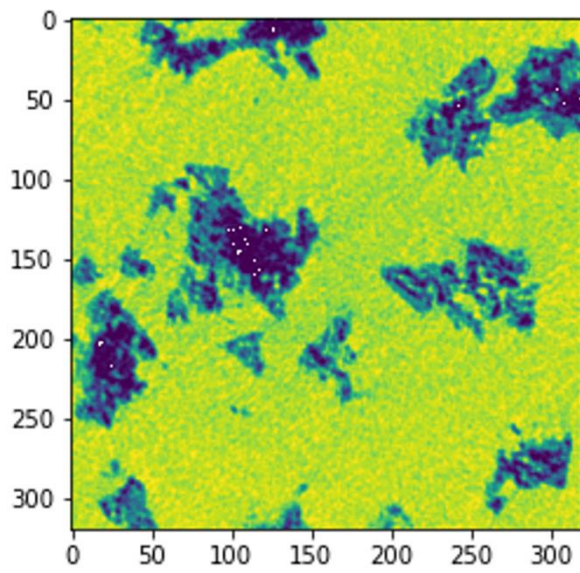
For most of the samples our new hybrid model estimates of permeability and formation factor are accurate within a factor of 2 with maximum variation not more than a factor of 10 as explained in detail in the discussion section. We consider this reasonably successful given the novelty of the approach, which can be further improved with future research. We have demonstrated that our new hybrid model has the flexibility to accurately identify the actual location of the matrix region, bypass isolated pores and matrix region, has the ability manipulate/assign porosity and pore sizes of microporosity within the matrix region to match the experimental values of the samples and to accurately connect microporosity in the matrix region with the macroporosity region.

4.3 Results and Discussion

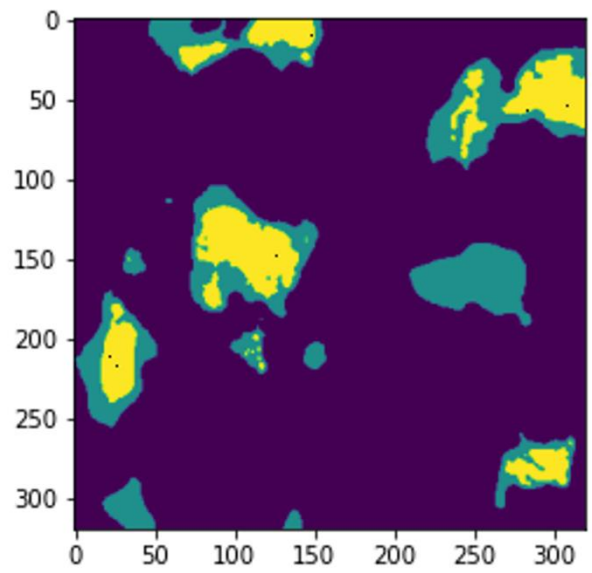
In this section the results of applying hybrid network extraction technique on 3D and 3-phase real carbonate samples of Massangis Jaune Limestone and Estailades carbonate are discussed in detail. These real rocks have been widely studied and used in digital rock analysis. Network summary statistics are also provided below and discussion on the results are given.



(a)

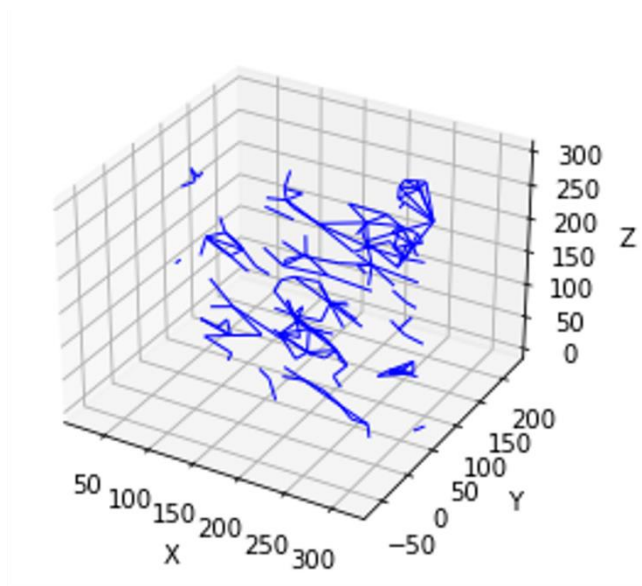


(b)

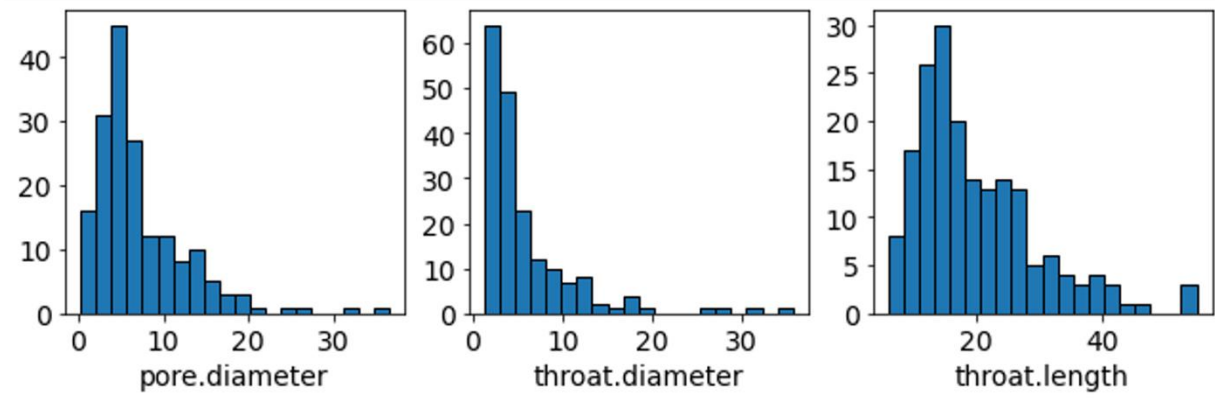


(c)

Figure 25: (a) Massangis Juane Limestone raw image and (b) a subsection of the greyscale raw image taken for 3 phase segmentation (c) Three phase segmentation.



(a)



(b)

Figure 26: a) Macropore network in 3D and, (b) histogram of network properties for Massangis Jaune Limestone.

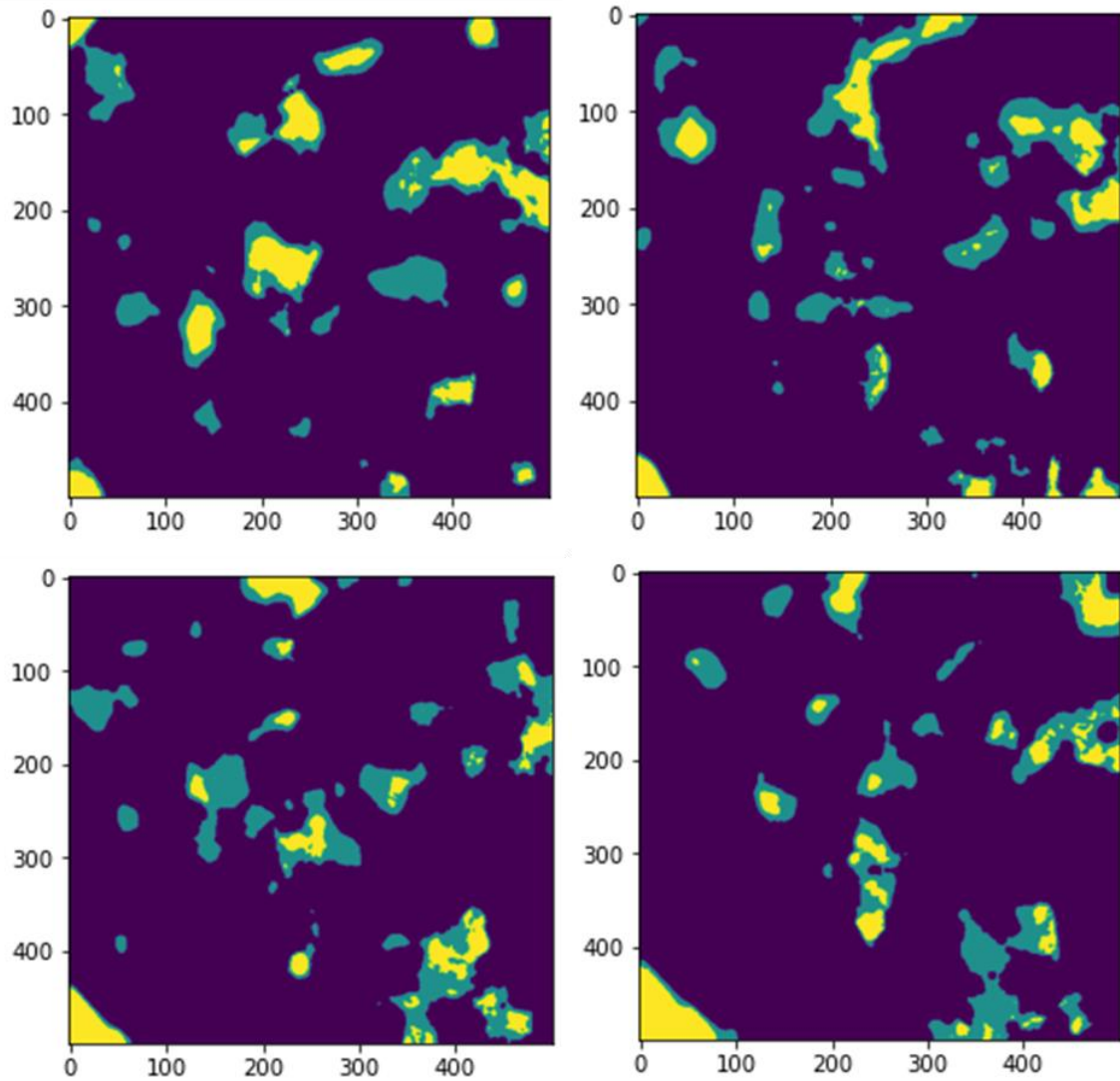


Figure 27: 2D slices through the three-phase segmentation of various z-direction slices of Massangis Jaune Limestone sample. The macroporosity fraction is approx. equal to microporosity. The microporosity type is both pore lining and pore filling resulting in microporosity having dominating control on transport properties.

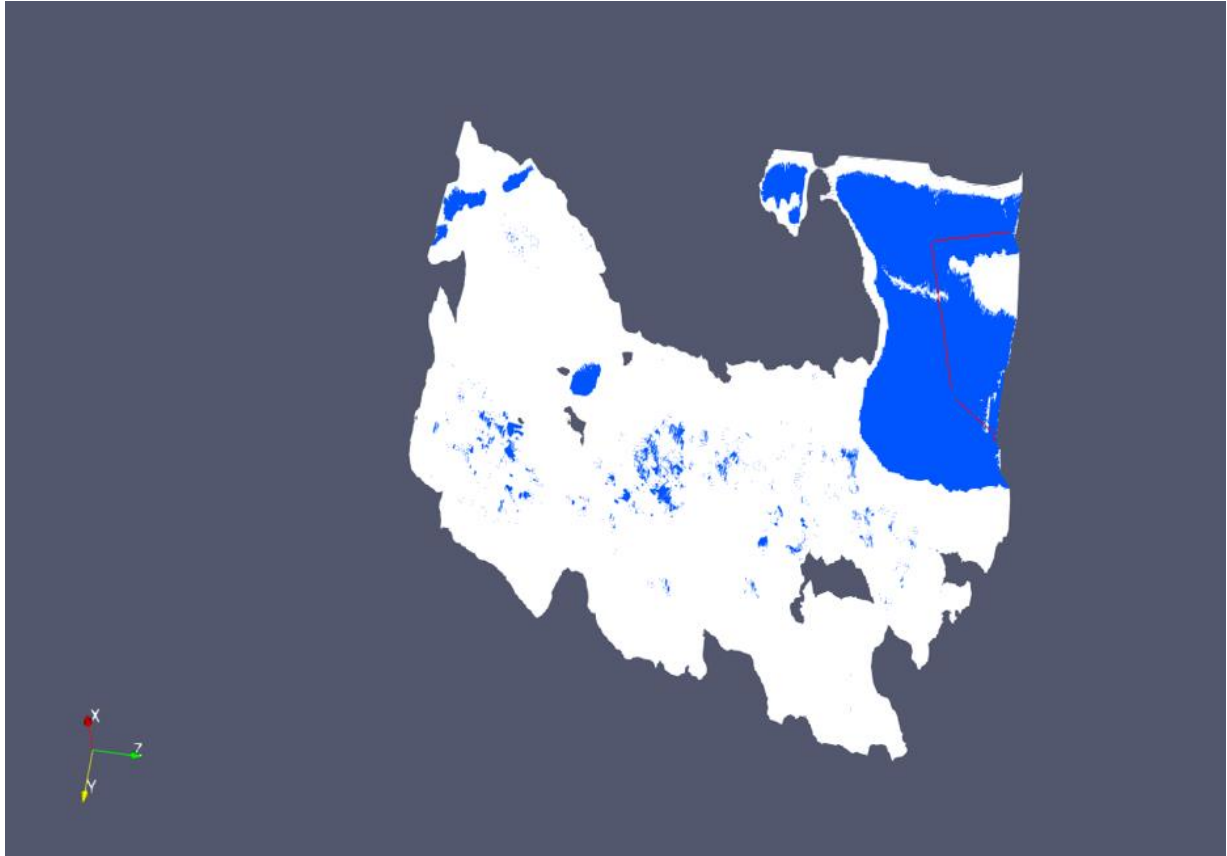
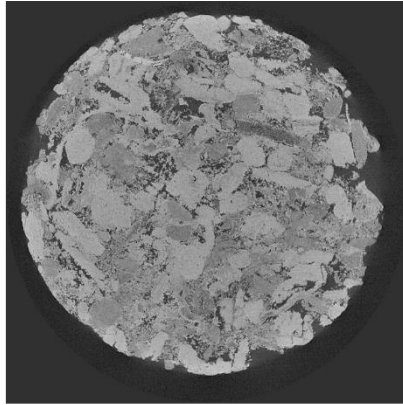
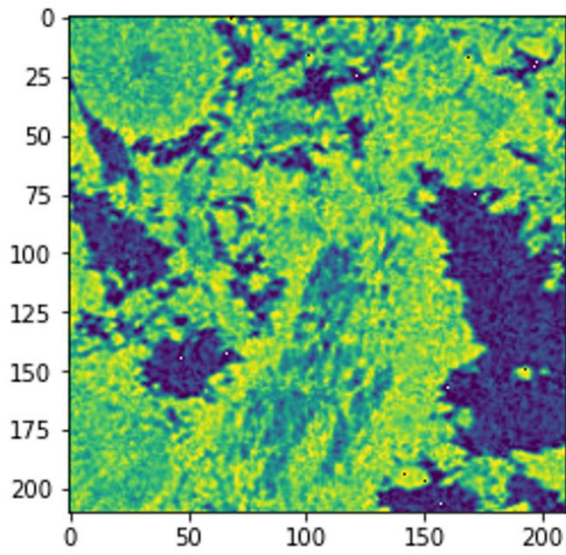


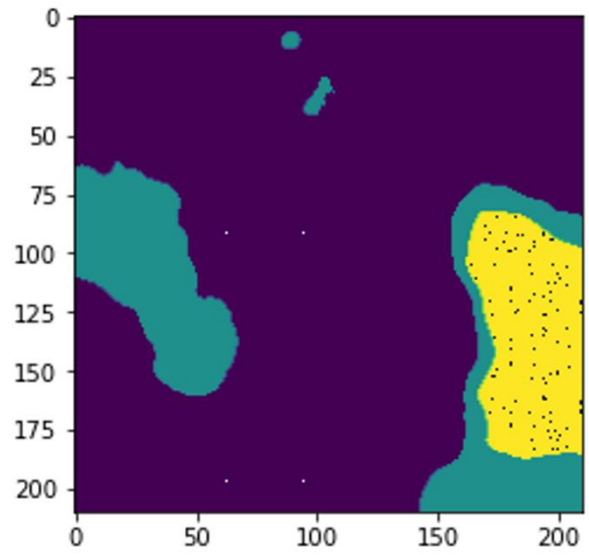
Figure 28: 3D network of Massangis Jaune Limestone shown in Paraview. Matrix is in white, macrothroats in red and interconnects are shown in blue color.



(a)

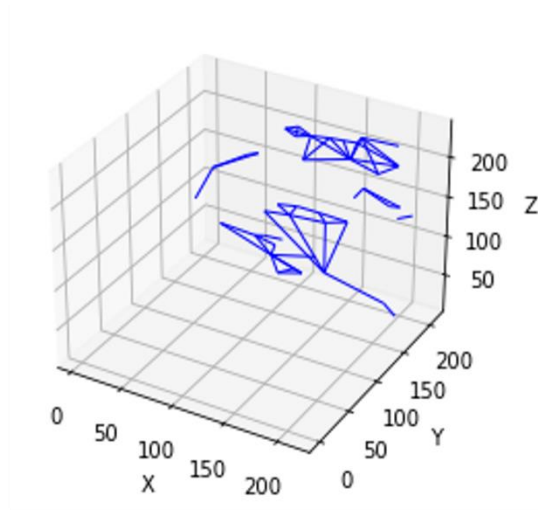


(b)

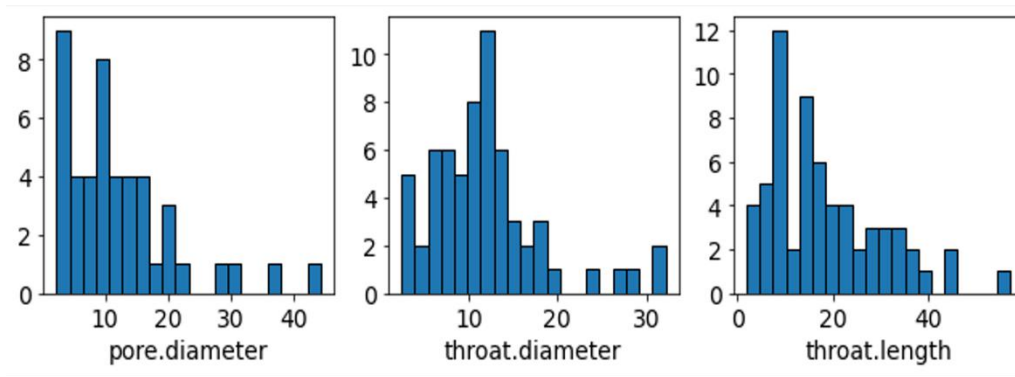


(c)

Figure 29: (a) Estallades raw image and (b) a greyscale subsection of the raw image taken for 3 phase segmentation (c) Three phase segmentation.



(a)



(b)

Figure 30: Estailades carbonate a) Macropore network and b) histogram of network properties.

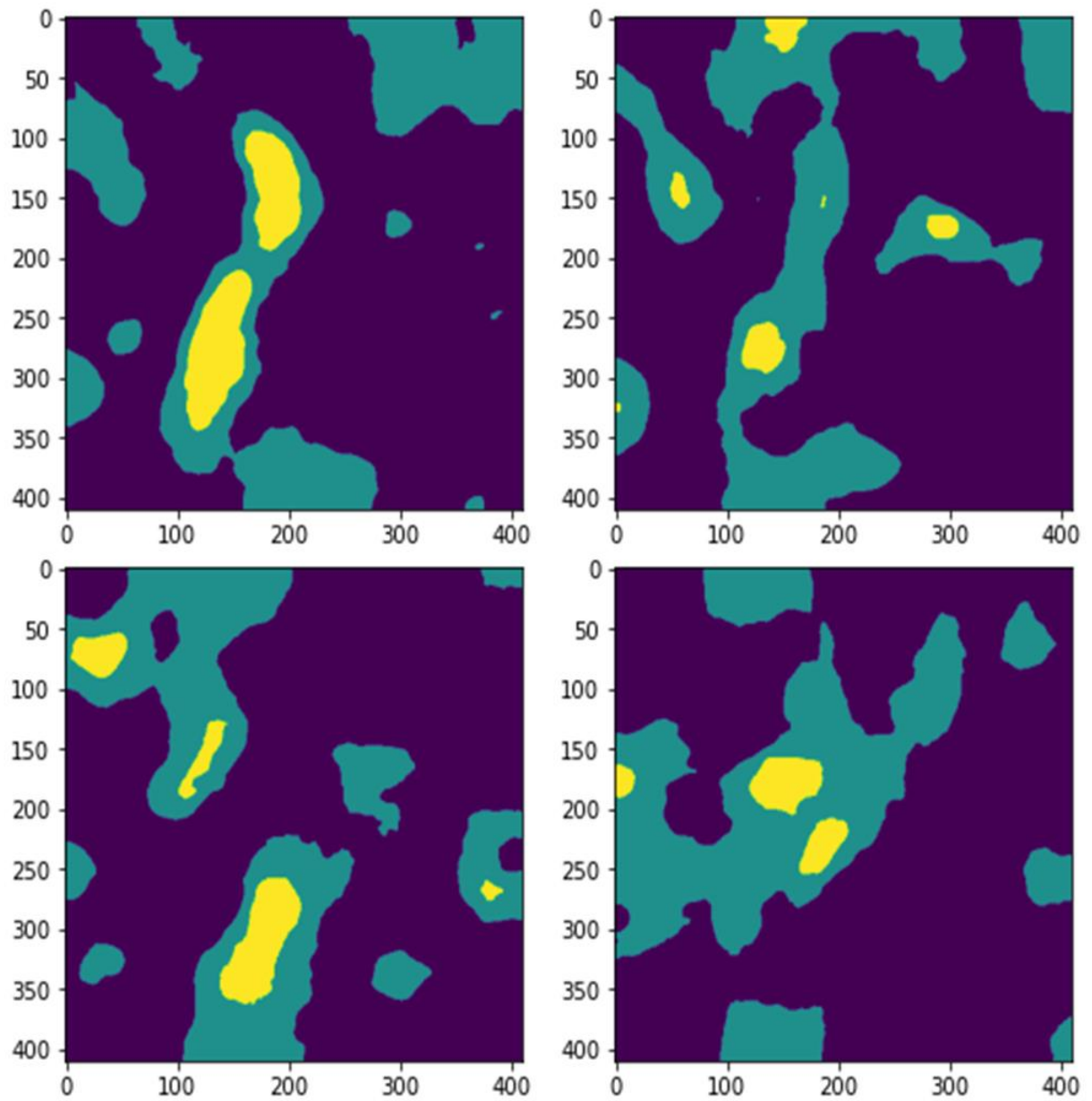


Figure 31: 2D representation of three-phase segmentation of various z-direction slices of Estailades carbonate sample. The microporosity fraction is greater than macroporosity. The microporosity and macroporosity arrangement results in parallel dominated flow with resulting higher permeability.

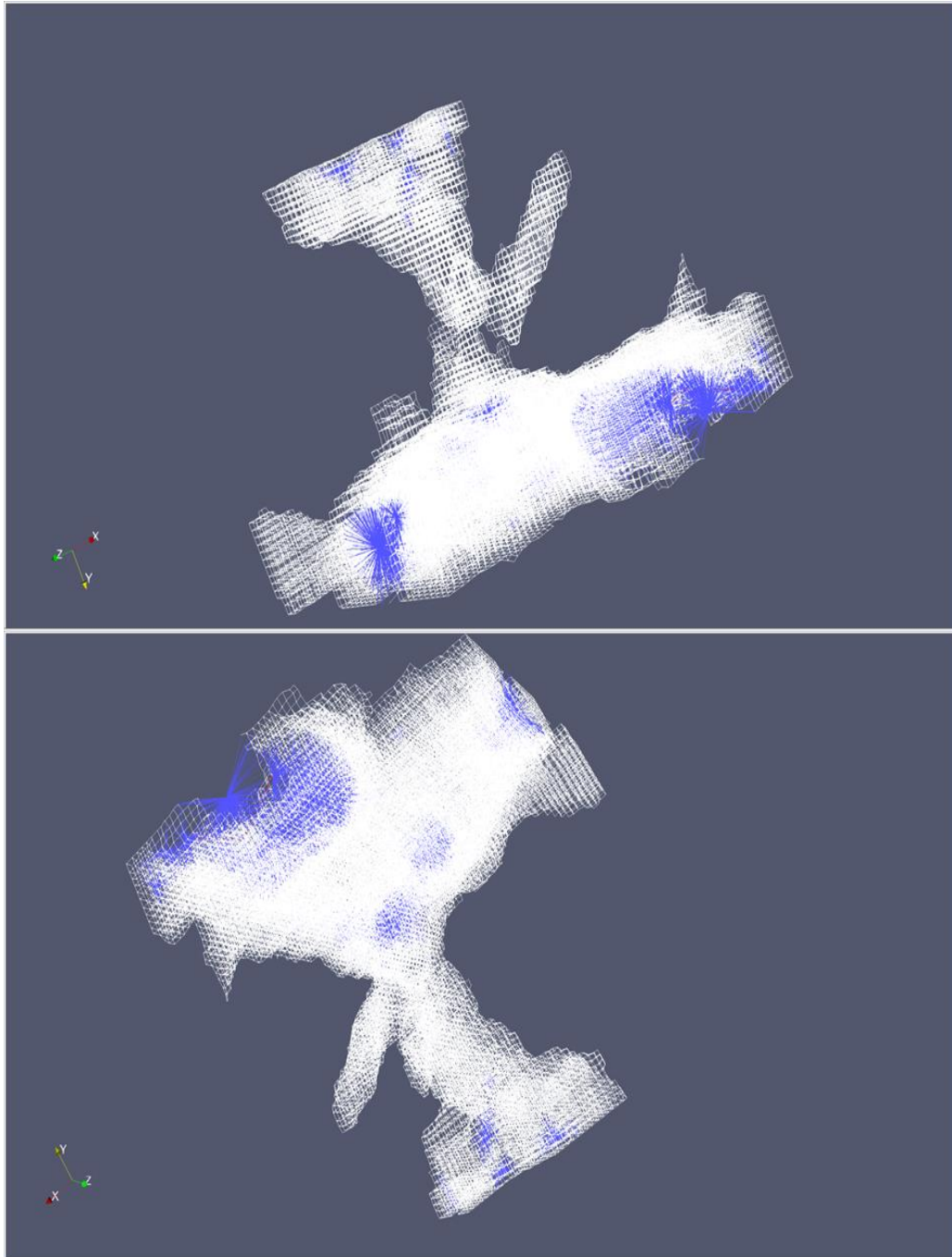


Figure 32: Two different view angles for 3D network of Estailades carbonate shown in Paraview. Matrix is in white, macrothroats in red and interconnects are shown in blue color.

Table 2: Network statistics for 3D and 3-phase carbonate rock samples.

	Massangis Jaune	Estailades
Sample size	320 X 320 X 300	210 X 210 X 240
Voxel dimension (m)	4.53e-6	3.1e-6
No. of macro-pores	177	46
No. of macro-throats	186	63
No. of micro-pores	1833311	1619963
No. of micro-throats	4922097	4675688
No. of interconnects	276501	82041
Macro coordination number, (MCN)	2.1	2.74
Avg. macro-pore diameter μm	6.87	12.43
Avg. macro-throat diameter μm	4.96	11.83
Absolute permeability (mD)	0.176	558
Formation Factor	158	6.4
Porosity (%) $\phi_{\text{tot}}/\phi_{\text{matrix}}/\phi_{\text{macro}}$	12.1/5.5/6.6	18.6/8.7/9.9

Table 3: Comparison of hybrid algorithm with the experimental values, * experimental range for this value is taken from [50].

Sample	Experimental porosity	Hybrid porosity	Experimental Permeability (mD)	Hybrid Permeability	Experimental FF	Hybrid FF
Massangis limestone	11.6	12.1	0.03-0.07	0.176	71-89	158
Estailades carbonate	23 - 25	18.6	257 - 320	558	23-25*	6.4

This study has demonstrated that for the 3D and 3-phase images the hybrid algorithm was successfully applied on the selected subsection of the samples and the transport calculations of permeability and formation factor were done using the equations given in Chapter 4. The main assumption used in our calculations was regarding the assignment of low resistance to flow in the ‘interconnects’, which provides a communication link between macropores and the micropores in the matrix region. The results of permeability and formation factor obtained are within the given tolerable range. We have explored the results in detail below and prepared 3D images of the network in Paraview Figure 28 and Figure 32.

Massangis Jaune Limestone is an ooid-dominated grainstone containing detrital micrite and bioclasts. Calcite cement rims have formed around the grains, strongly reducing the pore space. Microporosity can be found in the partially dissolved dolomite lining the molds and in local ooids [49]. It can be observed from the segmented image shown in Figure 27, that the type of microporosity is pore lining and pore filling, which results in serial coupling between micro and macroporosity regions and as a result, despite having a lower percentage in total porosity, the microporosity dominates the flow properties in the sample. The subsection of the image selected

for network extraction contains $320 \times 320 \times 300$ voxels with a resolution of $4.53 \mu\text{m}$, representing a rock volume of 2.86 mm^3 . The image has 5.5% matrix voxels and 6.6% macropore voxels. Network characteristics are shown above in Table 2.

Sensitivity of permeability and formation factor with microporosity characteristics of grain size and porosity values of Massangis Limestone indicates that assigning a lower value of matrix porosity results in lower overall permeability and larger formation factor for the sample thus confirming the serial coupling. Therefore, we can conclude that there is a strong dependence of transport properties on porosity in the matrix region (micropores), in the analyzed sample. The input parameters of matrix porosity are difficult to determine since they require higher resolution images, in this work it is assumed that the grain size in the matrix region is below the image resolution, grain size has shown to have a minor impact on the overall permeability. The average macro coordination number (MCN) give the average number of throats connected to a pore body. It is observed that MCN of Massangis Limestone is lower than Estailades carbonate indicating lower connectivity. The porosity values of the extracted images closely matched with the experimental values given for both the samples thus confirming a good three-phase segmentation of the samples.

Our hybrid algorithm overpredicts the permeability by a factor of approximately 3 in case of Massangis Limestone which is within the acceptable range. However, this variation could be due to three factors: our assumption of circular tube geometry for the macrothroats with no tortuosity or surface roughness, smaller section of the image taken due to computational limitations and could be due to better connectivity of microporosity in the matrix region with the macropores, since we have assigned low resistance/high conductance to the interconnects. Formation factor for the Massangis limestone [51] is overpredicted by the factor of approximately 2 which could be the result of higher calculated porosity and permeability values. The histograms for pore diameter, throat diameter and throat lengths for Massangis limestone

sample are shown in Figure 26. The average pore diameter is $6.87\mu m$. while average macrothroats diameter is $4.96\mu m$. The histogram of pore size distribution for macropores indicates a unimodal pore size distribution with a long tail towards larger pore sizes for both the samples. The location of main peak of macropores for the two samples are also similar, however Estailades carbonate sample has larger sizes of macropores.

Estailades carbonate is a monomineralic, calcite grainstone and its porosity consists of intergranular macropores and intragranular micropores, while microporosity makes up major portion of the total porosity. The subsection of the image selected for network generation contains $210 \times 210 \times 240$ voxels with a resolution of $3.1 \mu m$ representing a rock volume of $0.315 mm^3$. For the 2D images we have observed that high permeability samples have high percentage of connected microporosity and the ratio of macro to microporosity is mostly equal to or less than 1. For 3D image our algorithm overpredicts permeability by a factor of approximately 2 for the Estailades carbonate sample, which given the same reasons above for Massangis limestone, is reasonable. For the Estailades carbonate the calculated formation factor is underpredicted by a factor of 3.7 but is still in the good agreement range with the experimental value. Estailades carbonate has slightly higher percentage of microporosity in the sample, both microporosity and macroporosity here is known to act as two parallel flow systems [49] and as a result the impact of microporosity is not as dominant in controlling the overall flow properties as indicated for Massangis limestone sample. However, the parallel system and the larger sizes of macropores and macrothroats results in higher permeability values for the Estailades carbonate sample. The histogram for Estailades carbonate sample of pore diameter, throat diameter and throat length are shown in Figure 30. The average macropore diameter is $12.43 \mu m$ while average macrothroats diameter is $11.83 \mu m$.

5 Conclusions and future work

5.1 Conclusions

In this work, a hybrid pore network extraction method for multiscale materials was successfully developed with a cubic grid applied in the matrix region which is in communication with the neighbouring or attached macropores and thus a hybrid multiscale network is created. The multiscale pore network extraction algorithm was tested on different 2D, and 3D artificial and real images segmented into three phases, we selected Massangis Limestone and Estailades carbonate SEM images. As demonstrated previously, the algorithm is fast, less computationally intensive and also correctly identifies and connects the macropores with their surrounding micropores pores in the matrix by making new throats connections, which was the main objective of this exercise.

On the network generated, porosity and the transport properties i.e., permeability and Formation Factor of the resulting merged network were calculated. Furthermore, the generated network was validated with real sandstones and carbonate rocks and tested for mass transfer accuracy.

5.2 Further studies

Further studies are suggested which should proceed first with validation of the algorithm results using Direct Numerical Simulation techniques such as Lattice Boltzmann method where the governing equations of flow and transport are computed directly on the image. After validation, calculation of multiphase flow properties with varying various input parameters should be studied.

It is also recommended to rigorously generate massive images which could more closely represent real rocks. It is hypothesized that by generating massive images as recommended in the research work and applying the presented multiscale network extraction algorithm on these massive artificial images. The resulting extracted network model will represent a larger sample, closer to actual rock and will give fast, more reliable predictions of actual petrophysical properties at core scale which can be reliably input for reservoir scale simulation.

Since geometry plays a key role in conductance calculations, we recommend that different types of shapes be investigated regarding the geometry of the ‘interconnects’ for improved conductance calculations. In our case we have applied minimum resistance by assigning high values to the hydraulic and diffusive conductance, however these should be calculated by using appropriate geometry. We also recommend using a thin circular disk shaped ‘interconnects’ which gives minimum resistance to flow this should however be further investigated.

A pore network model of the hierarchical reservoir rock should be obtained by extracting pore networks from images that possess information at several scales in a single step. Multiscale image cannot currently be obtained from tomography equipment, so massive images should be artificially created that span several length scales. Artificial generation of images to match known structural and statistical properties is a well-established technique, so this task should leverage such work to create images that are representative of several scales simultaneously. This approach is now feasible due to recent developments in high performance network extraction algorithms within our group, capable of managing 5000^3 images, or larger.

Lastly, it is recommended to use the developed modeling framework to evaluate formation properties such as relative permeability, formation factor and resistivity index and by evaluating realistic water saturation values, then upscaling those properties for use in reservoir simulation. This will lead to enhanced reservoir characterization, resulting in application to better reservoir

management, production planning and improved recovery from difficult/complex oil and gas reservoirs. It is also proposed to use one of available reservoir simulators such as the Computer Modeling Group's CMG-GEM reservoir simulator which is a commercial software and is used for compositional, chemical, and unconventional reservoir modeling. Another example is a freely available MATLAB Reservoir Simulation Toolbox. The model presented and upscaling results can then be validated with the data and results from the industry papers available in public domain.

References

- [1] OPEC, “2018 World Oil Outlook.” .
- [2] BP, “BP Statistical Review of World Energy.” 2019.
- [3] IEA, “World Energy Outlook,” 2020. .
- [4] ExxonMobil, “2019 Outlook for Energy.” 2019.
- [5] J. Aghighi, M. Gostick, “Pore network modeling of phase change in PEM fuel cell fibrous cathodes,” *J. Appl. Electrochem*, vol. 47, pp. 1323–1338, 2017.
- [6] C. F. Berg, “Re-examing Archie’s law: Conductance description by tortuosity and constriction,” *Phys. Rev. E*, no. E 86, 046314, 2012.
- [7] Z. et. al. Liang, “Geometric and Topological Analysis of Three-Dimensional Porous Media: Pore Space Partitioning Based on Morphological Skeletonization,” vol. 13–24, 2000.
- [8] T. Bultreys, W. De Boever, and V. Cnudde, “Imaging and image-based fluid transport modeling at the pore scale in geological materials: A practical introduction to the current state-of-the-art,” *Earth-Science Rev.*, vol. 155, pp. 93–128, 2016, doi: 10.1016/j.earscirev.2016.02.001.
- [9] C. H. Arns, H. Jiang, H. Dai, I. Shikhov, N. SayedAkram, and J. Y. Arns, “Pore-type partitioning for complex carbonates: Effective versus total porosity and applications to electrical conductivity,” *SPWLA 59th Annu. Logging Symp. 2018*, no. 1990, 2018.
- [10] A. Farouk, S. Wibowo, G. Aillud, A. Al Shehhi, and K. Kingsley, “Water saturation uncertainty of tight, microporosity dominated carbonate reservoirs and the impact on hydrocarbon volume; case study from abu Dhabi, uae,” *SPWLA 55th Annu. Logging Symp. 2014*, no. March, 2014.
- [11] O. S. Al-Jaaidi *et al.*, “A Multi-Disciplinary Approach to Characterize Microporosity Impact on Arab D Reservoir, a Case Study from the Bul Hanine Field, Qatar,” 2015, doi:

10.2523/iptc-18501-ms.

- [12] E. A. Clerke, J. J. Funk, and E. Shtepani, “Spontaneous imbibition of water into oil saturated M-1 bimodal limestone,” *Soc. Pet. Eng. - Int. Pet. Technol. Conf. 2013, IPTC 2013 Challenging Technol. Econ. Limits to Meet Glob. Energy Demand*, vol. 7, no. September, pp. 5497–5513, 2013, doi: 10.2523/iptc-17162-ms.
- [13] S. M. Fullmer *et al.*, “Microporosity: Characterization, distribution, and influence on oil recovery,” *Soc. Pet. Eng. - 30th Abu Dhabi Int. Pet. Exhib. Conf. ADIPEC 2014 Challenges Oppor. Next 30 Years*, vol. 4, pp. 2810–2826, 2014, doi: 10.2523/iptc-17629-ms.
- [14] J. Lucia, *Carbonate Reservoir Characterization An Integrated Approach 2nd Edition*. 2007.
- [15] F. A. L. Dullien, *Porous Media Fluid Transport and Pore Structure Second Edition*. 1992.
- [16] M. Abu-Al-Saud, A. Gmira, S. Al-Enezi, and A. Yousef, “Pore-scale simulation of fluid flow in carbonates using micro-CT scan images,” *Int. Pet. Technol. Conf. 2020, IPTC 2020*, 2020, doi: 10.2523/iptc-19832-ms.
- [17] D. L. Cantrell and R. M. Hagerty, “Microporosity in Arab Formation Carbonates, Saudi Arabia,” *GeoArabia*, vol. 4, no. 2, pp. 129–154, 1999.
- [18] M. Mousavi, M. Prodanovic, and D. Jacobi, “New classification of carbonate rocks for process-based pore-scale modeling,” *SPE J.*, vol. 18, no. 2, pp. 243–263, 2013, doi: 10.2118/163073-PA.
- [19] R. et. al. Stanely, “Microporosity Spatial Modeling in a Giant Carbonate Reservoir,” *IPTC*, no. 18327-MS, 2015.
- [20] P. R. Thomson, A. Hazel, and S. Hier-Majumder, “The influence of microporous cements on the pore network geometry of natural sedimentary rocks,” *Front. Earth Sci.*, vol. 7, no. March, pp. 1–14, 2019, doi: 10.3389/feart.2019.00048.
- [21] T. Bultreys, L. Van Hoorebeke, and V. Cnudde, “Multi-scale, micro-computed

- tomography-based pore network models to simulate drainage in heterogeneous rocks,” *Adv. Water Resour.*, vol. 78, pp. 36–49, 2015, doi: 10.1016/j.advwatres.2015.02.003.
- [22] V. Hebert, C. Garing, L. Luquot, P. A. Pezard, and P. Gouze, “Multi-scale X-ray tomography analysis of carbonate porosity,” *Geol. Soc. Spec. Publ.*, vol. 406, no. 1, pp. 61–79, 2015, doi: 10.1144/SP406.12.
- [23] Q. Lin, A. M. Alhammadi, Y. Gao, B. Bijeljic, and M. J. Blunt, “Iscal for complete rock characterization: Using pore-scale imaging to determine relative permeability and capillary pressure,” *Proc. - SPE Annu. Tech. Conf. Exhib.*, vol. 2019-Septe, 2019, doi: 10.2118/196082-ms.
- [24] S. Sadeghnejad and J. Gostick, “Multiscale Reconstruction of Vuggy Carbonates by Pore-Network Modeling and Image-Based Technique,” *SPE J.*, vol. 25, no. 1, pp. 253–267, 2020, doi: 10.2118/198902-PA.
- [25] A. Mehmani, R. Verma, and M. Prodanović, “Pore-scale modeling of carbonates,” *Mar. Pet. Geol.*, vol. 114, no. July 2019, p. 104141, 2020, doi: 10.1016/j.marpetgeo.2019.104141.
- [26] M. J. Blunt, *Multiphase Flow in Permeable Media. A Pore-Scale Perspective*, vol. 56, no. 5. 2017.
- [27] L. P. Dake, “The Practice of Reservoir Engineering (Revised Edition),” *Elsevier*, 2001.
- [28] A. S. Ziarani and R. Aguilera, “Pore-throat radius and tortuosity estimation from formation resistivity data for tight-gas sandstone reservoirs,” *J. Appl. Geophys.*, vol. 83, pp. 65–73, 2012, doi: 10.1016/j.jappgeo.2012.05.008.
- [29] M. A. Knackstedt *et al.*, “Archie’s exponents in complex lithologies derived from 3D digital core analysis,” *48th Annu. Logging Symp. 2007*, no. 1, pp. 1–16, 2007.
- [30] Z. Bassiouni, “Theory, Measurement, and Interpretation of Well Logs,” 1994.
- [31] I. Fatt, “The network model of porous media I.,” *AIME*, no. 207, pp. 144–159, 1956.
- [32] J. C. Russ and F. B. Neal, *The Image Processing Handbook*. 2018.

- [33] K. E. Thompson, C. S. Willson, C. D. White, S. L. Nyman, J. P. Bhattacharya, and A. H. Reed, “Application of a new grain-based reconstruction algorithm to microtomography images for quantitative characterization and flow modeling,” *SPE J.*, vol. 13, no. 2, pp. 164–176, 2008, doi: 10.2118/95887-PA.
- [34] a P. Sheppard, R. M. Sok, H. Averdunk, V. B. Robins, and a Ghous, “Analysis of Rock Microstructure Using High- Resolution X-Ray Tomography,” *Proc. Int. Symp. Soc. Core Anal.*, no. November 2014, pp. 1–12, 2006, [Online]. Available: d:%5CBiblioGroupe%5CFichiers_PDF%5CSheppard_SCA_2006.pdf.
- [35] A. Rabbani, S. Jamshidi, and S. Salehi, “An automated simple algorithm for realistic pore network extraction from micro-tomography images,” *J. Pet. Sci. Eng.*, vol. 123, pp. 164–171, 2014, doi: 10.1016/j.petrol.2014.08.020.
- [36] J. T. Gostick, “Versatile and efficient pore network extraction method using marker-based watershed segmentation,” *Phys. Rev. E*, vol. 96, no. 2, pp. 1–15, 2017, doi: 10.1103/PhysRevE.96.023307.
- [37] P. Tahmasebi and S. Kamrava, “Rapid multiscale modeling of flow in porous media,” *Phys. Rev. E*, vol. 98, no. 5, pp. 1–13, 2018, doi: 10.1103/PhysRevE.98.052901.
- [38] S. Békri, C. Laroche, and O. Vizika, “Pore Network Models To Calculate Transport and Electrical Properties of Single or Dual-Porosity Rocks,” *Int. Symp. Soc. Core Anal.*, no. January 2015, pp. 1–16, 2005.
- [39] D. Bauer, S. Youssef, M. Fleury, S. Bekri, E. Rosenberg, and O. Vizika, “Improving the Estimations of Petrophysical Transport Behavior of Carbonate Rocks Using a Dual Pore Network Approach Combined with Computed Microtomography,” *Transp. Porous Media*, vol. 94, no. 2, pp. 505–524, 2012, doi: 10.1007/s11242-012-9941-z.
- [40] Z. et. al. Jiang, “Representation of multiscale heterogeneity via multiscale pore networks,” *Water Resour. Res.*, vol. 49, pp. 5437–5449, 2013.
- [41] M. Prodanović, A. Mehmani, and A. P. Sheppard, “Imaged-based multiscale network

- modelling of microporosity in carbonates,” *Geol. Soc. Spec. Publ.*, vol. 406, no. 1, pp. 95–113, 2015, doi: 10.1144/SP406.9.
- [42] T. Bultreys, W. De Boever, L. Van Hoorebeke, and V. Cnudde, “A multi-scale, image-based pore network modeling approach to simulate two-phase flow in heterogeneous rocks,” *Int. Symp. Soc. Core Anal. 16-21 August, 2015*, pp. 1–12, 2015, [Online]. Available: <https://biblio.ugent.be/publication/6923699>.
- [43] N. Hakimov, A. Zolfaghari, A. Kalantari-Dahaghi, S. Negahban, and G. Gunter, “Pore-scale network modeling of petrophysical properties in samples with wide pore size distributions,” *Soc. Pet. Eng. - Abu Dhabi Int. Pet. Exhib. Conf. 2018, ADIPEC 2018*, 2019, doi: 10.2118/192890-ms.
- [44] A. Mehmani and M. Prodanović, “The effect of microporosity on transport properties in porous media,” *Adv. Water Resour.*, vol. 63, pp. 104–119, 2014, doi: 10.1016/j.advwatres.2013.10.009.
- [45] A. Rabbani, M. Babaei, and F. Javadpour, *A Triple Pore Network Model (T-PNM) for Gas Flow Simulation in Fractured, Micro-porous and Meso-porous Media*, vol. 132, no. 3. Springer Netherlands, 2020.
- [46] Q. Xiong, T. G. Baychev, and A. P. Jivkov, “Review of pore network modelling of porous media: Experimental characterisations, network constructions and applications to reactive transport,” *J. Contam. Hydrol.*, vol. 192, pp. 101–117, 2016, doi: 10.1016/j.jconhyd.2016.07.002.
- [47] Ş. Merey, “Prediction of transport properties for the Eastern Mediterranean Sea shallow sediments by pore network modelling,” *J. Pet. Sci. Eng.*, vol. 176, no. December 2018, pp. 403–420, 2019, doi: 10.1016/j.petrol.2019.01.081.
- [48] J. T. Dewan, *Essentials of Modern Open-hole Log Interpretation*. 1983.
- [49] T. Bultreys *et al.*, “Investigating the relative permeability behavior of microporosity-rich carbonates and tight sandstones with multiscale pore network models,” *J. Geophys. Res.*

- Solid Earth*, vol. 121, no. 11, pp. 7929–7945, 2016, doi: 10.1002/2016JB013328.
- [50] M. A. Ioannidis and I. Chatzis, “Network modelling of pore structure and transport properties of porous media,” *Chem. Eng. Sci.*, vol. 48, no. 5, pp. 951–972, 1993, doi: 10.1016/0009-2509(93)80333-L.
- [51] L. Casteleyn *et al.*, “An integrated study of the petrophysical properties of carbonate rocks from the ‘Oolithe Blanche’ formation in the Paris Basin,” *Tectonophysics*, vol. 503, no. 1–2, pp. 18–33, 2011, doi: 10.1016/j.tecto.2010.09.031.
- [52] G. Scott, “Multi-scale Image-Based Pore Space Characterisation and Pore Network Generation: Case Study of a North Sea Sandstone Reservoir,” *Transp. Porous Media*, vol. 129, no. 3, pp. 855–884, 2019, doi: 10.1007/s11242-019-01309-8.
- [53] C. Lu and H. Zoya, “Directional-Permeability Assessment in Formations with Complex Pore Geometry with a New Nuclear-Magnetic-Resonance-Based Permeability Model,” *SPE J.*, vol. 21, no. 4, pp. 1436–1449, 2016, doi: 10.2118/179734-pa.
- [54] K. Kawaura, A. Hanyu, Y. Mino, S. Takahashi, and T. Tsuji, “Resistivity measurement affected by saturating fluid concentration and pore geometry,” *21st Form. Eval. Symp. Japan 2015*, no. 2, pp. 1–8, 2015.
- [55] J. Gostick, “A three-phase image segmentation algorithm,” *Chem. Eng. Univ. Waterloo Canada*, 2020.

Appendix A

The steps required to generate a multiscale network from realistic segmented images are explained below:

1. Extract regions in voids. Apply Porespy filter SNOW partitioning on void to get the regions of macropores. In this step SNOW algorithm uses a marker-based watershed segmentation to partition the image into regions belonging to each pore.
2. Obtain a rim of voxels around each region obtained from step 1. Dilate the output from step 1 using binary dilation function from skimage morphology. Multiplying the resulting dilation with the matrix region of the image gives the surrounding rim of microporous region only which is around or surrounding each macropore region.
3. Combine each of the region from step1 with its rim obtained from step 2. This will give the required region together with its surrounding communicating rim. The combined output is named regrim. The concept is explained in Figure 18.
4. Obtain newrims which are defined as rims having the same color/number as its enclosing region. Apply maxfilter function from Scipy.ndimage on the result obtained from step 3. A maxfilter is used to diminish noise by replacing each voxel in the image with the maximum value found in neighborhood that is defined by a structuring element R – thus the local peaks retain their value while other voxels are overwritten with a larger value.
5. Then multiply the result with the rim to get newrims. Here, labels the dilation with the same color to identify which surrounding rim (i.e., newrims) belong

to which region of macropore. The resulting images and networks are shown in Figure 20.

6. Identify peaks of each macropore region. Thus, giving the total number of macropores in the image and each macropore pore peak is identified with its surrounding/neighboring rim.
7. In regions where matrix is labelled as 1s and solid grains labeled as 0s, insert CubicTemplate function from OpenPNM in matrix region only. This gives the network pn_matrix in the matrix (microporosity) region. The CubicTemplate returns a network of simple cubic lattice with arbitrary domain shape specified by a template image. All locations in the image that are marked as True are kept while the rest are trimmed to yield the shape.
8. Create a new array which gives all the matrix pores that index into newrims and thus identify which matrix pores are besides each macropores in the network extraction.
9. Make a new network in macropores region using Porespy SNOW network extraction function. This gives the network net1 and name it pn_void.
10. Put labels for the matrix as ‘micropores’ and macropore regions as ‘macropores’. Import the network pn_void and transfer all geometrical properties from pn_void to geom_macro.
11. Merge the two networks together using OpenPNM merge function which combines multiple networks into one without stitching. The two networks pn_void and pn_matrix are merged into one.
12. Merged network is renamed as ‘combo’.
13. Define geometry objects for micropores.
14. Make throat network connection between macropores region with its surrounding region of micropores in the matrix region thus enabling mass transfer between the two. Then, use extend function in OpenPNM to manually

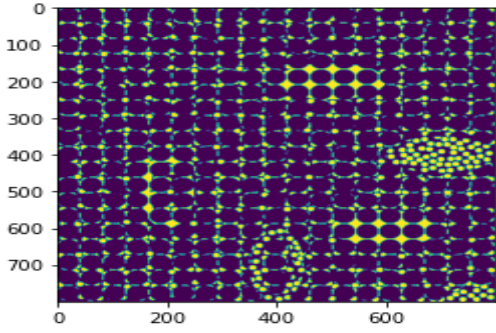
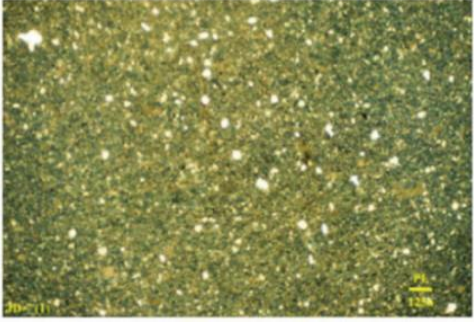
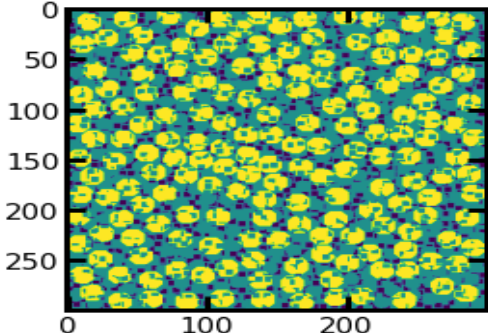
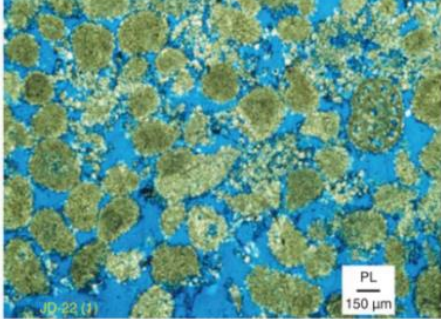
making a list to connect pore number from cubic template to pore number in network extraction, thus add new throat connections for mass transfer between the two regions (matrix and macropores). Extend function adds throats to the network from a list of conns, the list numbering must point to the existing pores.

15. Define geometry objects for newly created throats.
16. Create phase and physics for each of the three geometry objects i.e., geom_macro, geom_micro and geom_new.
17. Carman-Kozeny equation for estimation of Darcy permeability for each voxel and thus find hydraulic conductance g of the matrix for each voxel. Here, the procedure is treating the microporosity as a continuum and estimating the required transport parameter values.
18. Once the pressure in all pores is found and flow rates through all throats is calculated using the OpenPNM rate method calculate effective permeability for the whole network using Darcy's law.
19. Estimate tortuosity of the matrix region by using Bruggeman correlation for spheres. Then calculate Formation Factor using Fick's law on the whole domain.

Note 1. Since Macropores numbers begin with 0 in the merged openPNM network `combo_net`, so it is required to re-number 1s to 0s and so on in list A i.e., `pn` [`'pore.macro_pore_connection`] created in step 8, so that correct macropore should connect its surrounding micropores of same numbers/color.

Appendix B

The artificially generated images as explained in Chapter 4, are demonstrated in the following pages below:

S. No	Generated Image	Real Image
1.		
	2D-2phase image, yellow is matrix, purple is grain	Type I rock sample- Lime mudstone
2.		
	2D-3phase image, void = (purple), grain = (yellow), matrix = (green)	Type II rock sample – Peloidal dolograinstone

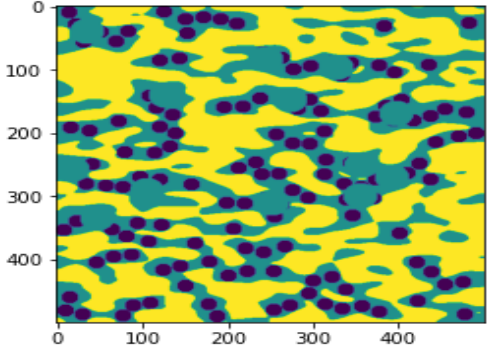
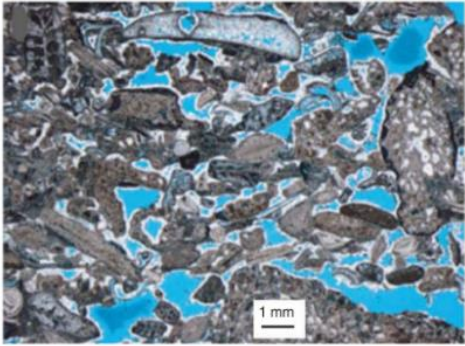
3.		
	2D-3phase image, void = (purple), grain=(yellow), matrix=(green)	Type II rock sample – Limestone, enlarged vuggy porosity (touching vug)

Figure 33 : Artificial image of the rock on the left compared with an actual SEM image on the right. On the right rock types I an II [18] are shown.

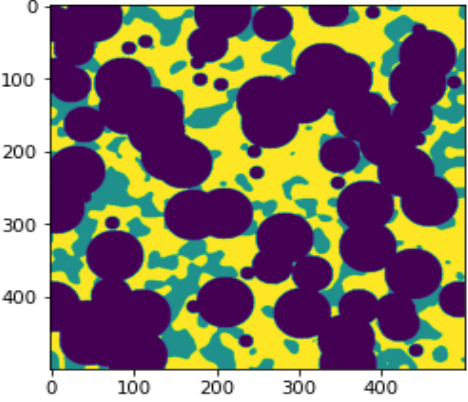
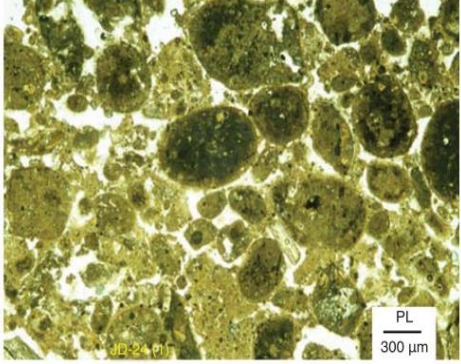
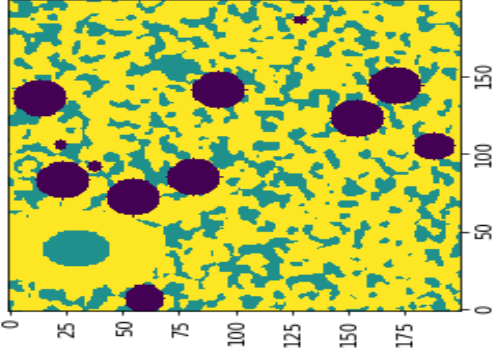
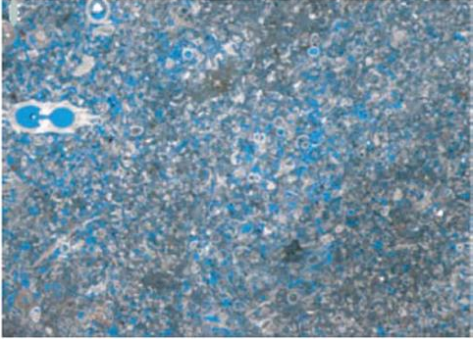
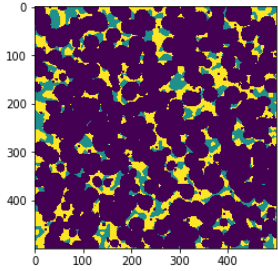
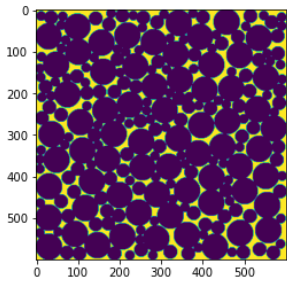
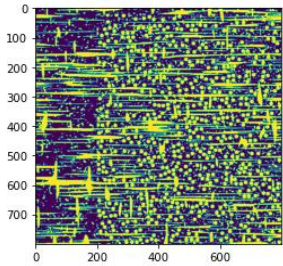
S. No.	Generated Image	Real Image
1		
	2D-3phase image, void = (purple), grain=(yellow), matrix=(green)	Type III rock sample - Low-mud packstone
2.		
	2D-3phase image, Green is void, black are grains, and yellow is matrix.	Type III rock sample – Limestone with fine to medium grained packstone texture, abundant matrix microporosity porosity=18.3%, permeability 545 mD.

Figure 34: Two artificially generated 2-D and 3-phase images and real rock type III are shown in the right column.

S. No.	Artificial Image
1.	
	3D and three-phase image, yellow is matrix, black is solid grains and green is void region.
2.	
	2D and two-phase image, yellow is void, black is solid grains.
3.	
	2D and two-phase image, yellow is void (showing small fractures or touching vugs), black is matrix.

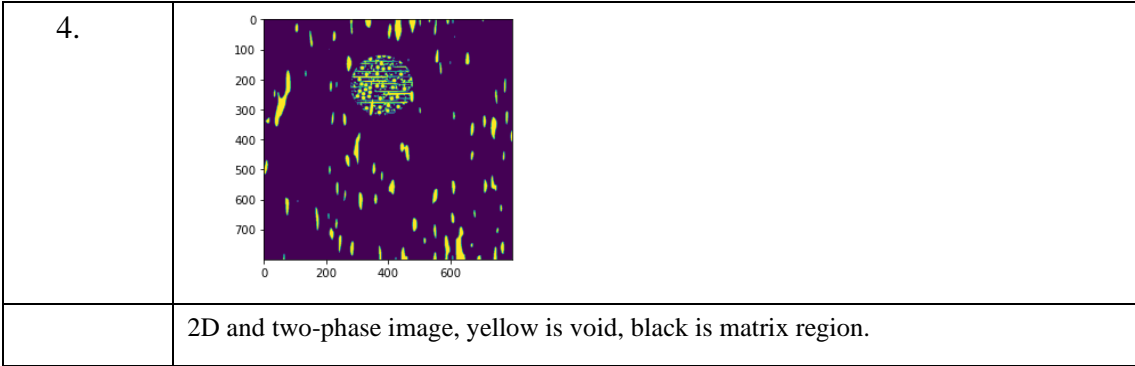


Figure 35: A few more examples of artificially generated images.

Appendix C

Selected sandstones samples and their network extraction are shown below:

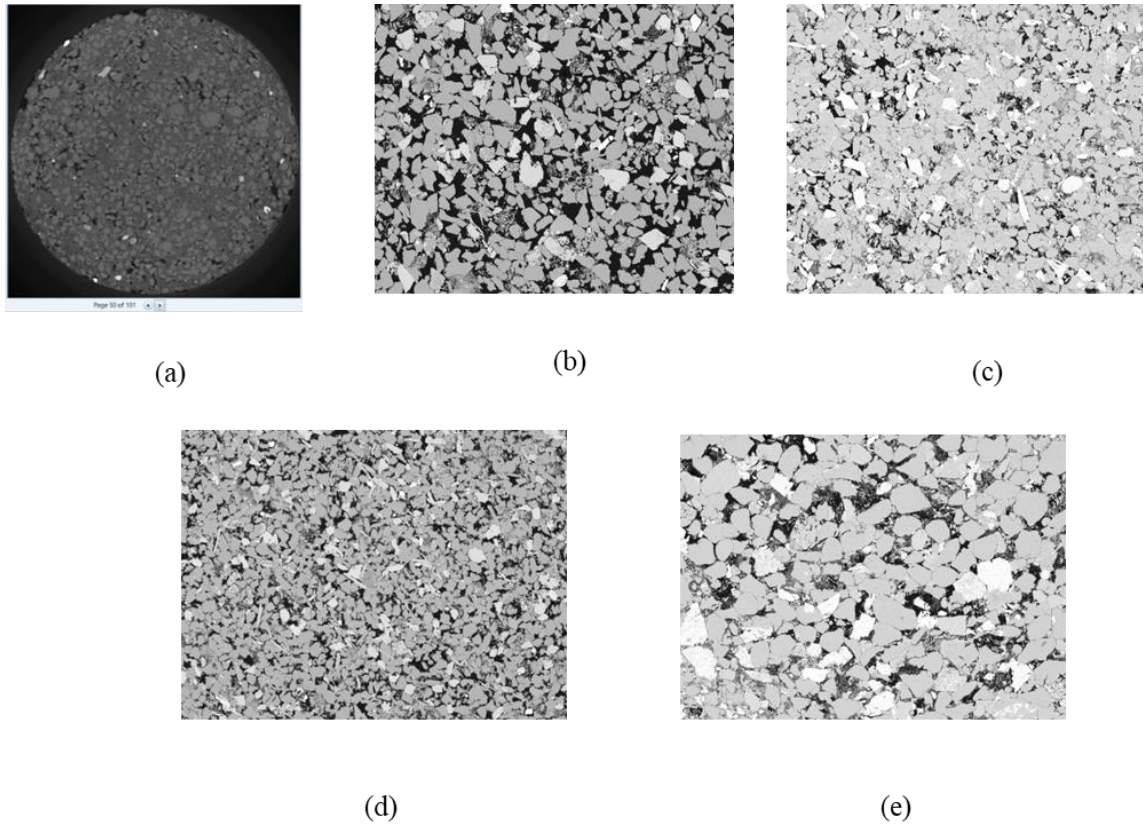


Figure 36: Selected sandstone SEM images for 2D analysis, (a) top left to right Berea sandstone, (b) North Sea sandstone plug 44, (c) North Sea sandstone plug 77, (d) bottom left to right North Sea sandstone plug 130, (e) North Sea sandstone plug 367.

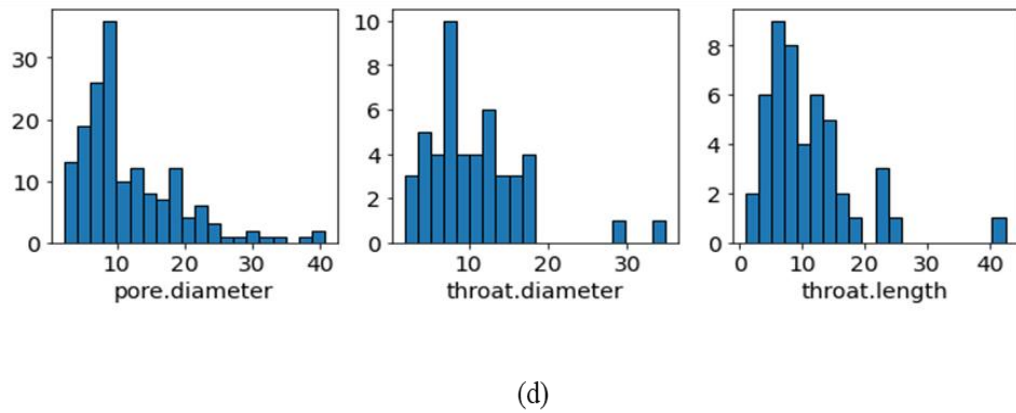
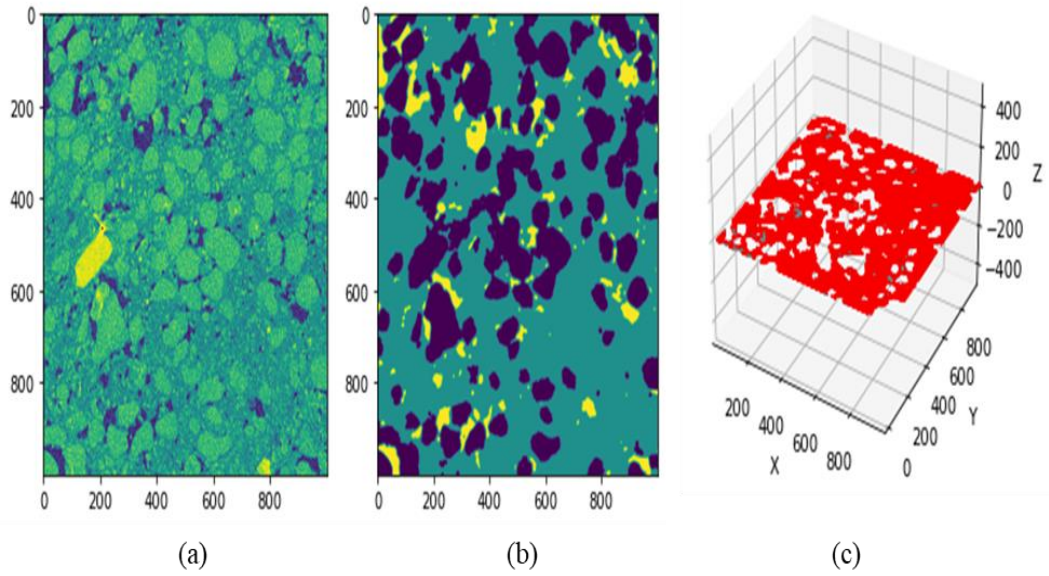
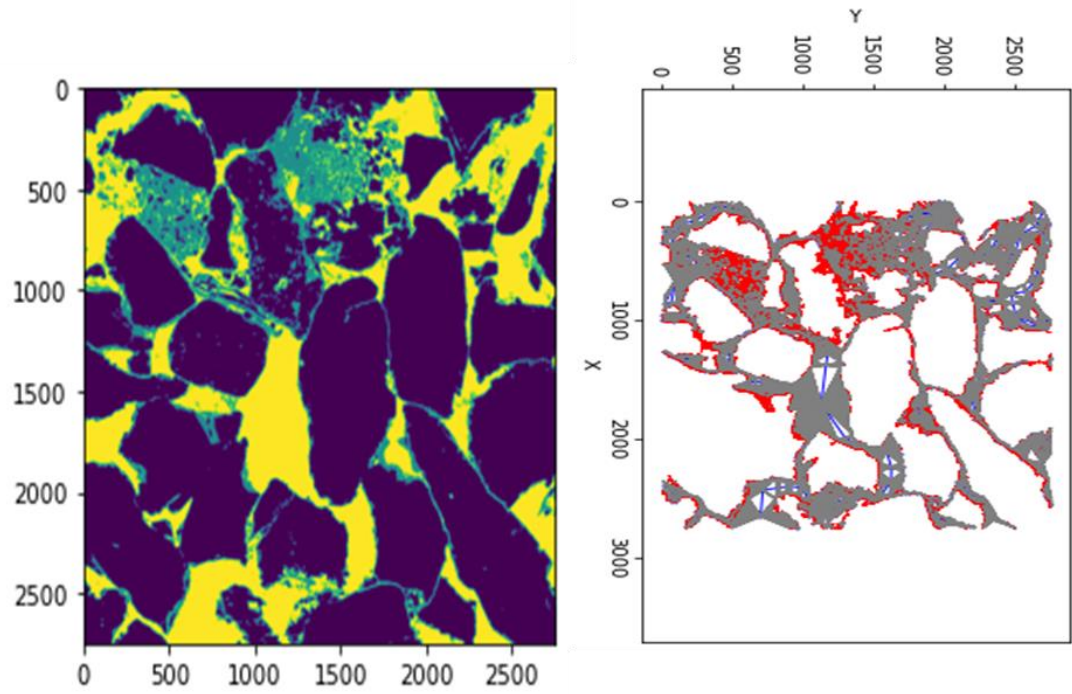
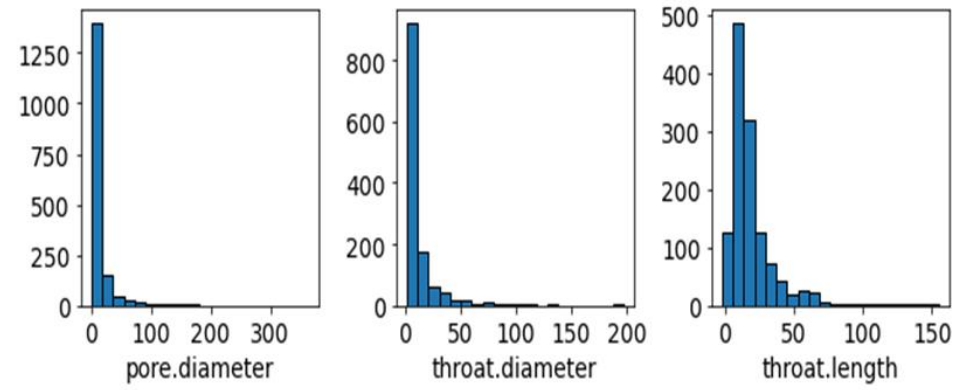


Figure 37: Berea_D_20 sandstone (a) raw image, (b) three-phase segmentation of a selected section, (c) network extraction and (d) histogram of network properties.



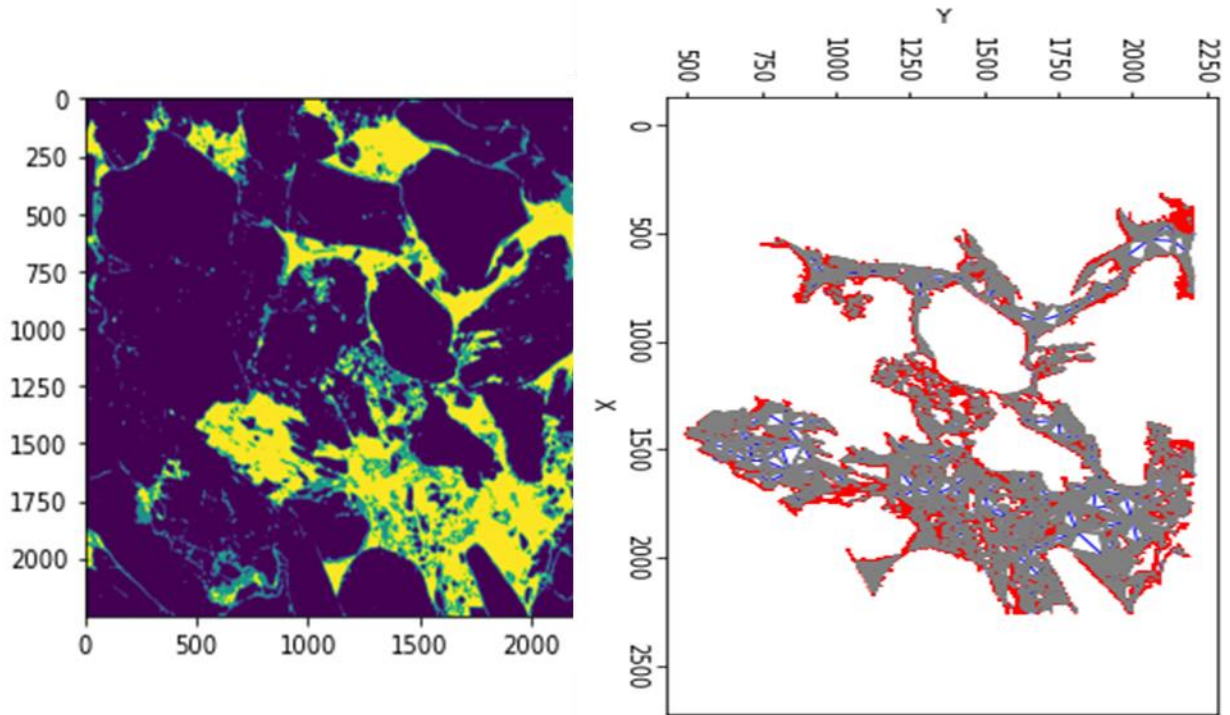
(a)

(b)



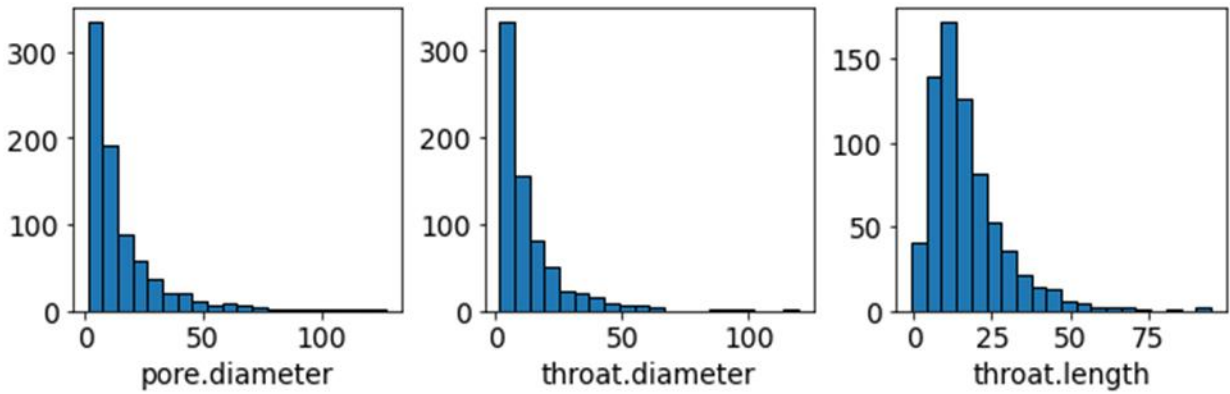
(c)

Figure 38: North Sea sandstone plug 44 a) Three phase segmentation, b) Macropore network and c) histogram of network properties



(a)

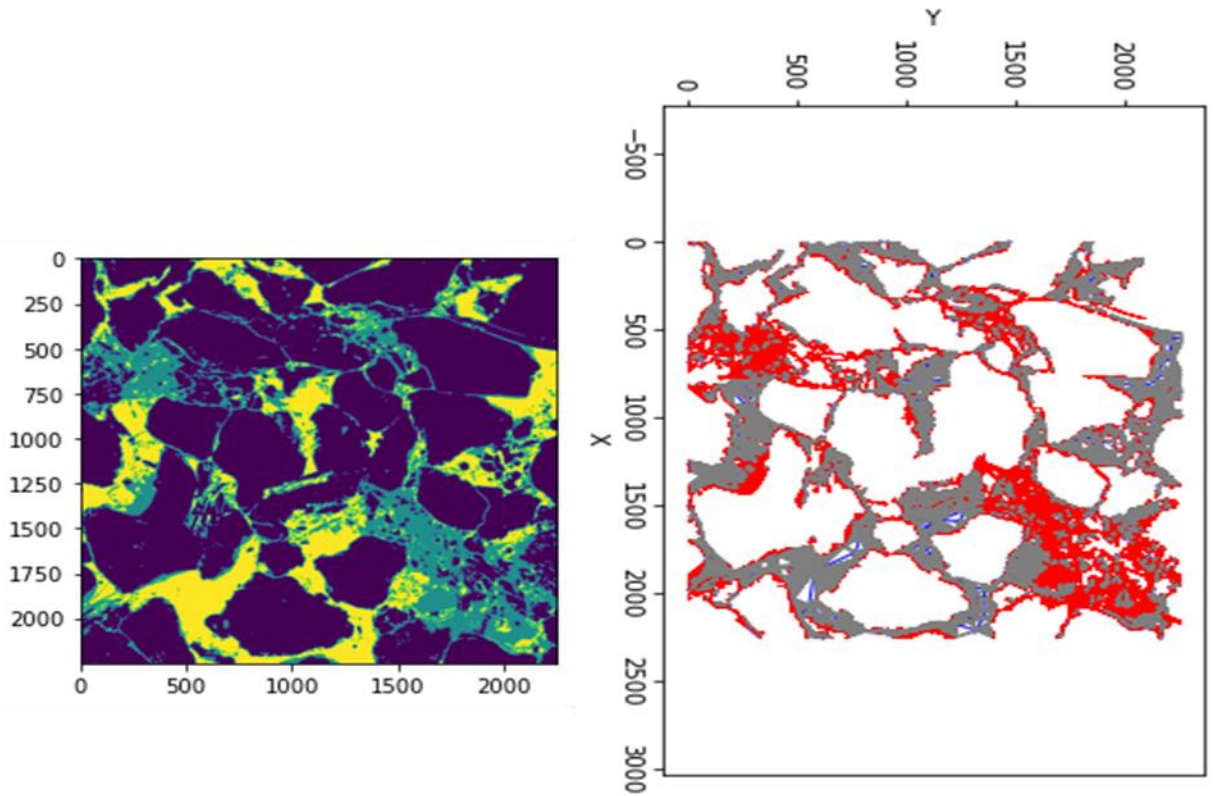
(b)



(c)

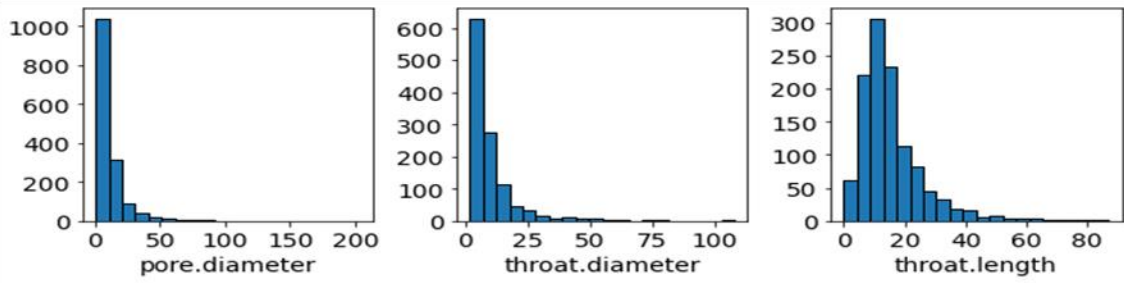
Figure 39: (a) North Sea sandstone plug 77 three-phase segmentation of a selected section

(b) network extraction and (c) histogram of network properties.



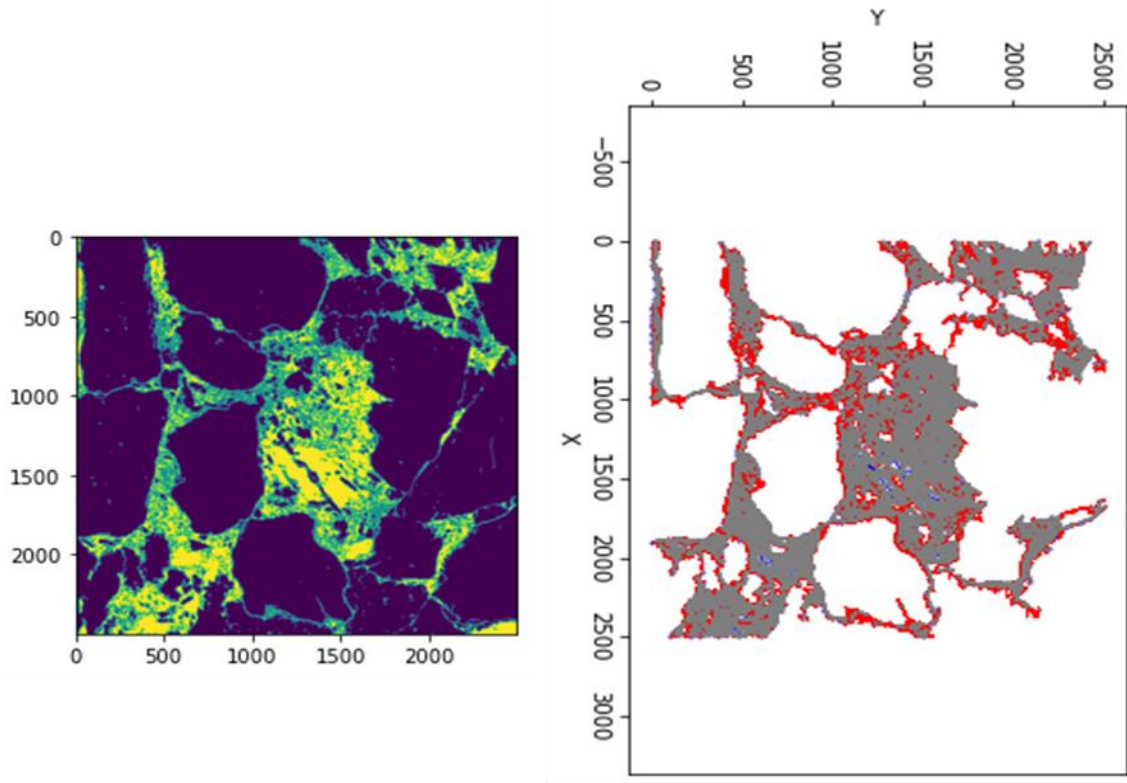
(a)

(b)



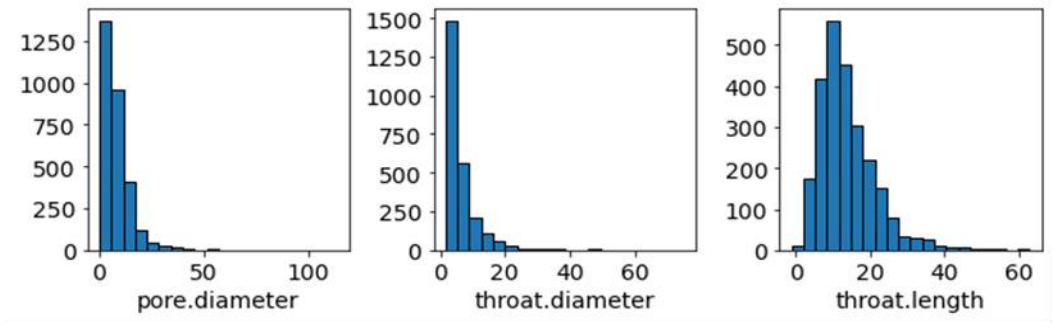
(c)

Figure 40: (a) North Sea sandstone plug 130 three-phase segmentation of a selected section, (b) network extraction and (c) histogram of network properties.



(a)

(b)



(c)

Figure 41: North Sea sandstone plug 367, a) Three-phase segmentation b) Macropore network and c) histogram of network properties.

	3D & 3phase Artificial	D_20_Berea	North Sea sandstone Plug 44	North Sea sandstone Plug 77	North Sea sandstone Plug 130	North Sea sandstone Plug 367
No. of macro- pores	74	164	1660	760	1531	2977
No. of macro- throats	14	48	1268	692	1158	2496
No. of micro- pores	260214	617652	784468	290248	853380	861602
No. of micro- throats	648272	1214622	1429890	518813	1567705	1534907
No. of Interconnects	37320	8842	106254	50711	86751	165739
Avg. macro- pore diameter (μm)	4.26/2. 0	11.69	12.57	15.51	11.08	8.43
Avg. macro- throat dia (μm)	1.8/1.5	10.72	11.79	13.21	9.72	6.07
Absolute permeability (mD)	4937	81.19	119.52	12.98	11.13	20.47
Formation Factor	38	98.55	35.35	29.96	45.69	28.49
Porosity (%) ϕ_{total} , ϕ_{macro} , ϕ_{micro}	16.7 / 8.6 /8.1	63.1/ 6.66/56.44	32.7 / 24.25 / 8.45	23.38 / 17.63 / 5.75	29.31/18. 1/ 11.21	25.72 / 15.23 / 10.89

Table 4: Summary of network statistics for 3D artificial and 2D sandstone samples.

The following analysis is done for 2D simulation carried out on the samples:

Berea is a more homogeneous rock with narrow pore size distribution as compared to more complex sandstone such as North Sea Sandstone which has undergone extensive diagenesis resulting in wide range of pore sizes. We selected Berea since it is a standard material used in geosciences studies and the raw SEM image was available. We have selected the North Sea Sandstone samples, downloaded from digital rocks portal, since these are complex sandstone with wide range of pore size distribution resulting is significant percentage of microporosity which cannot be imaged by the high-resolution SEM as low as $0.27\mu m$. Also, the experimental data for porosity, permeability and FF was available for these sandstones. The four North Sea samples selected are plugs 44, 77, 130 and 367, Scott et al, [52] have conducted detailed fluid flow analysis on these 2D images. Similarly for 2-D analysis on carbonate rock which typically represent multiple porosity systems and multimodal pore size distributions. We have selected a total of four samples, one Savonnières, two Estailades, Austin Chalk [53] downloaded from the Digital rock portal website where we had the option to select only non-segmented raw images since we need to process the raw image into a three phase segmented image. The raw jpg images from digital rock portal were converted to tiff format using ImageJ software.

Berea Sandstone: This rock is a fine grained, fairly consolidated, and poorly sorted sandstone with non calcareous cement present. The range of experimental properties [54] are compared with the hybrid network and values of permeability and formation factor calculated are within the experimental values as given below. The sample has high fraction of well connected microporosity and high porosity within the microporosity region which is reflected in high permeability value:

Experimental

Porosity (%)	<i>FF</i>	Permeability (mD)
16 – 19	47 - 147	36 - 414

Hybrid Algorithm

Sample	Porosity (%)	<i>FF</i>	Permeability (mD)
Berea_D_20	63%	98.5	92.3

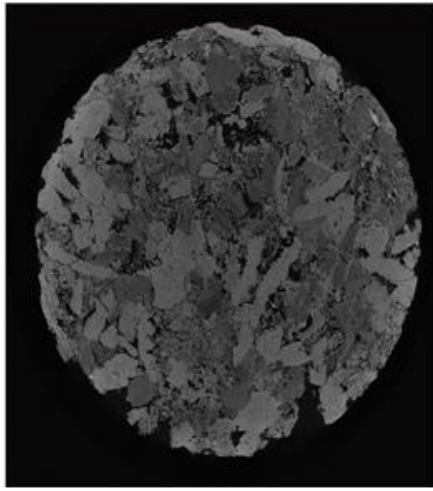
North Sea Sandstone: Samples 44, 77 and 130 [52] used in our work are from lower Fulmar formation of North Sea sandstone reservoir, which is subjected to extensive diagenesis, in sample 130 around two-third of the porosity is microporosity which cannot be resolved. Sample 367 is from Skagerrak formation of North Sea sandstone in which cement and clays are found together with secondary porosity created by partial grain dissolution. Since the available images were of large size, we have validated the code on various subsections of the images. The porosity, permeability and formation factors values calculated by hybrid algorithm for these samples are in close agreement with the experimental values. The larger percentage of microporosity is noted in samples 367 and 130 as compared to sample 44, this is reflected in lower overall permeabilities for these samples.

Experimental

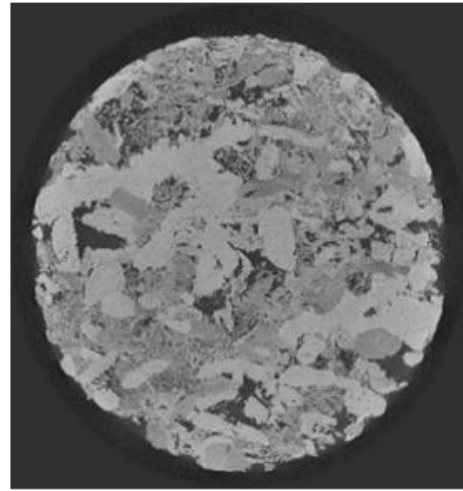
Sample #	Porosity (%)	<i>FF</i>	Permeability (mD)
44	28.3	8.3	557
77	14.2	25	2.7
130	22.8	12.4	5.8
367	16.2	21	45

Hybrid Algorithm

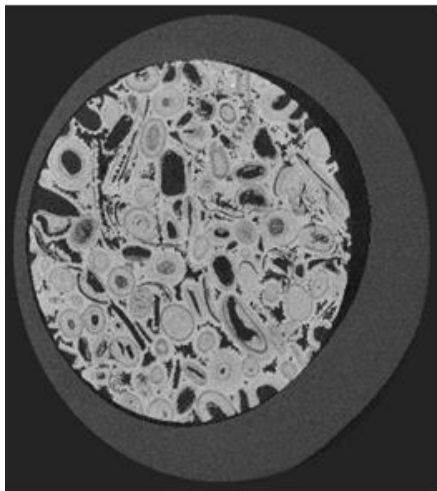
Sample #	Porosity (%), total, macro, micro	FF	Permeability (mD)
44	31.6, 22.8, 8.45	35	421
77	22.88, 18, 4.88	28.96	12.98
130	29.3, 18.1, 11.2	45.7	11.13
367	25.7, 15.2, 10.5	28.49	20.47



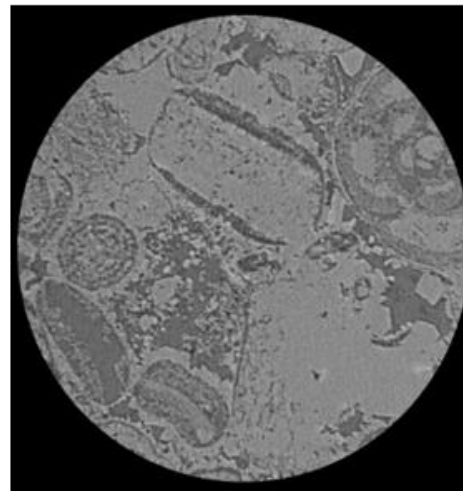
(a)



(b)

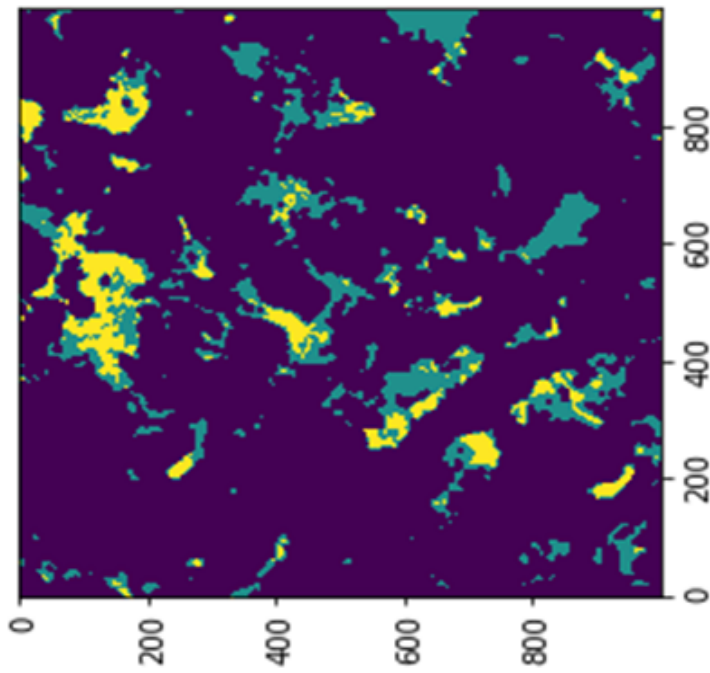


(c)

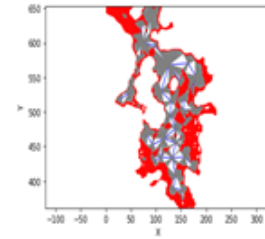


(d)

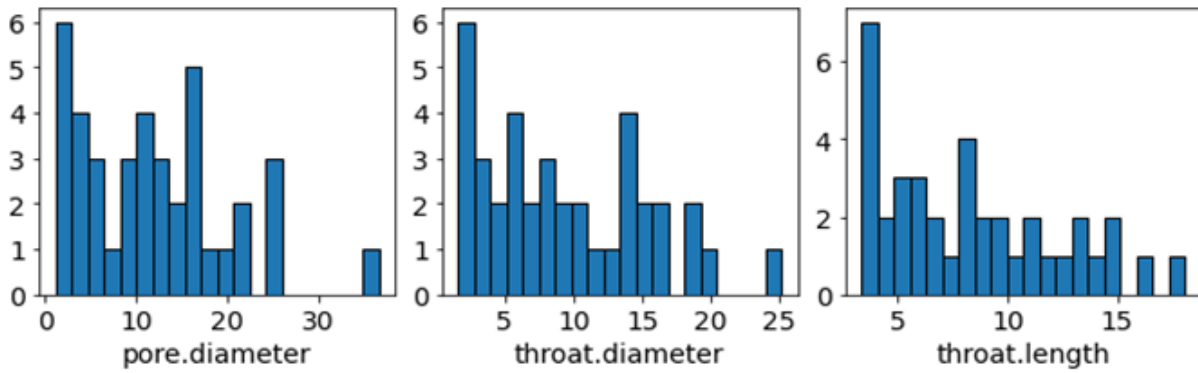
Figure 42: Selected Carbonate SEM images for 2D analysis, (a) top left to right Estailades ES32_0523 (images downloaded from www.digitalrocksportal.org, (b) Estailades ES32_1832, bottom left to right (c) Savonnieres carbonate, (d) Austin chalk.



(a)

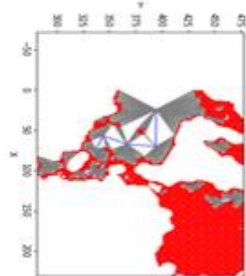
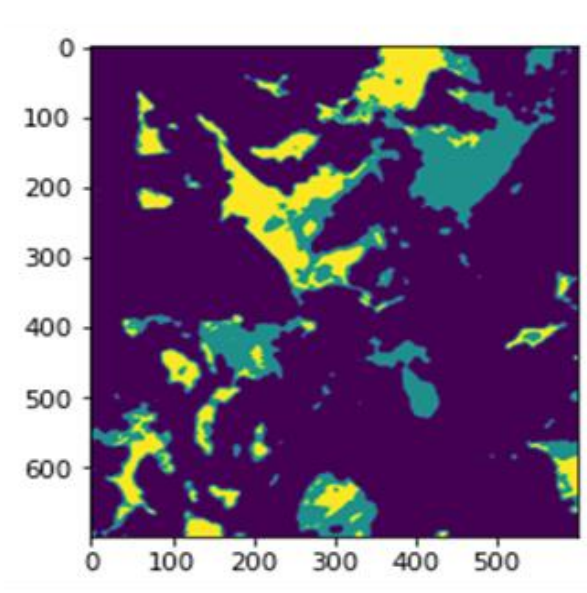


(b)



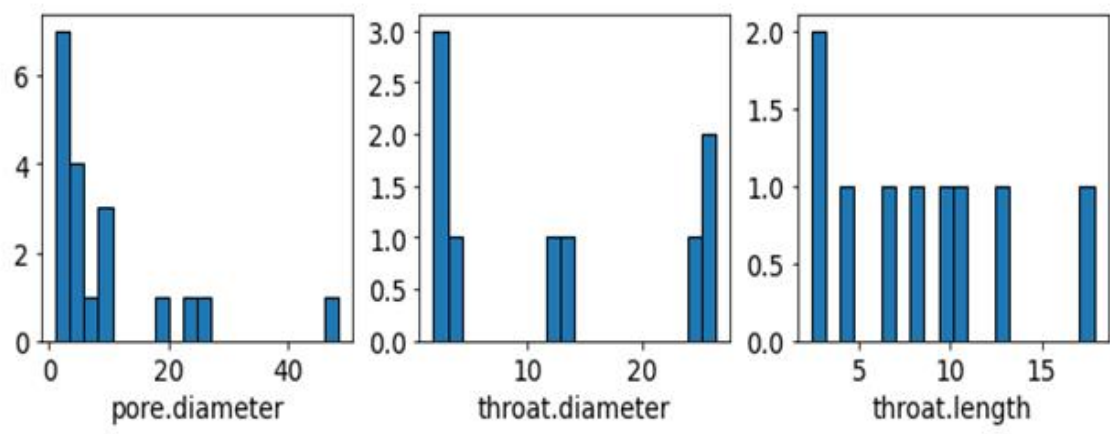
(c)

Figure 43: a) Estailades ES32_0532 three-phase segmentation of a selected section, b) network extraction and c) histogram of network properties.



(a)

(b)



(c)

Figure 44: Estailades ES32_1832 (a) three phase segmentation of a selected section, (b) network extraction and (c) histogram of network properties.

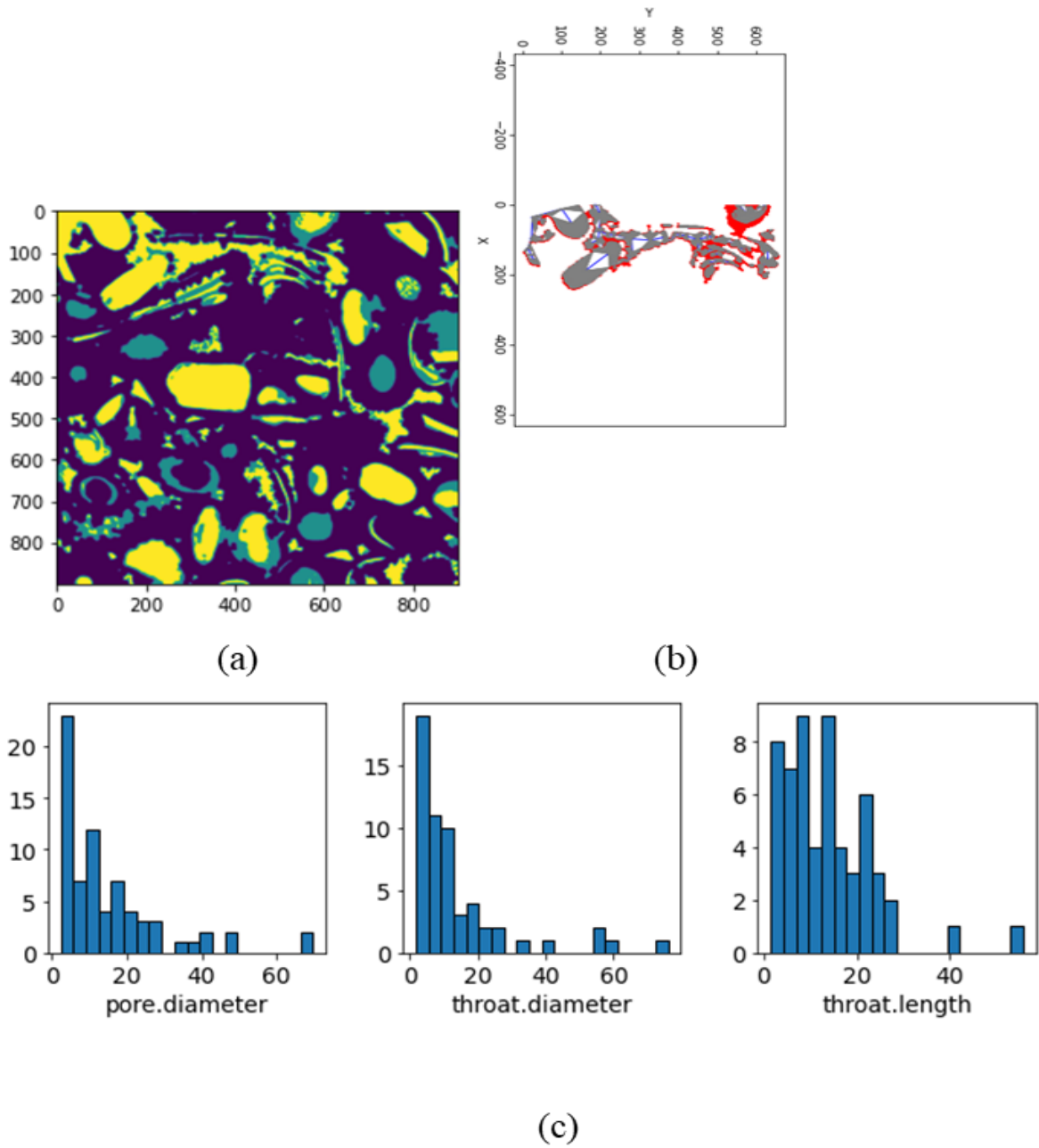


Figure 45: Savonnieres carbonate (a) three phase segmentation of a selected section (b) network extraction and (c) histogram of network properties.

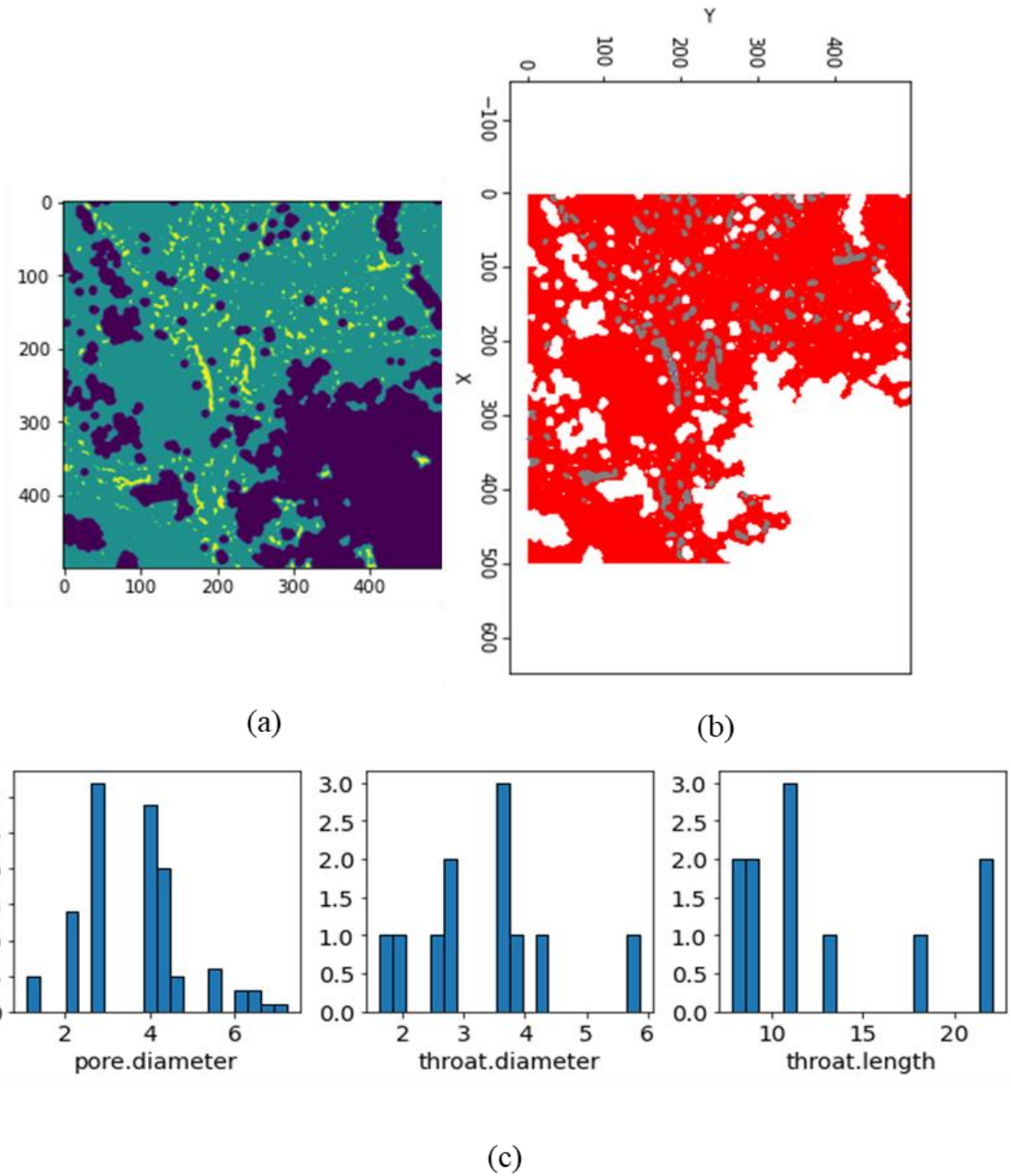


Figure 46: (a) Austin chalk three phase segmentation of a selected section, (b) network extraction and (c) histogram of network properties.

	Austin Chalk	Estailades ES32_0523	Estailades ES32_1852	Savonnieres SAVII2_m_0162
No. of macro-pores	119	39	19	71
No. of macro-throats	11	38	9	57
No. of micro-pores	150820	11933	18614	16665
No. of micro-throats	292041	20692	35376	27533
No. of Interconnects	3713	1918	1028	4385
Avg. macro- pore diameter (μm)	3.63	11.97	10.06 (max=48.38)	15.1
Avg. macro- throat dia (μm)	3.28	9.33	12.61 (max=26.4)	13.87
Absolute permeability (mD)	38.44	90.35	104	284.12
Formation Factor	109.29	134.85	77.48	61.6
Porosity % $\phi_{\text{total}} / \phi_{\text{macro}}$ $ / \phi_{\text{micro}}$	57.2 / 4.93 / 52.27	12.72 / 3.86 / 8.86	19.97 / 8.74 /11.23	31.5 / 20.4 /11.1

Table 5: Summary of network statistics for 2D carbonate samples.

Austin Chalk is a carbonate sample obtained from Austin chalk formation outcrop. The experimental values [53] and hybrid algorithm values are given below. The permeability calculated by hybrid algorithm is within a factor of 2.5 of experimental value, while experimental formation factor for this sample was not available.

Experimental

Porosity (%)	FF	LBM Permeability (mD)
25.44	--	16.4

Hybrid Algorithm

Porosity (%)	FF	Permeability (mD)
Total=57, macro=5, micro=52	109	38

Estailades Limestone A carbonate rock which exhibits a bimodal pore size distribution due to two types of pores present, well connected intergranular macro-pores and intragranular micro-pores. Figure 42 shows the SEM images of the Estailades Limestone indicating a complex pore structure and very fine feature not fully captured by the image. The pore diameters and throat diameters show a bimodal size distribution in Figure 43, and Figure 44.

The high value of permeability in Estailades sample despite of high percentage of microporosity indicates that the matrix region is well connected with macroporosity and has high internal porosity. Experimental properties are shown below [21] The permeability

calculated by hybrid algorithm is within a factor of 2.5 and formation factor calculated was within a factor of 3:

Experimental

Porosity (%)	FF	Permeability (mD)
23.7	23-25	260-280

Hybrid Algorithm

Sample	Porosity (%) ϕ_{total} , $/\phi_{macro}, /\phi_{micro}$	FF	Permeability (mD)
ES32_1852	20, 8.7, 11.3	77	104
ES32_0523	12.7, 3.8, 8.9	135	90

Savonnieres Limestone

Savonnieres is a layered oolitic limestone, having pore structure containing four different types of porosity: intergranular, intra-oolithic microporosity, and inter-granular and micro-connected microporosity [21]. The permeability ranges between 115 – 2000 mD and porosity ranges from 22% to 41%. The hybrid algorithm permeability value is within a factor of 3.5 but close to the value in DPNM [42], while the formation factor is reasonably close to value from the classical PNM model.

Experimental

	Porosity (%)	<i>FF</i>	Permeability (mD)
Experimental	21 – 41%	NA	903
Classical PNM	--	85.7	244
DPNM	--	13.5	268

Hybrid Network

Sample	Porosity (%)	<i>FF</i>	Permeability (mD)
SAVII2_m_0162	31.5	61.6	284.12

Appendix D

Filtering of Noisy Tomograms

The network extraction method works on either generated artificial images or 3-phase images obtained by segmenting real SEM images into three phases i.e., having fully resolved macropores and vugs taken as voids, while unresolved micropores are represented by a single grey-scale value and grains are identified as a solid phase. This is illustrated in Figure 47 below. The image contains a reasonably large field of view such that transport properties can be representative of the real material, the micropores here are not resolved. The real sandstone SEM has been segmented into 3 phases i.e., void, solid and region with unresolved microporosity.

Three phase segmentation method developed in-house at our research group [55] is used in this work. The details of the method are explained in the following steps:

1. Adjust histogram of each slice to match the histogram of the entire stack.
2. Apply non-local means filter for removing the speckle-type noise from the image. This requires determining by trial and error the ideal parameters for applying non-local means filter, such as estimating the noise standard deviation from the noisy image. This function assumes the noise follows a Gaussian distribution. (Non-local filters use a large region of the image to transform the value of one pixel).
3. Apply thresholds (we use two thresholds, between macro and micropore and between micro- and solids) obtained from grey level histograms on the image to get the 3-phase composite image. Apply 1st threshold for separating macropores from micropores.
4. Apply second threshold for separating micropores from solids by applying a spatially constrained iterative threshold filter.

5. Apply local-thickness filter to the grains to remove small asperities and dendrites.
6. Keep only the grains obtained from step (v) which are greater than a certain selected diameter.

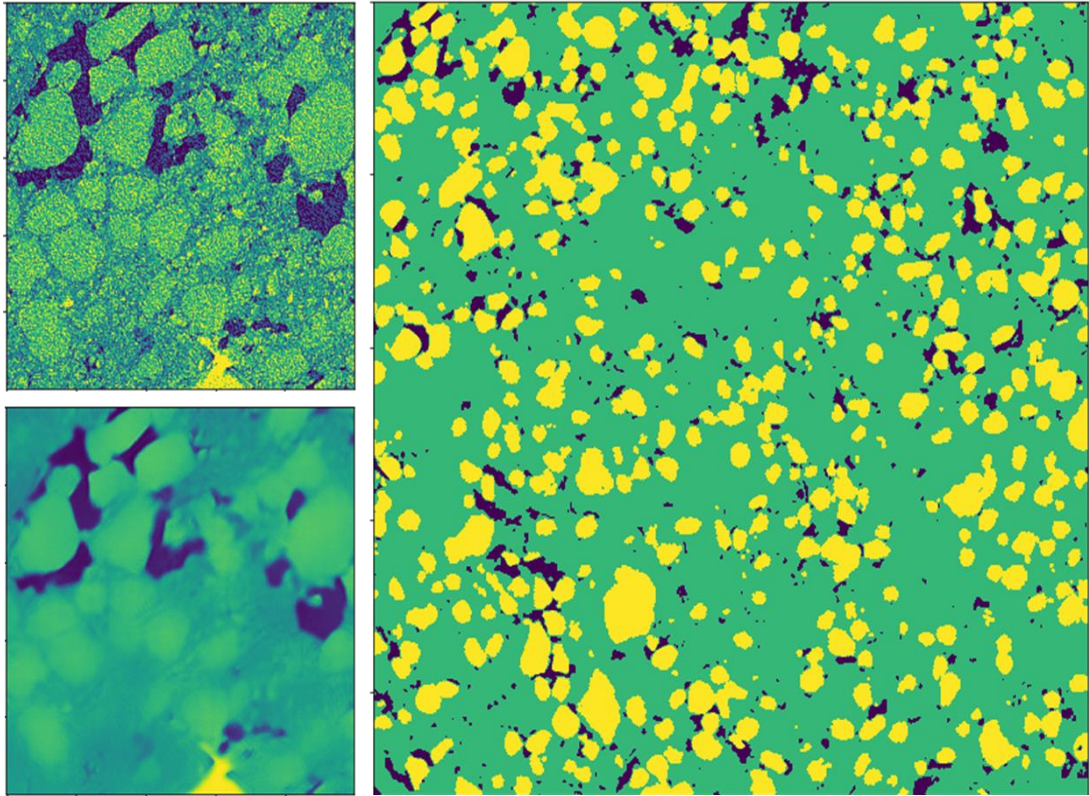


Figure 47: Example of a Tomography image of a sandstone material with microporosity. Top left shows a greyscale image where the microporosity is visible between the voids (dark) and grains (light). Bottom left shows the result after applying a non-local means filter.